

Proceedings of the 72nd
European Study Group
Mathematics with Industry

Preface

The 72nd “Studiegroep Wiskunde met de Industrie” (SWI) took place at Centrum Wiskunde & Informatica (CWI) at the Science Park in Amsterdam from 25 till 29 January, 2010. The concept of SWI is simple. During one week, around sixty mathematicians from all over Europe come together to tackle challenging industrial problems. Several companies present their problems on Monday, the mathematicians are divided in groups and devote the entire week aiming at solving the problems, and on Friday the results are presented.

The main purpose of SWI is to demonstrate that mathematical modeling and mathematical techniques are powerful tools to solve real-life problems. The motivation for most participants is also driven by the pleasure to apply mathematics to open problems, which requires team work and intensive collaboration.

We have selected companies to cover a wide range of application areas, as well as a broad spectrum of mathematical techniques. This year’s problems were provided by: the European Space Agency (ESA) on satellite communications; KEMA on energy networks; Phytocare on algae growth; the Maritime Research Institute Netherlands (MARIN) on thruster allocation; and Stork on food processing.

The enthusiasm and commitment to get optimal results given the time limitations were overwhelming and often the industrial partners were amazed by the results obtained from a short period of intense and cooperative research. In these proceedings, the scientific reports of the five groups of SWI 2010 are presented.

It is a great pleasure to thank the sponsors of SWI 2010 for their donations. STW, NWO, CWI and the five industrial partners have been very generous sponsors, and their financial contributions are strongly appreciated.

The organizing team of SWI 2010,

Arnoud den Boer, Joost Bosman, Niek Bouman, Susanne van Dam, Jason Frank,
Rob van der Mei, Chrétien Verhoef

Table of Contents

I Five Industrial Problems

1	ESA: Smart Positioning Algorithms for Indoor Navigation	2
2	KEMA: Scalability of Electricity Grids	3
3	MARIN: Thruster Allocation	5
4	Phytocare: Optimizing Algae Growth	6
5	Stork: Modeling the Production Process of Nuggets	7

II Reports by the Participating Mathematicians

1	Position Estimating in Peer-to-Peer Networks	10
1.1	Introduction	10
1.2	Problem description	11
1.3	Least squares algorithm	12
1.4	Probability density functions algorithm	15
1.5	Conclusion and discussion	24
1.6	References	24
2	Optimal Distributed Power Generation Under Network-Load Constraints	25
2.1	Introduction	25
2.2	Network model and load flow	27
2.3	Local power production and consumption	31
2.4	Objective: maximal local energy production under load constraints . .	32
2.5	Computational experiments	35
2.6	Conclusion	37
2.7	References	38
3	Thruster Allocation for Dynamical Positioning	39
3.1	Introduction	39
3.2	General problem statement	40
3.3	Approaches	43
3.4	Results	49
3.5	Recommendations	49
3.6	References	53
4	Modeling and Optimization of Algae Growth	54
4.1	Introduction	54

4.2	A hierarchy of models and some qualitative analysis	57
4.3	An ODE model for algae growth	65
4.4	An alternative PDE Model	74
4.5	Recommendations	82
4.6	References	83
5	Modeling Compressible Non-Newtonian Chicken Flow	86
5.1	Introduction	86
5.2	Modeling chicken flow	87
5.3	Construction of approximate velocity profiles	89
5.4	References	96

Part One

Five Industrial Problems

Problem 1

ESA: Smart Positioning Algorithms for Indoor Navigation

The European Space Agency (ESA) is an agency for the cooperation among European States in space research, technology and space applications. One of the topics of ESA is Satellite Navigation, being responsible for the construction of the Galileo system and an augmentation-system for GPS. Satellite Navigation has many applications, including route guidance for cars, the navigation of boats and airplanes, and the synchronization of telecom networks.

Problem Description

Today's positioning algorithms for users applying Satellite Navigation are well known and relatively simple. However, in spite of this large number of applications, Satellite Navigation has a major weakness: the availability inside buildings is rather poor (due to the attenuation of the signal by walls). As a result, alternatives for indoor navigation are a topic of research. One potential solution is to use wireless signals to determine the distance between users. In the future we could have the following scenario: inside a shopping mall, a large number of users are able to determine the distance to nearby users, whereas a minority of these users is also able to use Satellite Navigation. In addition, all users are able to exchange data, but they would like to compute their position themselves. This leads to the following question: What are the optimal positioning algorithms in this scenario?



Problem 2

KEMA: Scalability of Electricity Grids

KEMA is a global, leading authority in energy consulting and testing & certification, and is active throughout the entire energy value-chain. In a world of increasing demand for energy, KEMA has a major role to play in ensuring the availability, reliability, sustainability and profitability of energy and related products and processes. KEMA combines unique expertise and facilities, in order to add value to our customers in the field of risk, performance and quality management. With more than 2,000 people, operating from 20 countries around the globe, we are committed to offering reliable, sustainable and practical solutions. We understand and recognize the technical consequences of a business decision, as well as the business consequences of a technical decision. Innovative technology has been our starting point for more than 80 years. That is our experience you can trust.

Problem Description

Electrical power grids are becoming increasingly complex. The customer used to be solely a power-consumer, whereas nowadays more and more customers are becoming power-producers, mainly because of the development of novel components for decentralized power generation (solar panels, small wind turbines and heat pumps). And in the near future, decentralized energy buffering is expected to become important due to the growth of the electric car market.

These developments pose many interesting questions to grid operators and electricity producers. To what extent is the current power infrastructure suited for the addition of this kind of energy-producing components? Or, at which locations should the infrastructure be reinforced to handle placements of additional components? What is the peak power that is produced by these components, as a function of time, day of the week, season, etc.? What kinds of correlations exist between the yields of multiple components of the same type, which are, for instance, installed at different geographical locations? For example, if the sun is shining in a particular street, then it is likely that the sun shines in all streets in the vicinity. And what about correlations in power production between different types of components, e.g. between solar panels and wind turbines, day versus night, seasonally?

KEMA addresses these types of questions, and advises grid operators and energy producers. Although the problem is clearly complex, for the SWI we will focus on the following question.

The transmission of power in each segment of an electrical power network can be determined through a load flow analysis according to Ohm's and Kirchhoff's laws. Solving these algebraic equations can be computationally involved. In particular, simulating many alternative configurations (due to proposed placements of additional decentralized power-generating components in various locations of an existing power network, in order to assess the impact of such placements) is prohibitively complex.

Given an existing power grid, we would like to have a method that can quickly determine how many units of each type (solar panel, small wind turbine or heat pump) can be inserted into any transmission line in the network, such that under given distributions on the typical production and consumption, the maximum loads on the lines and components will not be exceeded, or if exceeded, to what degree and for what length of time this is likely to happen.

As input, we will provide the operating characteristics and statistics of the three types of components, the load-flow parameters of a model power grid of a neighborhood of a fictitious town, and typical usage data.

Depending on the progress during the week, the problem can be extended by incorporating more parameters into the analysis, adding optimization criteria, or determining necessary network reinforcement.

Problem 3

MARIN: Thruster Allocation

MARIN, the Maritime Research Institute Netherlands, has become a reliable, independent and innovative service provider for the maritime sector and a contributor to the well being of society.

MARIN has been expanding the boundaries of maritime understanding with hydrodynamic research for over 70 years. Today, this research is applied for the benefit of Concept Development, Design Support, Operations Support and Tool Development. The services incorporate a unique combination of simulation, model testing, full-scale measurements and training programmes.

Problem Description

Many ships working in the offshore industry are equipped with a dynamic positioning (DP) system. The position of the vessel is measured and actively controlled thrusters (main propellers, rudders, azimuth thrusters, bow tunnel thrusters, ...) are used to keep the vessel at the desired location. The main advantage for DP vessels working in deep water is that no mooring system is required. DP systems consist of the following components; a position reference system (to determine the position error), a Kalman filter (to separate the low frequency and wave frequency motions, in real time, without phase delay), a controller (to determine the required forces F_X , F_Y and M_Z , based on the low frequency position error) and a thrust allocation algorithm (to distribute the required total forces over the available thrusters). Typically, the vessel will have more thrusters than strictly necessary, resulting in an overdetermined allocation problem. The aim of the allocation algorithm is to generate the total thrust force, while minimizing fuel consumption (power). The output of the thruster allocation algorithm are the RPM and azimuth angle settings for each of the individual thrusters. The resulting optimization problem has the multiple challenges.



Problem 4

Phytocare: Optimizing Algae Growth

Problem Description

The runoff water from greenhouses contains fertilizers and must be cleaned before it can be returned to the groundwater system. A means of doing this is to introduce algae into the water. The algae eat up the fertilizer and clean the water. Subsequently, the algae may be removed and sold as feed, for example, to oyster farms.

Phytocare plans to grow algae in greenhouse runoff water, both for sale as feed and to clean the water. These are two different optimization criteria: (1) maximum production of algae in a production pond, and (2) maximum depletion of contaminants in an exhaustion pond. We would like to determine the best conditions for each case.

A runoff water treatment pond is a racetrack-shaped tank, 30cm deep, with a paddle wheel at one point to keep the water flowing and mixing (see Figure). Tests confirm that the mixture is homogeneous and the algae density is independent of depth. Photosynthesis depends on the amount of light present, which is a function of the time of day, the season, the weather, and the penetration into the pond (a function of the algae density and the depth). Algae growth can be influenced by varying the supply of nutrients and by controlled harvesting. Algae density is measured 3 times per day and the pond composition is regularly analyzed in a laboratory (analysis takes 1 day).

Phytocare seeks mathematical answers to the following questions. How does the photosynthesis model depend on pond composition in terms of pH, fertilizer content, temperature, CO₂ level, and sunshine? How can this dependence most efficiently be determined by means of experiments? Given a photosynthesis model, what is the dynamics of phytoplankton production? How is it influenced by weather, by nutrient supply, by harvesting? How can we optimally control the production as a function of the weather conditions (e.g. the amount of sunlight) by adjusting the nutrient supply? What is the optimal harvesting strategy? And how do the optimization strategies change, depending on whether algae production or water cleaning is the goal?



PHYTOCARE

Problem 5

Stork: Modeling the Production Process of Nuggets

Stork Food Systems is the supplier of processing systems for poultry and fresh meat. As a technology market leader, with more than 45 years of experience, process knowledge and proven track record worldwide, we support and equip food processors to create maximum process value now and in the future.

Problem Description

In meat processing equipment flow of meat mass is an important aspect. Meat mass will flow through tubes, pass bends and orifices, diverge or converge in manifolds, enter moulds, etc. Optimization of equipment to attain stable, high-end product quality requires control of this meat mass flow. We would like to be able to better predict how meat properties affect flow in our forming (moulding) machines, where meat mass is pressed in moulds during mould opening and flow is a start-stop phenomena. Meat masses have the following physical properties:

1. Viscoelastic
2. Compressible
3. Strongly inhomogeneous
4. Strongly temperature dependent

These properties together cause a very complex reaction to deformations (flow). Especially in non-continuous flow, where the value of different parameters and even the equipment itself never stabilizes, this leads to high complexity. Complexity hampers prediction of flow and final product quality and, as a result, optimization of equipment.

Nowadays, many flow problems are solved by Computational Fluid Dynamics (CFD). However, meat mass properties are very complex and CFD as a modeling tool is too complex and time consuming for such a purpose. It would not be unthinkable that there are other ways to come to a model that sufficiently predicts flow. There might be analogies with other fields of expertise that indicate possible solutions that we are not aware of this moment.

The goal of this assignment is to develop a mathematical model that predicts non-continuous flow of viscoelastic, compressible meat mass in simple geometries. Pressure fluctuation, deformation rates, mould filling rates and final product weight should be important parameters in a model.

Part Two

Reports by the Participating Mathematicians

Report 1

Position Estimating in Peer-to-Peer Networks

Authors:¹ Rogier Brussee², Mirela Dărau³, Marta Dworczynska⁴, Yabin Fan³, Paulien Koeleman⁵, Piotr Kowalczyk⁶, Nico Schlömer⁷, Tomasz Swist⁸, Sandra van Wijk³

Abstract

We present two algorithms for indoor positioning estimation in peer-to-peer networks. The setup is a network of two types of devices: reference devices with a known location and blindfolded devices that can determine distances to reference devices and each other. From this information the blindfolded devices try to estimate their positions. A typical scenario is navigation inside a shopping mall where devices in the parking lot can make contact with GPS satellites, whereas devices inside the building make contact with each other, devices on the parking lot, and devices fixed to the building. The devices can measure their in-between distances, with some measurement error, and exchange positioning information. However, other devices might only know their position with some error.

We present two algorithms for positioning estimation in such a peer-to-peer network. The first one is purely geometric and is based on Euclidean geometry and intersecting spheres. We rewrite the information to a linear system, which is typically overdetermined. We use least squares to find the best estimate for a device its position. The second approach can be considered as a probabilistic version of the geometric approach. We estimate the probability density function that a device is located at a position given a probability density function for the positions of the other devices in the network, and a probability density function of the measured distances. First we study the case with a distance measurement to a single other user, then we focus on multiple other users. We give an approximation algorithm that is the probabilistic analogue of the intersecting spheres method. We show some simulated results where ambiguous data lead to well defined probability distributions for the position of a device. We conclude with some open questions.

1.1 Introduction

There are many wireless network applications for which knowing the location of the devices within the network is necessary. Think, for example, of a military or police operation using a radio network. Other examples are locating a specific car in a parking garage, or finding your seat in a large stadium.

¹We would like to thank Jaron Samson from European Space Agency, The Netherlands, for useful discussions during the week. Thanks furthermore to the other participants who helped during the week: Rob De Staelen (University of Gent, Belgium), Rashid Mirzavand Boroujeni (TU Eindhoven, The Netherlands), and Valentina Masarotto (TU Delft, The Netherlands).

²Novay Institute, The Netherlands

³Technische Universiteit Eindhoven, The Netherlands

⁴Wroclaw University of Technology, Poland

⁵Vrije Universiteit Amsterdam, The Netherlands

⁶University of the West of Scotland, United Kingdom

⁷Univeristy of Antwerpen, Belgium

⁸National Bank of Poland, Poland

For outdoor situations GPS is widely used, and location estimates using GPS are in general very accurate [1]. However, for indoor use it is not possible to use GPS as the signal is quickly absorbed or blocked by walls. A number of indoor positioning technologies exist, see Zeimpekis et al. [2] for an overview.

In this paper we consider a network situation in which a small number of devices have knowledge of their locations, for example from using GPS or because their location is fixed. We call these devices *reference devices*. Most of the devices however, the so-called *blindfolded devices*, do not have this knowledge, but they wish to estimate their own location on the basis of location and distance information they exchange with other uses in the network. Such a network is known as a *peer-to-peer network*. We develop two algorithms for position estimation in these kind of networks. One is based on least squares methods and triangulation, and the other involves convolutions of probability density functions of the device locations.

The rest of the paper focuses on the two algorithms. Firstly, we explain the problem setting in more detail, and discuss the assumptions made in Section 2. In Section 1.3 we present the algorithm using the least squares methods. In Section 1.4 we give the algorithm based on probability density functions. Finally, in Section 1.5 we give our conclusions and suggestions for future research.

1.2 Problem description

We consider the following indoor peer-to-peer positioning problem. A number of customers inside a shopping mall want to know their positions inside the building. In order to estimate its position, each customer has a GPS device which measures the distances to and can exchange positioning information with other customers' devices. These customers can either be inside the building as well, or outside, e.g. on the parking lot. Customers inside the building might have connection to one or a few satellites, and hence might have some partial information about their exact positions. The customers outside have full satellite connection, and hence know their positions. We refer to these devices with known position as reference devices. This also includes fixed devices, such as routers, of which the position is known. The so-called blindfolded devices do not have exact position knowledge. They can try to estimate their own location based on location and distance information they exchange with other devices in the network. However, the distance measurements contain some error, and other (blindfolded) devices might be insecure about their positions as well.

We assume that the reference devices have exact or close to exact position estimates. This is because satellite connections give a location estimate with an error that is negligible compared to the error in location estimates made by blindfolded devices. The customers inside the mall are blindfolded devices, and we study the problem of how they can compute their locations, given that some of them have a connection with reference devices. We want to find an estimate for the location of each customer inside the mall.

We make the following simplifying assumptions. Firstly, we assume that there is no reflection of signal from the walls, or obstruction of the distance measurement is some way. Also, we assume the errors in the distance measurements between two

devices, to be Gaussian distributed with zero mean. The variance in the error is the same for all devices. However, we do include the fact that signals die out over a distance. For this, we assume that two devices can exchange information only if they are closer to each other than some maximum distance, which is assumed equal for all device pairs. All devices within reach are referred to as the neighbours of a given device.

We focus on a two dimensional, static problem. So, we do not allow devices to change position. In consecutive time steps, each of the devices performs distance measurements to other devices within its range, and exchanges position information. From this information, the devices estimate their positions. The question is, how a device should best process the information. We want to find an estimate for the position, as well as the accuracy (error) of this estimate. For this, two algorithms are given in the next two sections. Firstly, we consider the problem after a single time step and give an algorithm using least squares estimates. Secondly, we give an algorithm based on probability density functions, focusing also on multiple time steps.

1.3 Least squares algorithm

In this section, we give a method for estimating a given device its position after a single time step. Let X , with coordinates (x, y) , be the unknown position of the blindfolded device under consideration. Suppose it is within range of n neighbours, say A_i for $i = 1, \dots, n$, with (estimated) coordinates (x_i, y_i) . This estimate is the actual location plus some error δ_i . Also, the outcome of a single distance measurement between X and A_i is known, for all i . These measurements consists of the actual distance plus some error ε_i , which we assume to have a Gaussian distribution with zero mean and standard deviation σ . From this information, we want to estimate the position X of the device.

We start by abstracting the problem in geometrical terms in the following way. From the coordinates (x_i, y_i) and the error δ_i , it follows that the exact position of A_i should be contained in a disc with radius δ_i around (x_i, y_i) . That is, the exact position of A_i is contained in the following domain:

$$\{(a_{ix}, a_{iy}) | (a_{ix} - x_i)^2 + (a_{iy} - y_i)^2 \leq \delta_i^2\}, \quad \forall i = 1, \dots, n. \quad (1.1)$$

The exact position of X is contained in the domain:

$$\{(x, y) | (d_i - |\varepsilon_i|)^2 \leq (x - a_{ix})^2 + (y - a_{iy})^2 \leq (d_i + |\varepsilon_i|)^2\}, \quad (1.2)$$

which is a ring centered at (a_{ix}, a_{iy}) , with inner radius $d_i - |\varepsilon_i|$ and outer radius $d_i + |\varepsilon_i|$. From (1.1) and (1.2), we have that X is in:

$$\{(x, y) | (d_i - \delta_i - |\varepsilon_i|)^2 \leq (x - x_i)^2 + (y - y_i)^2 \leq (d_i + \delta_i + |\varepsilon_i|)^2\}, \quad \forall i = 1, \dots, n. \quad (1.3)$$

This is again a ring, now centered at (x_i, y_i) with radii $d_i \pm (\delta_i + |\varepsilon_i|)$. The probabilities of $\varepsilon_i \in (-\sigma, \sigma)$, $(-2\sigma, 2\sigma)$, respectively $(-3\sigma, 3\sigma)$ are about 68.2%, 95.4%, respectively

99.6%. Now based on geometrical considerations, X should be inside the intersection of the n domains given by (1.3):

$$\bigcap_{i=1}^n \{(x, y) | (d_i - \delta_i - |\varepsilon_i|)^2 \leq (x - x_i)^2 + (y - y_i)^2 \leq (d_i + \delta_i + |\varepsilon_i|)^2\}. \quad (1.4)$$

Example 1.3.1. Consider the following example for $n = 4$, where

$$\{(x_i, y_i, \delta_i, d_i) \mid i = 1, \dots, 4\} = \{(1, 1, 0.2, \sqrt{2}), (3, 1, 0.01, \sqrt{10}), \\ (-2, 0, 0.08, 2), (3, -3, 0.1, 3\sqrt{2})\},$$

$\sigma = 10^{-2}$ and $\varepsilon_i \in (-3\sigma, 3\sigma)$ randomly chosen. Figure 1.1 shows the four rings specified by (1.3). The position of X should be inside the intersection of these four rings. When zooming in, Figure 1.2 gives a closer look of the intersection (the shadowed part), i.e. the domain that X belongs to, which is (1.4).

Remark 1.3.2. When there are no errors in the distance measurements and the positions (x_i, y_i) , i.e. when all $\delta_i, \varepsilon_i = 0$, then domain (1.4) reduces to a single point.

Remark 1.3.3. The more information available (i.e. the larger n), the smaller the domain (1.4) is, i.e. the more accurately X 's position is estimated.

Now we know that X should be inside a given domain, the question is which point inside this domain should be chosen as a best estimate for X . In the following, let us consider the problem in a different way. Knowing the outcomes of the n distance measurements to its neighbours, we have the following system of equations for (x, y) :

$$\begin{aligned} (x - x_1)^2 + (y - y_1)^2 &= d_1^2 \\ (x - x_2)^2 + (y - y_2)^2 &= d_2^2 \\ &\vdots \\ (x - x_n)^2 + (y - y_n)^2 &= d_n^2 \end{aligned} \quad (1.5)$$

Since the system is quadratic, and therefore hard to solve, we use the following procedure to reduce it to a linear system. Let

$$\bar{x} = \frac{1}{n} \sum_{k=1}^n x_k, \quad \bar{y} = \frac{1}{n} \sum_{k=1}^n y_k, \quad \bar{d}^2 = \frac{1}{n} \sum_{k=1}^n d_k^2. \quad (1.6)$$

Then, for $i = 1, \dots, n$:

$$(x - x_i)^2 = (x - \bar{x})^2 + (\bar{x} - x_i)^2 + 2(x - \bar{x})(x - x_i), \quad (1.7)$$

$$(y - y_i)^2 = (y - \bar{y})^2 + (\bar{y} - y_i)^2 + 2(y - \bar{y})(y - y_i). \quad (1.8)$$

Summing (1.7) and (1.8) over all $i = 1, \dots, n$, and using the notation of (1.6), we have

$$(x - \bar{x})^2 + (y - \bar{y})^2 = \frac{1}{n} \sum_{k=1}^n d_k^2 = \bar{d}^2. \quad (1.9)$$

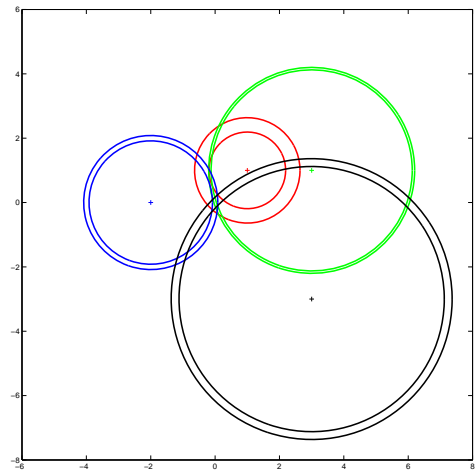


Figure 1.1: Figure of Example 1, for four neighbours.

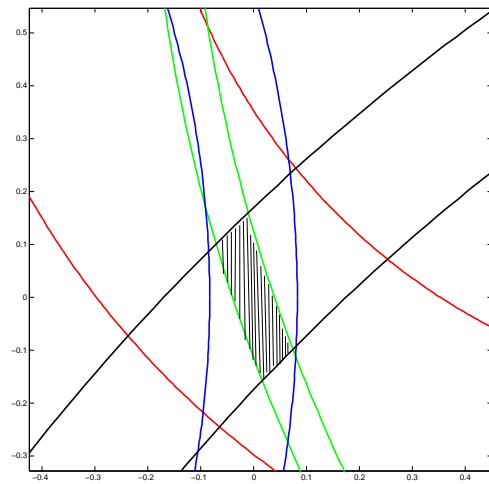


Figure 1.2: Again Figure 1.1, now zoomed in at the intersection.

Substituting (1.7) and (1.8) in (1.5), and using (1.9), we obtain the linear system

$$\begin{aligned}
 (x_1 - \bar{x})x + (y_1 - \bar{y})y &= \frac{1}{2} (d_1^2 - d^2 + (\bar{x}^2 + \bar{y}^2) - (x_1^2 + y_1^2)) \\
 (x_2 - \bar{x})x + (y_1 - \bar{y})y &= \frac{1}{2} (d_2^2 - d^2 + (\bar{x}^2 + \bar{y}^2) - (x_2^2 + y_2^2)) \\
 &\vdots \\
 (x_n - \bar{x})x + (y_1 - \bar{y})y &= \frac{1}{2} (d_n^2 - d^2 + (\bar{x}^2 + \bar{y}^2) - (x_n^2 + y_n^2))
 \end{aligned} \tag{1.10}$$

This system is generally over-determined, therefore we use the least squares method to determine the best estimate for (x, y) . That is, when writing (1.10) as $AX = b$, we find $X = (x, y)$ such that

$$\|AX - b\|_2$$

is minimized. Here $\|\cdot\|_2$ denotes the Euclidean norm, defined by $\|z\|_2 = (\sum_{i=1}^n z_i^2)^{1/2}$, for some real-valued vector $z = (z_1, \dots, z_n)$. Hence, the best position estimate for X is the least square solution of the system (1.10).

1.4 Probability density functions algorithm

In this section we present a holistic approach to the uncertainty of localization of clients. The idea is that at each moment, client k 's notion of its absolute position is described by a random variable X_k and an associated probability density function (pdf) ρ_{X_k} . This concept captures other more specific approaches, such as the one described in Section 1.3, which can be embedded into the present approach by associating each client k with pdf

$$\rho_k(\mathbf{x}) = \begin{cases} (\pi r^2)^{-1} & \text{if } \|\mathbf{x} - \mathbf{x}_k\|_2 \leq r, \\ 0 & \text{otherwise,} \end{cases}$$

where \mathbf{x}_k is the true position of client k , and r is the range of the distance measurement. In this sense, the present methodology aims to provide a general framework with the help of which it can be inferred what localization information generally can and cannot be deduced from a given client configuration. In this sense, all more simplistic approaches could use this approach as a reference framework.

The general idea is that in each (time) step, a client's pdf is updated based upon all available information, that is, measurements of its distance to neighbouring clients and their respective pdfs. In this way, within a group of clients, every individual client can alter and hopefully improve its localization pdf over time.

We try to outline in how far one can defer properties of the clients pdf by distance measurements to other clients and their pdfs. We focus on the two-dimensional case, although all presented ideas can be formulated effortlessly in any spatial dimension.

In Subsection 4.1 some required notation is introduced and the model is laid out in greater detail. Then, in Subsection 4.2, the focus is on the mathematical steps that a client has to perform to build its own pdf. This is done based upon measurements

with respect to other clients. Subsection 4.3 contains numerical experiments with simple client setups from which suggestions are derived about the characteristics of possible scenarios. Finally, the results are discussed in Subsection 4.4.

Model and notation

When a client tries to determine its position based on measurements to other clients, there are two kinds of uncertainties involved: the distance measurement itself and other clients' pdfs. We capture these uncertainties in two random variables, which are both introduced below.

Position. Let the generally unknown true position of client k be denoted by $\mathbf{x}_k \in \mathbb{R}^2$, and let the random variable X_k describe the assumed position of client k . Let ρ_k denote the corresponding probability density function. Hence, the probability that client k is located in $\Omega \subseteq \mathbb{R}^2$ is given by $P(\mathbf{x}_k \in \Omega) = \int_{\Omega} \rho_k(\mathbf{x}) d\mathbf{x}$. The random variable X_k may typically be normally distributed with mean \mathbf{x}_k , but in general, ρ_k can be every normalized integrable function.

Distance measurement. Let D_{k_0, k_1}^{1D} be the random variable giving the distance measurement of one client k_0 to another client $k_1 \neq k_0$. It is assumed that D_{k_0, k_1}^{1D} is normally (i.e. Gaussian) distributed with (unknown) mean $d_{k_0, k_1} := \|\mathbf{x}_{k_0} - \mathbf{x}_{k_1}\|_2$ and a given standard deviation $\sigma > 0$. This standard deviation could e.g. be a property of the devices in use. So,

$$D_{k_0, k_1}^{1D} \sim \mathcal{N}(d_{k_0, k_1}, \sigma^2),$$

$$\rho_{D_{k_0, k_1}^{1D}}(x) = \rho_{\mathcal{N}}(x; d_{k_0, k_1}, \sigma) := \frac{1}{\sqrt{2\pi}\sigma} \exp \left\{ -\frac{1}{2} \left(\frac{x - d_{k_0, k_1}}{\sigma} \right)^2 \right\}, \quad (1.11)$$

see Figure 1.3(a).

Based upon n statistically independent samples $\{D_i\}_{i=1}^n$ of D_{k_0, k_1}^{1D} , it is the goal to estimate (1.11), that is, to estimate d_{k_0, k_1} . The most natural approach is here to use the maximum likelihood estimator

$$\hat{D} := \frac{1}{n} \sum_{i=1}^n D_i$$

which is well known to be normally distributed as well, with standard deviation σ/\sqrt{n} :

$$\hat{D} \sim \mathcal{N}(d_{k_0, k_1}, \sigma^2/n). \quad (1.12)$$

Based upon this, it is possible to determine the probability density function of the random variable D_{k_0, k_1}^{2D} which describes the location $\mathbf{d} := \mathbf{x} - \mathbf{x}_0$ relative to a fixed spot \mathbf{x}_0 to which a distance measurement according to (1.11) was done. As there is no preference in a particular spatial direction, the pdf associated with D_{k_0, k_1}^{2D} is given by

$$\rho_{D_{k_0, k_1}^{2D}}(\mathbf{d}; \hat{d}, \sigma) = \frac{1}{2} \left(\frac{1}{2\pi} \rho_{D_{k_0, k_1}^{1D}}(\|\mathbf{d}\|_2; \hat{D}, \sigma) + \frac{1}{2\pi} \rho_{D_{k_0, k_1}^{1D}}(\|\mathbf{d}\|_2; -\hat{D}, \sigma) \right); \quad (1.13)$$

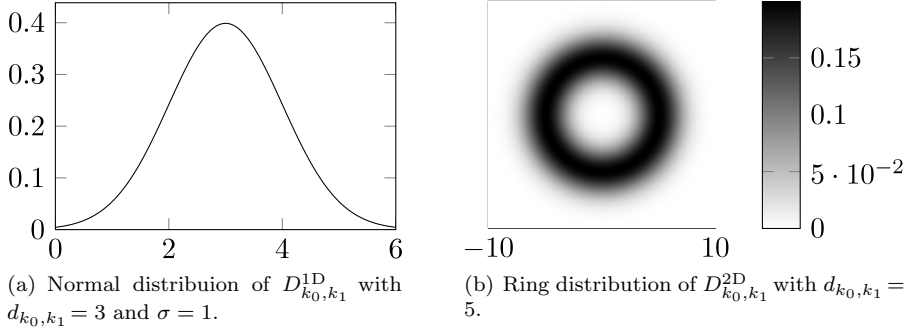


Figure 1.3: Assumed normal distribution of D_{k_0, k_1}^{1D} as defined in (1.11), along with the corresponding two-dimensional ring distribution of D_{k_0, k_1}^{2D} as defined in (1.13).

see Figure 1.3(b).

Note 1.4.1. It would also be possible to generically discard negative distance measurements, and instead of (1.11) assume a cut-off normal distribution

$$\tilde{\rho}_{D_{k_0, k_1}^{1D}}(x) = \begin{cases} I^{-1} \rho_{\mathcal{N}}(x; d_{k_0, k_1}, \sigma) & \text{for } x > 0, \\ 0 & \text{otherwise} \end{cases}$$

for D_{k_0, k_1}^{2D} . The normalization factor $I := \int_{x>0} \rho_{\mathcal{N}}(x; d_{k_0, k_1}, \sigma)$ is well-known not to have an analytic representation. However, this would lead to the simpler expression

$$\tilde{\rho}_{D_{k_0, k_1}^{2D}}(\mathbf{d}; \hat{\mathbf{d}}, \sigma) = \frac{1}{2\pi I} \rho_{D_{k_0, k_1}^{1D}}(\|\mathbf{d}\|_2; \hat{\mathbf{d}}, \sigma).$$

Note that $\tilde{\rho}$ is non-smooth at \mathbf{x}_0 , which is in the context of pdfs not a restriction.

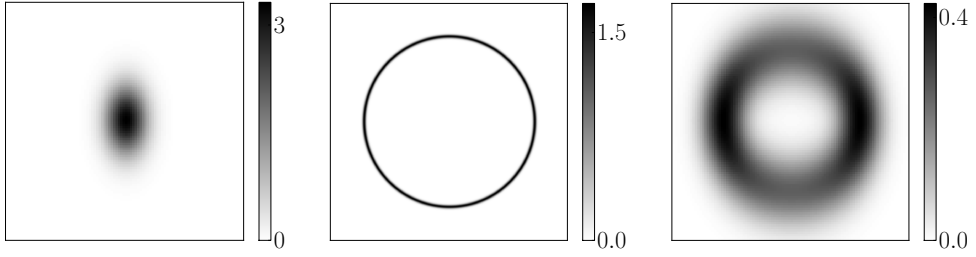
Deferring information on the location from other clients

We now make use of the knowledge gained by distance measurements to several neighbouring clients, and combine the uncertainties given by (1.13) with the pdfs of the respective neighbouring clients to get an estimate for the user's own pdf.

Distance measurements to one other client

The first question to be answered is how the estimated $\rho_{D_{k_0, k_1}^{2D}}$ of (1.13) and $\rho_{X_{k_1}}$ can be cast into an approximation for $\rho_{X_{k_0, k_1}}$. As $\mathbf{x}_{k_0} = \mathbf{x}_{k_1} + \mathbf{d}$, we set $X_{k_0, k_1} := X_{k_1} + D_{k_0, k_1}^{2D}$, where X_{k_0, k_1} describes the position of client k_0 with respect to communication with client k_1 . Furthermore, the random variables X_{k_1} and D_{k_0, k_1}^{2D} are assumed to be independent, which means that the distance measurement (error) does not depend on the actual distribution of X_{k_1} . Hence,

$$\rho_{X_{k_0, k_1}} = \rho_{X_{k_1} + D_{k_0, k_1}^{2D}} = \rho_{X_{k_1}} * \rho_{D_{k_0, k_1}^{2D}},$$



(a) Normal distribution centered at the origin, with a slightly larger deviation in the y -direction than in the x -direction.

(b) Ring distribution as defined in (1.13) with deviation significantly smaller than the deviations of the normal distribution of Figure 1.4(a).

(c) Result of the convolution of the two distributions of Figures 1.4(a) and 1.4(b).

Figure 1.4: Illustration of the convolution process of (1.14). Figure 1.4(a) shows the convolution data, Figure 1.4(b) the convolution kernel, and Figure 1.4(c) the actual convolution of the two. Note how the smaller deviation in the x -direction of the bivariate Gaussian distribution increases the values of the convolution at the x -extreme ends of the localization pdf in (c).

where the asterisk denotes convolution, i.e.,

$$\rho_{X_{k_0}, k_1}(\mathbf{x}) = \iint_{\mathbb{R}^2} \rho_{X_{k_1}}(\mathbf{y}) \rho_{D_{k_0, k_1}^{2D}}(\mathbf{x} - \mathbf{y}) d\mathbf{y}, \quad (1.14)$$

where $\rho_{X_{k_1}}$ is occasionally referred to as *convolution data* and $\rho_{D_{k_0, k_1}^{2D}}$ as *convolution kernel*. This expresses the notion that the ‘data’ distribution $\rho_{X_{k_1}}$ is acted upon and blurred by convolution with the ‘kernel’ $\rho_{D_{k_0, k_1}^{2D}}$. Note, though, that mathematically there is no distinction between data and kernel as the convolution is commutative.

The integral in (1.14) can be calculated numerically (e.g., using Fast Fourier Transformation). Figure 1.4 shows an example.

Example 1.4.2. Suppose that client k_1 knows its position exactly. So, its distribution is the Dirac-distribution centered at \mathbf{x}_{k_1} , that is $\rho_{X_{k_1}} = \delta_{\mathbf{x}_{k_1}}$. Then

$$\rho_{X_{k_0}, k_1}(\mathbf{x}) = \iint_{\mathbb{R}^2} \delta_{\mathbf{x}_{k_1}}(\mathbf{y}) \rho_{D_{k_0, k_1}^{2D}}(\mathbf{x} - \mathbf{y}) d\mathbf{y} = \rho_{D_{k_0, k_1}^{2D}}(\mathbf{x} - \mathbf{x}_{k_1}),$$

i.e., the ‘ring’ distribution centered at \mathbf{x}_{k_1} . As expected, the only contribution to the uncertainty of X_{k_0, k_1} is the uncertainty rooted in the distance measurement itself.

Distance measurements to multiple other clients

Once all $X_{k_0, k}$ for all n neighbouring clients $k \in \{k_1, \dots, k_n\}$ have been calculated, the information contained in each of them is to be combined to a common pdf X_{k_0} that indicates the localization likelihood of client k_0 based upon measurements to all

```

reset own  $P$  to uniform distribution over  $\Omega$ ;
for all clients  $k_i$  within reach do
    measure the distance to  $k_i$ ;
    create the corresponding ring distribution  $R_{k_i}$  using (1.13);
    request the pdf  $P_{k_i}$  of client  $k_i$ ;
     $P \leftarrow P \cdot (P_{k_i} * R_{k_i})$ ;
end
normalize  $P$ ;

```

Algorithm 1: One update step for the pdf of a client. In this algorithm information about previous updates is discarded. However, a client could very well store data of the previous measurements to decrease the uncertainty of its neighbours' positions. For the computations in the present paper, the mean of all previous computations is stored in each step and updated accordingly for the new measurement. This assumes that none of the clients changes its position throughout the process.

its neighbours. Quite naturally one could ask for the probability that \mathbf{x}_0 is contained in $\Omega \subset \mathbb{R}^2$ according to X_{k_0, k_1} and X_{k_0, k_2} . That is

$$P(X_{k_0, k_1} \in \Omega \wedge X_{k_0, k_2} \in \Omega) = P(X_{k_0, k_1} \in \Omega) \cdot P(X_{k_0, k_2} \in \Omega \mid X_{k_0, k_1} \in \Omega).$$

Assuming independence of X_{k_0, k_1} and X_{k_0, k_2} , this yields

$$P(X_{k_0, k_1} \in \Omega \wedge X_{k_0, k_2} \in \Omega) = P(X_{k_0, k_1} \in \Omega) \cdot P(X_{k_0, k_2} \in \Omega),$$

and subsequently for all $k \in \{k_1, \dots, k_n\}$:

$$P\left(\bigwedge_{i=1}^n X_{k_0, k_i} \in \Omega\right) = \prod_{i=1}^n P(X_{k_0, k_i} \in \Omega).$$

This results in the pdf

$$\rho_{X_{k_0}}(\mathbf{x}) = I^{-1} \prod_{i=1}^n \rho_{X_{k_0, k_i}}(\mathbf{x}),$$

with the normalization constant $I \in \mathbb{R}$.

Simulation

In this section, a few example constellations are set up and iterated over a number of time steps, to see how the pdfs of the individual users evolve when more and more accurate data of the other users becomes available. It is assumed that none of the clients moves during the process.

Each of the following example setups consists of a number of free clients (\otimes), having blindfolded devices. These are located in a square-shaped domain Ω with edge

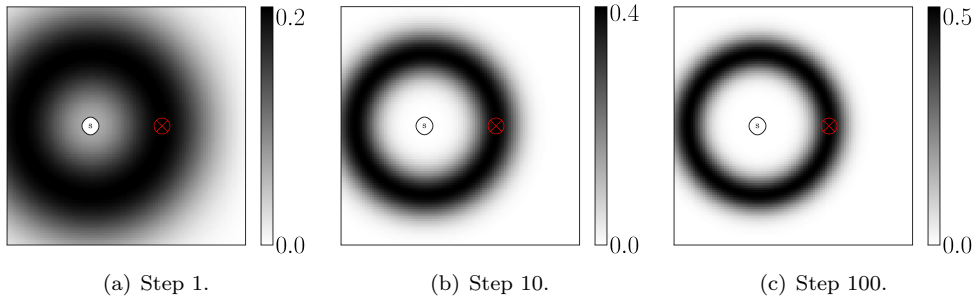


Figure 1.5: Experiment with one free client (\otimes) and one satellite client ($\textcircled{\text{S}}$) after multiple executions of Algorithm 1. The exact positions of the clients are depicted, as well as the pdf of the free client. After the first measurement, the free client can only determine its position up to rotation around the satellite client. Over time, the width of the rings becomes smaller as the deviation of the distance estimation diminished (see (1.12)), but with only one reference client the position cannot be further localized. The fuzziness of the ring distribution after 100 steps mainly depends on σ_{sat} rather than the uncertainty about the distance measurements.

length normalized to 1.0. All values indicating lengths, including standard deviations of distance measurements, hence are in units of the domain edge length.

Every client k starts off with an insignificant pdf corresponding to the random variable X_k of its spatial position, i.e. the uniform distribution over the domain Ω . Furthermore, there is at least one client who already has a significant pdf from the start, which are modeled here by clients ($\textcircled{\text{S}}$) who have a connection to a set of GPS satellites and can thus determine their positions independently from other clients. Hence, these are the reference devices. It is assumed that the pdf of client k_{sat} is the normal distribution centered at its true position $\mathbf{x}_{k_{\text{sat}}}$ with $\sigma_{\text{sat}} = 0.05$ independently for all satellite clients.

With this given setup, each of the free clients now iteratively executes Algorithm 1 to update its pdf given pdfs of its direct neighbours. The simulation is run for six settings, see Figures 1.5 to 1.10, starting from a simple case with only one satellite client and one free client, ending up with a network of multiple clients of both types. We depict the pdfs of the indicated free client after 1, 10, and 100 steps. Typically, the probability density becomes more concentrated about one location or possibly multiple locations. In this way the most likely location(s) of the clients become clearer and clearer. For each setting we discuss the setup and the results.

Discussion pdf algorithm

The presented approach gives in multiple settings reasonable outcomes, where the peak of the pdf coincides with the true position of the client. For some setups it was not possible to get any more specific information than a localization up to two significant spots (see for example Figure 1.9), although all available information was

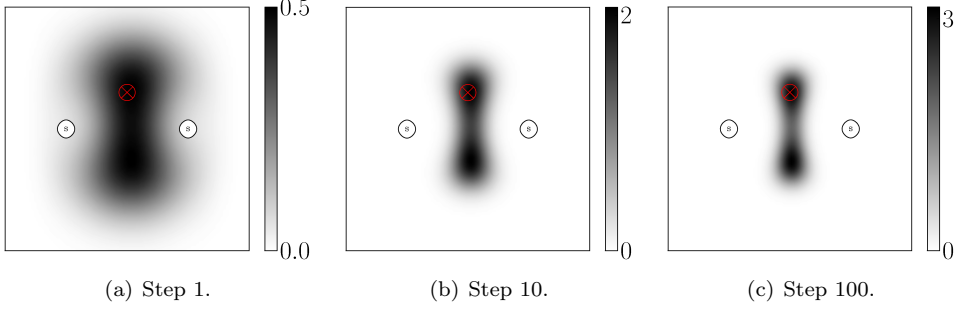


Figure 1.6: Experiment with one free client (\otimes) and *two* satellite clients (\odot) after multiple executions of Algorithm 1. After measurements to both of the satellite clients, the free client can be determined to be more likely in those regions where the two fuzzy rings overlap, i.e., where their product is locally maximal. The principal fact that two spots are preferred cannot be overcome, although again the uncertainty about the distance measurements is filtered out by sampling over 100 steps.

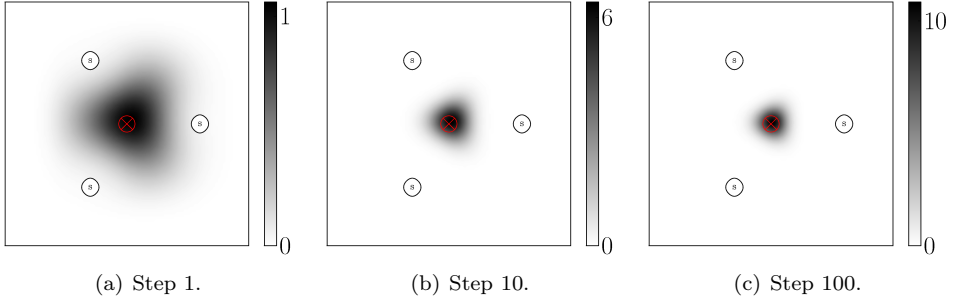


Figure 1.7: Experiment with one free client (\otimes) and *three* satellite clients (\odot) after multiple executions of Algorithm 1. As opposed to Figures 1.5 and 1.6, after one measurement already *one* fuzzy spot can be determined to likely contain the client's position. Again, certainty is increased as more samples in distance measurement are taken, such that the uncertainty σ_{sat} ultimately dominates for the free client as well.

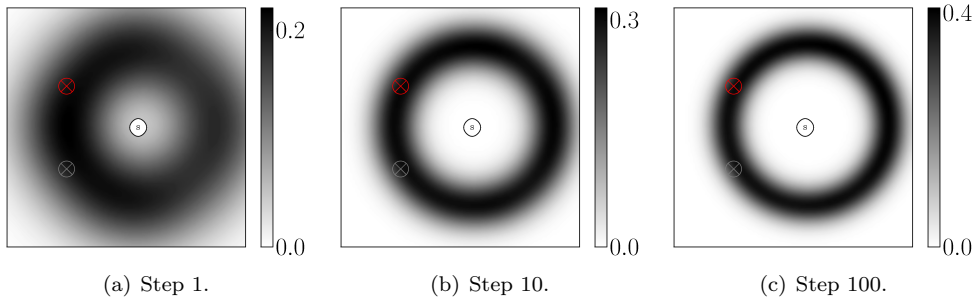


Figure 1.8: Experiment with two free clients (\otimes) and one satellite client (\textcircled{S}) after multiple executions of Algorithm 1. This situation is not much different as compared to the one in Figure 1.5, except for the fact that now two clients with (initially) rather uncertain information about their position can try to improve their localizations by exchanging information about their position relative to each other. It appears, though, that this extra information does not improve the position estimate of the individuals. The determining factor remains that there is only *one* client with absolute information about its position. This experiment suggests that adding clients without information on their absolute positions does not alter the uncertainty of localizations of present clients.

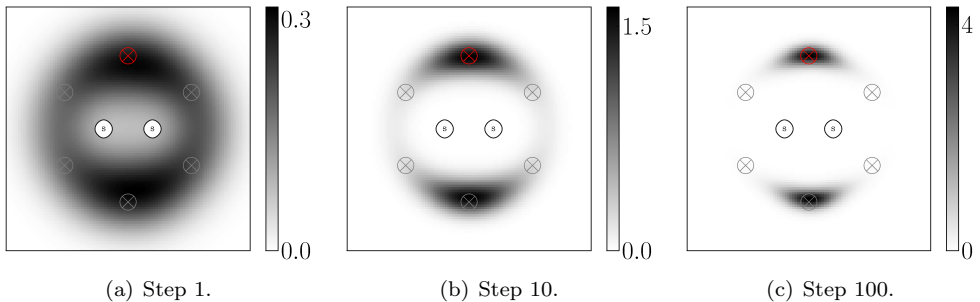


Figure 1.9: Experiment with six free clients (\otimes) and two satellite clients (\textcircled{S}) after multiple executions of Algorithm 1. No single free client has contact with both of the satellite clients, but still the localization information propagates through the network to each of the clients, such that they all have pdfs similar to the situation in Figure 1.6 rather than Figure 1.5.

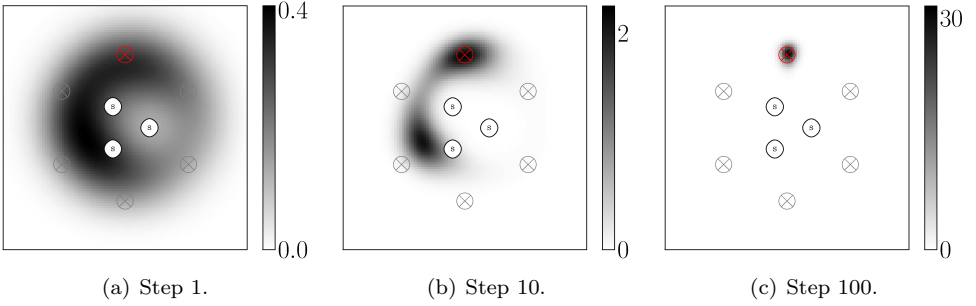


Figure 1.10: Experiment with six free clients (\otimes) and three satellite clients (\textcircled{S}) after multiple executions of Algorithm 1. Quite curiously, the pdf of \otimes has a curved shape with a preferred direction in space after one step. This is likely related to the particular (not fully rotational symmetric) arrangement of the satellite clients within the circle of the free clients. After a few steps, two spots of higher probability of localization are formed which is rather similar to the much simpler situation of Figure 1.6. One of the two preferred spots is indeed the true position of the client. After a few more steps, this location is actually preferred over the other local maximum, such that the client gets a good estimate about its position.

made use of. This means that, principally, no algorithm that uses less information can localize the client any more precisely.

An option for improvement still might be taking into account previous measurements by weighting them with the current one, and using this for the updating of the pdf. Currently, only the most recent measurement is taken into account, which can, by chance, have a large error. In an early stage of the updating process, this might cause the pdf to concentrate about an erroneous location, far off the true location, from which it needs many extra measurements to make it more accurate again. On the other hand, putting too much weights on previous measurements makes it last longer before the pdf concentrates around a location.

It must be noted that, for practical implementations, the given approach requires relatively heavy inter-client communication between the devices. Also, numerical calculation of the convolutions (1.14) is computationally expensive. This holds particularly for very fine-grained discretizations of the client's environment. An alternative for communicating an entire pdf is approximating it by, e.g., a bivariate Gaussian distribution. As only the few real-valued parameters have to be exchanged in this case, this would dramatically reduce the amount of data to be transferred. On the other hand, a bivariate Gaussian distribution might not always be suited for representing a client's position, see for example Figure 1.5. It is left for further research to investigate how much this decline in performance is, and what would be the best choice for approximation of a client's pdf.

1.5 Conclusion and discussion

In this paper we presented two promising methods for solving the problem of computing device locations from information about neighbour locations. The first method uses least square techniques, and is simple to implement and execute on a device. The second method uses complete information in the form of probability density functions and so gives more, and even more accurate, information than the first method. However, this comes at the cost of having to exchange more information between devices and using a more computation-intensive algorithm.

There are many possibilities for further research. A first important point for both methods is, if and how the algorithms converge. From our experiments we are confident that both methods converge to a location or probability distribution of a location for every device in the network, but that does not necessarily mean that they converge to the correct position. The conditions under which they actually do so, would be interesting, as would be the rate of convergence.

For the method using least squares, the question also remains how accurate the proposed method is, and how the error in the best estimated position can be determined. For the second method, an important issue still open, is the question if the amount of information transmitted and the computation to be done, can be reduced to make it more suitable for practical use. This reduction should be done with minimal loss in performance.

Finally, another important point for consideration is how these algorithms can be extended to include moving devices, that is, customers actually walking around in a mall. This makes the questions on speed of convergence and ease of computation even more relevant.

1.6 References

- [1] M. Chivers. Differential GPS explained. *Environmental Systems Research Institute, Inc.*, 2003.
- [2] V. Zeimpekis, G.M. Giaglis, and G. Lekakos. A taxonomy of indoor and outdoor positioning techniques for mobile location services. *ACM SIGecom Exchanges*, 3(4):19–27, 2002.

Report 2

Optimal Distributed Power Generation Under Network-Load Constraints

Marjan van den Akker¹, Gabriël Bloemhof², Joost Bosman³,
Daan Crommelin³, Jason Frank³, Guangyuan Yang⁴

Abstract

In electrical power networks nowadays more and more customers are becoming power-producers, mainly because of the development of novel components for decentralized power generation (solar panels, small wind turbines and heat pumps). This gives rise to the question how many units of each type (solar panel, small wind turbine or central heating power units) can be inserted into any transmission line in the network, such that under given distributions on the typical production and consumption over time, the maximum loads on the lines and components will not be exceeded.

In this paper, we present a linear programming model for maximizing the amount of decentralized power generation while respecting the load limitations of the network. We describe a prototype showing that for an example network the maximization problem can be solved efficiently. We also modeled the case where the power consumption and decentralized power generation are considered as stochastic variables, which is inherently more complex.

2.1 Introduction

Electrical power grids are becoming increasingly complex. The customer used to be solely a power-consumer, whereas nowadays more and more customers are becoming power-producers. Decentralized Power Generation (DPG) refers to an electric power source such as solar, wind or combined heat power (CHP) connected directly to the distribution network or on the customer side of the meter (Pepermans, G. et al., [8]; Chicco and Mancarella, [2]). It has emerged as a key option for promoting energy efficiency and use of renewable sources as an alternative to the traditional generation. Moreover in the near future, decentralized energy buffering is expected to become important, e.g. due to a growth of the electric car market.

These developments pose many questions to grid operators and electricity producers. To what extent is the current power infrastructure suited for the addition of this kind of energy-producing components? Or, at which locations should the infrastructure be extended to handle placements of additional components?

This question is complicated by the fact that the power production of the components strongly varies over time. Different types of components will produce peak power at different points in time, which most likely will differ from the peaks in consumption. Moreover, there are correlations between the yields of multiple components

¹Department of Information and Computing Sciences, Utrecht University

²KEMA, Arnhem

³Centrum Wiskunde & Informatica, Amsterdam

⁴Tinbergen Institute, Erasmus University Rotterdam

of the same type, which are installed at nearby geographical locations. For example, if the sun is shining in a particular street, then it is likely that the sun shines in all streets in the neighborhood.

In many cases, distributed generators can provide lower-cost electricity and higher power reliability and security with fewer environmental consequences than traditional power generators. In contrast to the use of a few large-scale generating stations located far from load centers (the approach used in the traditional electric power paradigm), DPG systems employ numerous, but small plants and can provide power on-site.

Nevertheless, the high complexity of the issues regarding the planning and management of the electric power system and infrastructure for the decentralized power generation calls for powerful analysis tools. One of the most critical factors limiting large scale DPG in an existing network is the possible over-current on connections and over-voltage on nodes. A very large power generation at a moment of low consumption in the grid will usually violate voltage profile constraints. Transmission lines between the low voltage grids may become overloaded due to altered flow patterns resulting from the DPG current contribution. This may require a network reconfiguration or generation limitations on DPG. However, network reconfiguration requires a huge investment for which the distribution network has no incentive as a natural monopoly. Hence, it is important that regulators impose limits on DPG to allow them to participate in the electricity market. In this respect, few papers have addressed the optimal sizing and placement of DPG in an existing distribution network.

Niemi and Lund [7] develop a fast tool to assess and visualize the voltage effects of DPG in an existing distribution network. Using their method, they find that over-voltages with large amount of DPG can be avoided through a proper placement strategy; placing closer to the transformer side will reduce the voltage increase. However, there are quite a few limitations in their method such that it cannot be applied generally. Their static method assumes known load pattern and DPG production over time to predict a modified steady-state voltage profile when introducing DPG, and they believe the dynamic behavior of the electric system can be accessed through a point by point calculation over time. However, in reality, there are high uncertainties in both load and DPG production which makes the net power/consumption more volatile. They restrict their method to a loopless network, because in a loopless network, the cables between adjacent nodes have an unambiguous orientation: the upstream node looks always toward the transformer and downstream node toward the end of the line, so the loopless branched network can be approximated with a single line network by matching downstream consumption and impedance at each node. Nevertheless, it is quite usual that a power distribution network has loops. Moreover, they assume an evenly distributed load along the line and some sort of even distribution of DPG units along the line. This approximation takes into account the voltage differences occurring over transmission line, but not over the individual loads.

Other papers (Gozel and Hocaoglu [3]; Acharya, Mahat and Mithulananthan [1]) propose analytical approaches to calculate the optimal sizing and placement of DPG for minimizing the total power losses in a power distribution system. They document the exact loss formula or loss sensitivity factor for the distribution system.

They examine the effect of size and placement of DPG with respect to loss in the network. However, they only considered voltage constraints and their analyses are based on the power injection or equivalent current injection which they assume to be deterministic. Kuhn and Schultz [6] developed models and algorithms for risk neutral and risk averse power optimization under uncertainty, including a stochastic integer programming model.

KEMA BV addresses many types of questions related to energy networks, and advises grid operators and energy producers. For the SWI we have focused on the following question. Given an existing power grid, we would like to have a method that can quickly determine how many units of each type (solar panel, small wind turbine or central heating power units) can be inserted into any transmission line in the network, such that under given distributions on the typical production and consumption, the maximum loads on the lines and components will not be exceeded. As input, we have used the operating characteristics and statistics of the three types of components and typical usage data.

The transmission of power in each segment of an electrical power network can be determined through a load flow analysis according to Ohm's and Kirchhoff's laws. For this analysis there is standard software available such as Vision Network Analysis⁵ for the medium voltage network and Gaia⁶ for the low voltage network. This analysis results in a linear relation between the amount of decentralized power generation and the load in the network. We first considered the situation in which the power usage of consumers and the power generated by the decentralized units is assumed to be deterministic, although it can vary over time. We derived a linear programming model for maximizing the amount of decentralized power generation while respecting the load limitations of the network. Linear programming models can be solved quite efficiently by modern solvers, for example CPLEX⁷. We have implemented a prototype for a small example network.

We also modeled the case where the power consumption and decentralized power generation are considered as stochastic variables. This case is inherently more complex, since we have to deal with probabilities of overloads.

The remainder of this paper is organized as follows. In Section 2.2 we study the network model and the load flow analysis. In Sections 2.4, 2.4, and 2.4 we describe the models for the deterministic and stochastic case respectively. Then in Section 2.5 we present numerical experiments for our prototype. Finally, Section 2.6 concludes the paper.

2.2 Network model and load flow

We model the electrical power network as an undirected graph (N, E) , where N is the set of nodes and E is the set of edges. A node corresponds to a site of electricity consumption and/or production (e.g. a house with solar panels) or to a connection point. There is an edge between two nodes i and j if there is a cable between the

⁵www.phasetophase.nl

⁶www.phasetophase.nl

⁷<http://www-01.ibm.com/software/integration/optimization/cplex/>

nodes. We assume that the network is connected, i.e., there is a path between each pair of points in the graph. For the network we define the following entities:

- H set of electricity consumption and/or production points.
- C set of connection points.
- P_i = net power production at node $i \in H$. $P_i < 0$ implies that the power consumption is larger than the power production, $P_i > 0$ implies that production is larger than consumption.
- V_i = voltage at node i
- Q_i = current flowing into or out of the network due to production at i . $Q_i > 0$ means power generation and $Q_i < 0$ means power consumption $i \in H$. For a connection point $i \in C$ we have $Q_i = 0$
- R_{ij} = resistance of cable corresponding to the edge between i and j . If there is no edge between i and j , $R_{ij} = \infty$. Resistance is independent of the direction of current flow $R_{ij} = R_{ji}$.
- I_{ij} = current flowing from nodes i to node j ($I_{ij} > 0$: flow $i \rightarrow j$, $I_{ij} < 0$: $j \rightarrow i$). Because of this definition, $I_{ij} = -I_{ji}$.

We assume the power at node i is generated at voltage V_i , such that

$$P_i(t) = V_i Q_i(t).$$

We are interested in the behaviour of the local flow I_{ij} given the production and consumption pattern Q_i . The flow of current in the network is governed by the laws of Ohm and Kirchhoff. The voltage drop along network edge (i, j) is given by *Ohm's law*

$$V_j - V_i = R_{ij} I_{ij}. \quad (2.1)$$

Kirchhoff's current law states that the total current entering a node equals the total current leaving it. For node i with net production Q_i this becomes

$$\sum_j I_{ij} = Q_i \quad (2.2)$$

Kirchhoff's voltage law states that the total voltage drop around a closed loop in the network must be zero. Let $L = \{(k_1, k_2), (k_2, k_3), \dots, (k_n, k_1)\}$ be a closed loop of n nodes. Then we have

$$\sum_{(k_i, k_{i+1}) \in L} R_{k_i, k_{i+1}} I_{k_i, k_{i+1}} = 0, \quad (2.3)$$

where $k_{n+1} = k_1$.

In 1847 Kirchhoff [5] already showed that to determine the current I , it is not necessary to consider equation (2.3) for all cycles, but only for a set of independent

cycles. For example if the equation holds for a cycle $\{A, B, C\}$ and a cycle $\{C, B, D\}$, then it also holds for the "sum" $\{A, B, D, C\}$. A well-known method to construct this set of independent cycles is as follows (see also Harary [4]). A tree is a graph without cycles. A spanning tree of a graph is a subgraph which is a tree and contains all nodes. For a connected graph with n nodes a spanning tree has $n - 1$ edges.

We take a spanning tree T of the graph. If we extend T by one edge from outside T we obtain a cycle. From the set of edges outside T , we now obtain a set of cycles, where each cycle is obtained by extending T with a single edge. This set of cycles forms a set of independent cycles. In fact it forms a *cycle base*, i.e. a family of cycles which spans all cycles of the graph. Now it is easy to see that the size of a cycle base equals

$$|E| - (|N| - 1).$$

In general, Kirchhoff's voltage law on the elements of a cycle base, implies Kirchhoff's voltage law on all loops. Hence, Kirchhoff's voltage law can be described by $|E| - (|N| - 1)$ equations of type (2.3).

We assume that the local network is connected to an infinite power reservoir and modelled by one node, say ∞ , connected to the outside world. This reservoir can provide (or absorb) any amount of net power produced by the local network. For simplicity, we will disregard the voltages and equations (2.1), by assuming that the power at the nodes is produced approximately at a constant voltage. As a result, we can analyse the load flow entirely in terms of currents and resistances. Thus, given the resistance R and the local production Q , we can use (2.2) and (2.3) to calculate I .

For the local flow, we do have to worry about equation (2.2) for the point ∞ . We conclude that Kirchhoff's current law can be described by $|N| - 1$ equations of type (2.2). Since Kirchhoff's voltage law can be described by $|E| - (|N| - 1)$ equations of type (2.3), the local flow I on the edges can be expressed in terms of R and Q by $|E|$ equations. From this we can easily show that there is a matrix A such that

$$I = A Q. \tag{2.4}$$

We illustrate this by the following example.

Example. To work with a concrete example, we consider the simple example network of Figure 2.1. This network has five houses indexed $1, \dots, 5$ with two houses in a closed loop, and three more houses in a radial network. The points with indices a , b and c are connection nodes, that have no generation or usage.

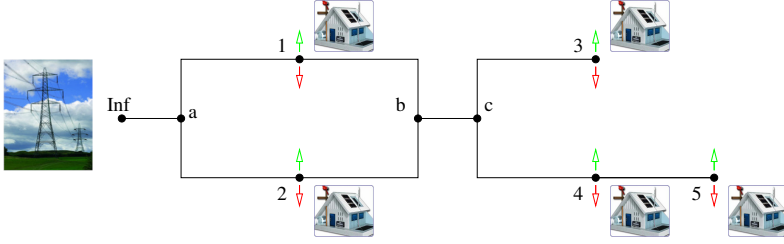


Figure 2.1: Example network

Kirchhoff's current laws for the respective nodes are:

$$I_{\infty a} - I_{a1} - I_{a2} = 0 \quad (a)$$

$$I_{a1} - I_{1b} + Q_1 = 0 \quad (1)$$

$$I_{a2} - I_{2b} + Q_2 = 0 \quad (2)$$

$$I_{1b} + I_{2b} - I_{bc} = 0 \quad (b)$$

$$I_{bc} - I_{c3} - I_{c4} = 0 \quad (c)$$

$$I_{c3} + Q_3 = 0 \quad (3)$$

$$I_{c4} - I_{45} + Q_4 = 0 \quad (4)$$

$$I_{45} + Q_5 = 0 \quad (5)$$

For the loop, Kirchhoff's voltage law gives

$$R_{a1}I_{a1} + R_{1b}I_{1b} - R_{2b}I_{2b} - R_{a2}I_{a2} = 0.$$

For ease of exposition, we assume $R_{a1} = R_{1b} = R_{2b} = R_{a2}$, so that Kirchhoff's voltage law results in $I_{a1} + I_{1b} - I_{2b} - I_{a2} = 0$.

The above equations can be written in matrix form

$$\begin{bmatrix} 1 & -1 & -1 & 0 & 0 & 0 & 0 & 0 & 0 \\ 0 & 1 & 0 & -1 & 0 & 0 & 0 & 0 & 0 \\ 0 & 0 & 1 & 0 & -1 & 0 & 0 & 0 & 0 \\ 0 & 0 & 0 & 1 & 1 & -1 & 0 & 0 & 0 \\ 0 & 0 & 0 & 0 & 0 & 1 & -1 & -1 & 0 \\ 0 & 0 & 0 & 0 & 0 & 0 & 1 & 0 & 0 \\ 0 & 0 & 0 & 0 & 0 & 0 & 0 & 1 & -1 \\ 0 & 0 & 0 & 0 & 0 & 0 & 0 & 0 & 1 \\ 0 & 1 & -1 & 1 & -1 & 0 & 0 & 0 & 0 \end{bmatrix} \begin{pmatrix} I_{\infty a} \\ I_{a1} \\ I_{a2} \\ I_{1b} \\ I_{2b} \\ I_{bc} \\ I_{c3} \\ I_{c4} \\ I_{45} \end{pmatrix} = \begin{pmatrix} 0 \\ -Q_1 \\ -Q_2 \\ 0 \\ 0 \\ -Q_3 \\ -Q_4 \\ -Q_5 \\ 0 \end{pmatrix} \quad (2.5)$$

The matrix on the left, which we denote by B is nonsingular. We also define the

injection matrix

$$J = \begin{bmatrix} 0 & 0 & 0 & 0 & 0 \\ -1 & 0 & 0 & 0 & 0 \\ 0 & -1 & 0 & 0 & 0 \\ 0 & 0 & 0 & 0 & 0 \\ 0 & 0 & 0 & 0 & 0 \\ 0 & 0 & -1 & 0 & 0 \\ 0 & 0 & 0 & -1 & 0 \\ 0 & 0 & 0 & 0 & -1 \\ 0 & 0 & 0 & 0 & 0 \end{bmatrix}$$

and the vectors $I = (I_{\infty a}, I_{a1}, I_{a2}, I_{1b}, I_{2b}, I_{bc}, I_{c3}, I_{c4}, I_{45})^T$ of loads and $Q = (Q_1, Q_2, Q_3, Q_4, Q_5)^T$ of net productions. With this notation, equation (2.5) takes the form

$$BI = JQ.$$

Recall from the above that B is a square nonsingular $|E| \times |E|$ matrix, and we can define $A = B^{-1}J$, cf. (2.4), with

$$A = \frac{1}{4} \begin{bmatrix} -4 & -4 & -4 & -4 & -4 \\ -3 & -1 & -2 & -2 & -2 \\ -1 & -3 & -2 & -2 & -2 \\ 1 & -1 & -2 & -2 & -2 \\ -1 & 1 & -2 & -2 & -2 \\ 0 & 0 & -4 & -4 & -4 \\ 0 & 0 & -4 & 0 & 0 \\ 0 & 0 & 0 & -4 & -4 \\ 0 & 0 & 0 & 0 & -4 \end{bmatrix} \quad (2.6)$$

2.3 Local power production and consumption

We write the net production of power at node i as

$$P_i(t) = -U_i(t) + \sum_k S_{ik}(t) \quad (2.7)$$

where U_i is the power consumption and S_{ik} is the generation by a device of type k (e.g. solar panel of given type, wind turbine, CHP unit, ...). Assume we can specify a distribution of local energy sources by choosing constants σ_{ik} such that

$$S_{ik}(t) = \sigma_{ik} \tilde{S}_{ik}(t) \quad (2.8)$$

where $\tilde{S}_{ik}(t)$ are unit production rates (possibly random), e.g. for solar production at a given node. \tilde{S} represents the solar insolation per m^2 , multiplied by a (possibly time-dependent) efficiency parameter that incorporates the angle of orientation of the solar panel and its efficiency factor (W/lux). Thus, σ_{ik} determines the size of the production unit (e.g. m^2 solar panels) of type k at node i .

As mentioned earlier, we assume that the power at each node in the local network is produced at a given voltage V_i . We will also assume that these voltages are all approximately equal, i.e. $V_i \approx V_j$. This implies that Q_i depends on σ_{ik} in much the same way as P_i :

$$Q_i(t) = q_{i0}(t) + \sum_k \sigma_{ik} q_{ik}(t) \quad (2.9)$$

2.4 Objective: maximal local energy production under load constraints

Deterministic case

The overall objective is to maximize the collective yearly energy production E by the local energy production units, while obeying constraints on the loads in the local network. In the deterministic setting, these are hard constraints, of the form $|I_{ij}| \leq I_{ij}^m$ with given maximal loads I_{ij}^m . For simplicity, we will not take into account constraints on the voltages (recall that we had assumed the voltages to be given).

We denote the yearly energy production of a unit size device of type k at node i as

$$\Sigma_{ik} = \int_{\text{year}} dt \tilde{S}_{ik}(t)$$

The total energy production E is determined by the σ_{ik} and Σ_{ik} . In this section, all Σ_{ik} , and thereby E , are considered to be non-random. The objective is to maximize E under variation of σ . Thus:

$$\begin{aligned} \hat{\sigma} &= \arg \max_{\sigma} E(\sigma) \\ &= \arg \max_{\sigma} \sum_i \sum_k \sigma_{ik} \Sigma_{ik} \end{aligned} \quad (2.10)$$

$$= \arg \max_{\sigma} \sigma^T \Sigma \quad (2.11)$$

under the constraints

$$\forall i, j, t: \quad |I_{ij}| \leq I_{ij}^m \quad (2.12)$$

$$\forall i, k: \quad \sigma_{ik} \geq 0 \quad (2.13)$$

Because of (2.4) we can write

$$I_{ij}(t) = \sum_{j'} A_{ijj'} Q_{j'}(t). \quad (2.14)$$

By substituting this expression in (2.9) the current constraints (2.12) can be recast as

$$\forall i, j, t: \quad -I_{ij}^m \leq A_{ij}^0(t) + \sum_{j', k} \tilde{A}_{ijj'k}(t) \sigma_{j'k} \leq I_{ij}^m \quad (2.15)$$

or

$$-I^m \leq A^0(t) + \tilde{A}(t) \sigma \leq I^m \quad (2.16)$$

with

$$A_{ij}^0(t) = \sum_{j'} A_{ijj'} q_{j'0}(t) \quad (2.17)$$

$$\tilde{A}_{ijj'k}(t) = A_{ijj'} q_{j'k}(t) \quad (2.18)$$

Although the objective function does not depend on time, the constraints do: we need $-I^m \leq A^0(t) + \tilde{A}(t)\sigma \leq I^m$ for all t . Can we find t_1, \dots, t_N such that if the constraints are satisfied at t_1, \dots, t_N then they are satisfied for all t ? If so, we extend the number of linear constraints (one set for every t_n) and solve the resulting LP.

Summarizing: if we check the constraints (2.15) only at a finite number of points in time (t_1, \dots, t_N) , we have to solve the following linear program (LP):

$$\hat{\sigma} = \underset{\sigma}{\operatorname{argmax}} E(\sigma) \quad (2.19)$$

$$E = \sigma^T \Sigma \quad (2.20)$$

$$\sigma \geq 0 \quad (2.21)$$

$$\tilde{A}(t_1)\sigma \leq I^m - A^0(t_1) \quad (2.22)$$

$$-\tilde{A}(t_1)\sigma \leq I^m + A^0(t_1) \quad (2.23)$$

$$\vdots \quad (2.24)$$

$$\tilde{A}(t_N)\sigma \leq I^m - A^0(t_N) \quad (2.25)$$

$$-\tilde{A}(t_N)\sigma \leq I^m + A^0(t_N) \quad (2.26)$$

Benefits of increasing the maximum loads

From the theory of linear programming it is known that each linear program

$$\max\{c^T x \mid Ax \leq b, x \geq 0\}$$

has a corresponding dual problem

$$\min\{b^T u \mid A^T u \geq c, u \geq 0\}.$$

The optimal values of the dual variables u are called the shadow prices of the constraints $Ax \leq b$ (i.e., the constraints (2.22) – (2.26) for the network problem considered here). These optimal values can be calculated from the solution of the original (primal) LP. Let \hat{x} and \hat{u} denote the solutions of the primal and dual LP. Assuming these solutions exist, they satisfy $c^T \hat{x} = b^T \hat{u}$. Thus, the shadow prices \hat{u} can be seen as the gradient of the maximum $c^T \hat{x}$ of the (primal) objective function with respect to the constraints b .

Let the shadow prices associated with the constraints (2.22), (2.25), etc. for edge (i, j) be denoted by $\hat{u}_{ij}(t_1)$ and $\hat{u}_{ij}(t_N)$. Similarly, $\hat{w}_{ij}(t_1)$ and $\hat{w}_{ij}(t_N)$ denote the shadow prices associated with (2.23), (2.26), etc. If the I_{ij}^m is increased by a small value ϵ , the value of the maximum yearly energy production $E(\hat{\sigma})$ will increase by

$$\Delta_{ij}(\epsilon) = \epsilon \sum_{n=1}^N (\hat{u}_{ij}(t_n) + \hat{w}_{ij}(t_n)).$$

Edges (i, j) for which this value is largest represent connections for which investment in additional load capacity is most beneficial.

Stationary stochastic case

In this section we assume that usage and generation at nodes are stationary random variables, i.e. all U_i and \tilde{S}_{ik} are characterized by probability distributions that are independent of time. For the objective function we take the expectation of the energy production (which, due to the assumption of stationarity, is proportional to the expectation of the power production). That is,

$$\mathbb{E}E(\sigma) = \mathbb{E} \sum_{i,k} \sigma_{ik} \int_{\text{year}} dt \tilde{S}_{ik} \quad (2.27)$$

$$\propto \sum_{i,k} \sigma_{ik} \mathbb{E} \tilde{S}_{ik} \quad (2.28)$$

Thus, the objective function is (again) linear in σ .

The constraints must be reformulated. Rather than imposing a hard constraint $|I_{ij}| \leq I_{ij}^m$, we want the probability that currents exceed their threshold to be below a certain level. Thus, we require

$$\text{Prob}(|I_{ij}| > I_{ij}^m) < \epsilon_{ij} \quad (2.29)$$

Alternatively, we can use a single constraint:

$$\text{Prob}(\exists(i, j) |I_{ij}| > I_{ij}^m) < \epsilon \quad (2.30)$$

An interesting, related question is: given a set of constants σ_{ik} , what is the probability distribution for any I_{ij} ? That distribution tells us e.g. what the probabilities are for small and large overloads.

Because of the linearity of the system (I depends linearly on Q , Q depends linearly on σ , U and \tilde{S}), the random variable I_{ij} is a linear combination of the random variables U_i and \tilde{S}_{ik} . We cannot assume that the U_i and \tilde{S}_{ik} are all independent. In fact, for some types of production devices (e.g. solar panels) we expect $\tilde{S}_{ik} \approx c_{ij} \tilde{S}_{jk}$ for any i, j (unless the network is well spread out geographically). In other words, two solar panels of the same size but at different (nearby) locations produce nearly the same power at equal times.

Constructing the probability distributions for the I from those for U and \tilde{S} will be difficult, partly because the dependence discussed above. Another complication stems from the type of distributions for U and \tilde{S} : it is questionable that those are close to known distributions (such as Gaussian). Monte-Carlo simulation can provide a way out (but may be time-consuming).

Time-dependent stochastic case

Clearly, it is more realistic to consider U_i and \tilde{S}_{ik} as non-stationary stochastic processes, rather than as stationary random variables. The non-stationarity stems from

the dependence of U_i and \tilde{S}_{ik} on seasonality and on the day/night cycle. The objective function, the expected yearly energy production, is still linear in σ :

$$\mathbb{E} E(\sigma) = \mathbb{E} \sum_{i,k} \sigma_{ik} \int_{\text{year}} dt \tilde{S}_{ik} \quad (2.31)$$

$$= \sum_{i,k} \sigma_{ik} \int_{\text{year}} dt \mathbb{E} \tilde{S}_{ik}, \quad (2.32)$$

where we have used $\mathbb{E} \int dt \tilde{S} = \int dt \mathbb{E} \tilde{S}$ because all \tilde{S}_{ik} are non-negative. Formulating (or estimating) suitable stochastic processes will be a major challenge. In fact, a hybrid approach (consisting of deterministic signals incorporating the daily, weekly and seasonal cycles, and supplemented by a stationary noise) may be plausible.

2.5 Computational experiments

For this paper we conducted numerical experiments for the deterministic case of Section 2.4 only. There was insufficient data for testing the stochastic model.

For the SWI, typical solar production and household usage data were provided by KEMA in the following form: 1) a database containing the instantaneous power flow in Watts for 27 households at 10 minute intervals for one week and 2) solar insolation data in lux at 10 minute intervals for one year.

Making use of the network of Figure 2.1 and corresponding matrix A (2.6) we solved the deterministic LP (2.19)–(2.26) on a one week interval with time constraint period $\Delta t = t_{n+1} - t_n = 10$ minutes. The usage data $U_i(t)$ was taken from the first 5 households of the provided data.

We took all power line maximum load constraints to be $I_{ij}^m = 70A$. We assume only a single type of decentralized generation, namely solar energy. To this end we ignore the second index k on source terms and denote them simply by $S_i(t)$, etc. We chose $S_i(t) = (100 \text{ W/m}^2) \tilde{S}_i(t) \sigma_i$, so that σ_i can be interpreted as the surface area of solar panels in m^2 at node i . Solar insolation \tilde{S}_i was taken from the first week of the given datafile, and assumed to be uniform over the model neighborhood.

The solution of the optimization problem is shown in Figure 2.2. For the optimal configuration, Figure 2.2a shows the loads in Amperes on all edges. Loads a1 and a2 are approximately equal. The critical load is reached on edges a1 and a2 after approximately 6.5 days.

The optimal configuration of solar panels is

$$\begin{aligned} \sigma_1 &= 122 \text{ m}^2 \\ \sigma_2 &= 121 \text{ m}^2 \\ \sigma_3 &= 31 \text{ m}^2 \\ \sigma_4 &= 24 \text{ m}^2 \\ \sigma_5 &= 8 \text{ m}^2 \end{aligned}$$

For this arrangement, the production in kW at each household is shown in Figure 2.2b. Productions at nodes 1 and 2 are nearly equal and significantly greater than

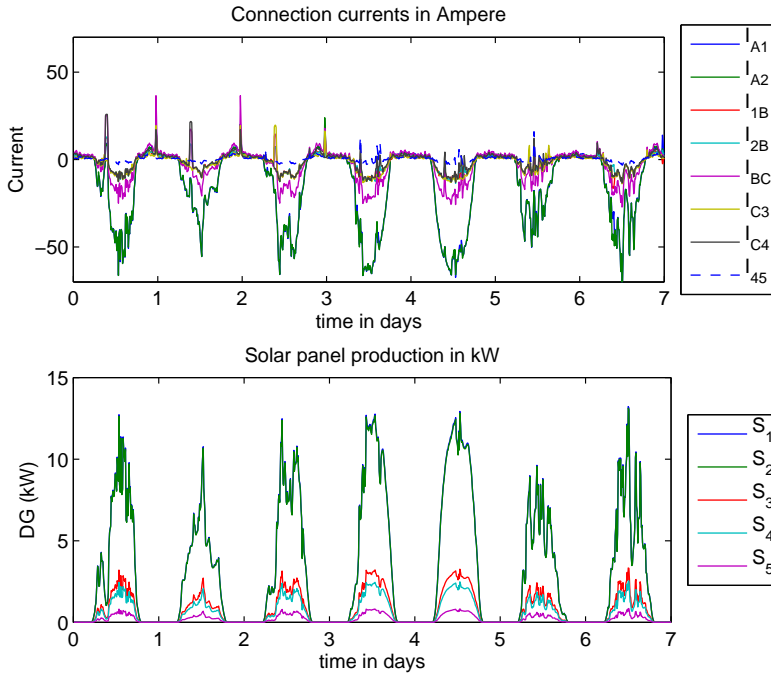


Figure 2.2: Optimal configuration of solar panels: (top) current flow through each network edge for the optimal configuration (negative flow is upstream, consistent with a net surplus in decentralized generation); (bottom) total solar generation at each household node for the optimal configuration.

nodes 3–5. The total optimal production is 1340 kWh/yr, with a net positive energy production of 1070 kWh/yr.

This fact hints at a possible problem with the simple optimization model used here. In particular, the benefit to a consumer of placing solar panels is dependent on that consumer's node in the network topology. For an optimal production, some consumers will gain a much more significant advantage than others. We also computed an alternative configuration for a strict 'fair play' scenario in which we assume all households are allowed an equal maximum solar production, enforced by taking $\sigma_i = \sigma = \text{const}$. We manually iterated to obtain an approximate best value of σ of 50 m². Figure 2.3a shows the loads on each network edge. The critical load again occurs on edges a1 and a2 after 6.5 days. In Figure 2.3b the production of all households is equal by assumption. Under the 'fair play' scenario, the total production is reduced to 1100 kWh/yr and net production to 830 kWh/yr.

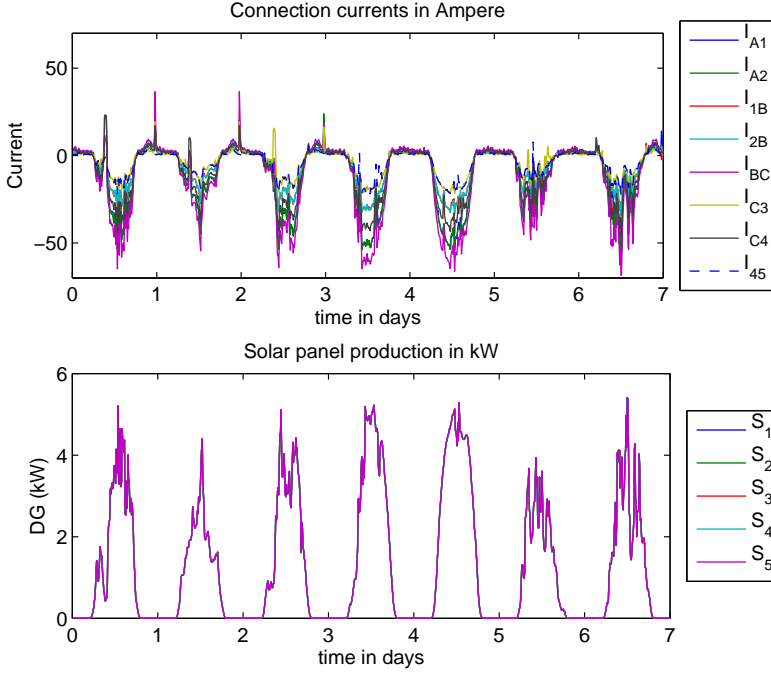


Figure 2.3: Optimal ‘fair play’ configuration of solar panels: (top) current flow through each network edge for this configuration; (bottom) total solar generation at each household node is equal.

2.6 Conclusion

In this paper, we developed a method that can quickly determine how many units of each type (solar panel, small wind turbine or central heating power units) can be inserted into any transmission line in the network, such that under given distributions on the typical production and consumption, the maximum loads on the lines and components will not be exceeded.

We first considered the situation where the power production and consumption are considered deterministic but vary over time. We derived a linear programming model for maximizing the amount of decentralized power generation while respecting the load limitations of the network. Since linear programming problems can be solved efficiently this is a promising result from the viewpoint of the application. We presented an initial model for the case where power consumption and production are considered as stochastic variables.

For the deterministic case we implemented a prototype in Matlab for a small example. The results are promising since we could quickly compute the optimal allocation of power generation units with a 10 minute time granularity. The results revealed that the optimal allocation is unbalanced in the sense that houses closer to

the connection point to the high voltage network are allowed to generate much more power than house located further from this connection, consistent with the findings of Niemi and Lund [7]. To achieve complete fairness, we tested the situation where each house generates the same amount of power. Then the financial benefits are more uniformly distributed among the consumers. However, this provides a significantly lower power production. Consequently, the development of intelligent fairness criteria, which for example can be achieved by adding additional constraints to the linear programming model, is an interesting issue for further research.

2.7 References

- [1] Acharya, N., Mahat, P. and Mithulananthan, N., 2006. An analytical approach for DG allocation in primary distribution network. *Electrical Power and Energy System*. 28, 669–678.
- [2] Chicco, G. and Mancarella, P., 2009. Distributed multi-generation: A comprehensive view. *Renewable and Sustainable Energy Reviews*. 13, 535–551.
- [3] Gozel, T. and Hocaoglu, M.H., 2009. An analytical method for the sizing and siting of distributed generators in radial systems. *Electric Power Systems Research*. 79, 912–918.
- [4] Harary F. (1972). *Graph Theory*. Addison-Wesley Series in Mathematics, Third printing
- [5] Kirchhoff G. (1847). Über die Auflösung der Gleichungen, auf welche man bei der Untersuchung der linearen Verteilung galvanischer Ströme geführt wird. *Ann. Phys. Chem*, 72, pp. 497-508.
- [6] Kuhn S. and Schultz R. (2009). Risk neutral and risk averse power optimization in electricity networks with dispersed generation. *Mathematical Methods in Operations Research*, 69: 353-367.
- [7] Niemi, R. and Lund, P.D. 2009. Decentralized electricity system sizing and placement in distribution networks. *Applied Energy*. forthcoming.
- [8] Pepermans G., Driesen J., Haeseldonckx D., Belmans R., D’Haeseleer W., 2005. Distributed generation: definition, benefits and issues. *Energy Policy*. 33(6), 787–798.

Report 3

Thruster Allocation for Dynamical Positioning

Authors:¹ Koen Poppe², Jan Bouwe van den Berg³, Elisabeth Blank⁴,
Claude Archer⁵, Magnus Redeker⁶, Michael Kutter⁶, Piet Hemker⁷

Abstract

Positioning a vessel at a fixed position in deep water is of great importance when working offshore. In recent years a Dynamical Positioning (DP) system was developed at Marin [2]. After the measurement of the current position and external forces (like waves, wind etc.), each thruster of the vessel is actively controlled to hold the desired location.

In this paper we focus on the allocation process to determine the settings for each thruster that results in the minimal total power and thus fuel consumption. The mathematical formulation of this situation leads to a nonlinear optimization problem with equality and inequality constraints, which can be solved by applying Lagrange multipliers.

We give three approaches: first of all, the full problem was solved using the MATLAB `fmincon` routine with the solution from the linearised problem as a starting point. This implementation, with robust handling of the situations where the thrusters are overloaded, lead to promising results: an average reduction in fuel consumption of approximately two percent. However, further analysis proved useful. A second approach changes the set of variables and so reduces the number of equations. The third and last approach solves the Lagrange equations with an iterative method on the linearized Lagrange problem.

3.1 Introduction

In this report, we focus on the allocation part of the full closed loop control system, depicted in Figure 3.1, which is used to keep the vessel in a stationary position. This allocation unit receives the required total force and momentum from the PID-controller and will try to generate these by sending the appropriate control signals to the available actuators of the vessel.

Note that the problem is considered to be 2-dimensional. In fact, any movement in the z -direction (up/down) is ignored due to its periodic behavior. Also, most common actuators do not have the ability to produce thrust in the z -direction. This clearly reduces the complexity of the problem.

¹Other participants: Hans Stigten and Sudhir Jain.

²Department of Computer Science, Katholieke Universiteit Leuven

³Department of Mathematics, VU University Amsterdam

⁴Department of Mathematics, University of Karlsruhe

⁵Royal Military Academy, Belgium

⁶Department of Mathematics, University Stuttgart

⁷Korteweg-de Vries Institute for Mathematics, University of Amsterdam

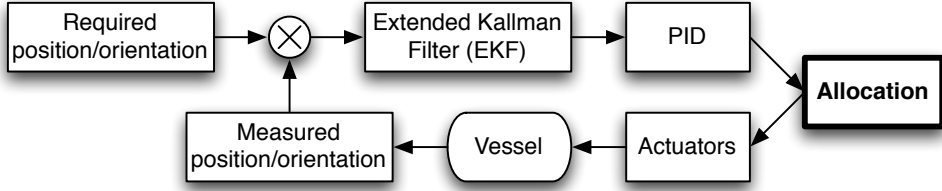


Figure 3.1: The closed loop control system. Measurements of the position of the vessel are compared with the required position. The difference is fed into a Extended Kalman Filter and PID-controller to convert this to the force and momentum required to correct the position. The allocation unit controls the thrusters, which must generate the required force and momentum.

Semi-submersible setup

Several types of actuators exist, but we limit ourselves to the azimuth thruster, shown in Figure 3.2(a). These are able to direct their thrust in 360 degrees around the z -axis. They are frequently used in the semi-submersible configuration shown in Figure 3.2(b). This kind of vessel consists of two pontoons which remain under water and eight poles that connect the pontoons with a large rectangular platform above the waters surface, a setup that is often used for offshore drilling in deep water, where anchors cannot be used.

It is necessary to introduce some notations. First of all, the coordinate system is installed in the center of gravity and the x -axis is pointing in the *forward* direction. The z -axis is the upwards direction and so the y axis points towards starboard. Let us denote the total required forces, given in x - and y -direction, by \mathbb{F}_x and \mathbb{F}_y respectively, and \mathbb{M}_z , the required momentum in z -direction. These must be generated by the N thrusters that are positioned on the bottom of the ship. We denote the force per thruster by its components $(f_{x,i}, f_{y,i}) \in \mathbb{R}^2$ for $i=1, \dots, N$. An alternative polar notation using $T_i = \sqrt{f_{x,i}^2 + f_{y,i}^2}$ for the thrust and $\alpha_i \in [-\pi, \pi)$ for the orientation relative to the x -axis, is shown in Figure 3.2(a). Furthermore, we use P for the total power used in a given time step and \bar{T}_i and \bar{P}_i respectively for the maximal thrust and maximal power for thruster i .

Some dimensions and the coordinates (x_i, y_i) , indicating the positions of the thrusters on the semi-submersible, are summarized in Figure 3.2(b).

3.2 General problem statement

The allocation problem can be translated to a constrained optimization problem. We introduce the objective function and the constraints of this minimization problem in the following paragraphs.

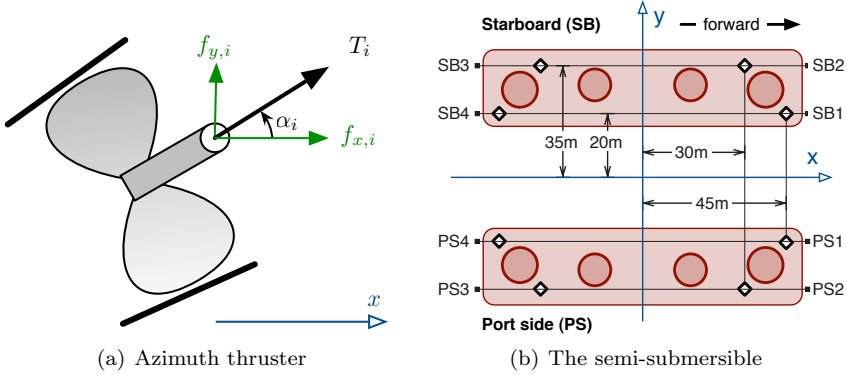


Figure 3.2: Detail of an azimuth thruster with its associated variables in 3.2(a) and a top-view of the actual semi-submersible that was used in the simulations. The azimuth thrusters are located on diamonds in 3.2(b).

Objective function

Cost-efficiency is important when considering the dynamical positioning. Therefore, we try to satisfy the requirements with the least energy possible

$$P_\nu = \sum_{i=1}^N T_i^{2\nu} = \sum_{i=1}^N \left(f_{x,i}^2 + f_{y,i}^2 \right)^\nu. \quad (3.1)$$

Here we assume that each thruster has the same specifications. If not, each term in the sum (3.1) must be scaled with a thruster specific constant $\bar{P}_i/\bar{T}_i^{2\nu}$.

In this report we use the realistic setting of the power $\nu = \frac{3}{4}$. Previously at MARIN, this optimization problem was only considered for $\nu = 1$, because it leads to linear derivatives of (3.1). Simulations have shown that the energy consumption may be lower by about 2% when using the realistic $\nu = \frac{3}{4}$.

Equality constraints

The first set of constraints follows from the need to generate the required force and momentum. If these would not be satisfied, the vessel can start to drift. To avoid this, the following equality constraints must be satisfied:

$$\mathbb{F}_x = \sum_{i=1}^N f_{x,i}, \quad (3.2)$$

$$\mathbb{F}_y = \sum_{i=1}^N f_{y,i}, \quad (3.3)$$

$$\mathbb{M}_z = \sum_{i=1}^N x_i f_{y,i} - y_i f_{x,i}. \quad (3.4)$$

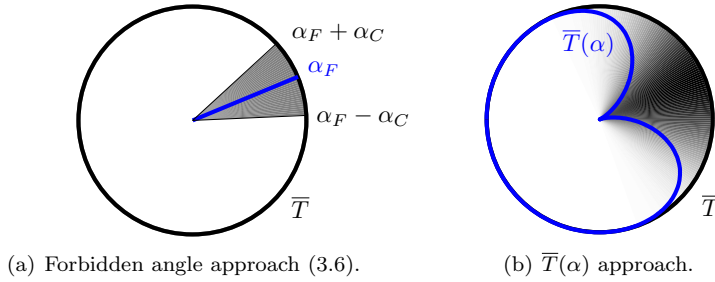


Figure 3.3: Two ways of dealing with disallowed angles. In 3.3(a), certain angles are forbidden, whilst in 3.3(b), the maximal thrust is variable (depending on α), and the intensity of the gray that indicates the available amount of available thrust for each angle α .

Note that these conditions assume that the total installed thruster capacity is sufficient. A more elaborate discussion on this is deferred to Section 3.3.

Inequality constraints

The second set of constraints originates from physical limitations. First of all, the thrusters have a limited capacity⁸ \bar{T}_i . Secondly, thrusters that are close together have an influence on each other: if one is in the stream of the other, its efficiency drops significantly. In order to avoid this, certain angles are prohibited. This results in the following constraints, for $i = 1, \dots, N$:

$$\bar{T}_i \geq T_i = \sqrt{f_{x,i}^2 + f_{y,i}^2}, \quad (3.5)$$

$$|\alpha_i - \alpha_{F,i}| \geq \alpha_{C,i}. \quad (3.6)$$

In this, cf. Figure 3.3(a), $\alpha_{F,i}$ is the center of thruster i 's forbidden zone, the angle that is oriented away⁹ from the neighboring thruster. The constant $\alpha_{C,i}$ gives the minimal angular distance from $\alpha_{F,i}$ needed to avoid influence on the other thrusters. A typical value used for $\alpha_{C,i}$ is about 10 degrees.

An alternative way to describe the inequalities is by using an angular dependent maximal thrust. In this, the maximum thrust in the forbidden regions can be limited to zero. Constraint (3.5) and (3.6) are combined into

$$\bar{T}_i(\alpha_i) \geq T_i. \quad (3.7)$$

This way of describing forbidden angles provides much more freedom and is easy to adapt for the influence of several near by thrusters. A rough example of such an

⁸This is also an approximation because this is the *open water* thrust capacity. Because of currents and interaction with the hull of the boat, the actual thrust might be far less.

⁹We use a thrust notation that shows the direction of the resulting force, while the water is pushed in the opposite direction. Hence the forbidden angles are opposite to the neighboring thruster.

angular dependent maximum thrust $\bar{T}_i(\alpha_i)$ for two neighboring thrusters is given in Figure 3.3(b). Note that it might be convenient to use a smooth continuous differentiable function for this angular dependence.

Full problem statement

The full allocation problem can be summarized as follows:

$$\begin{aligned} & \text{minimize (3.1)} \\ & \text{subject to (3.2), (3.3), (3.4) and} \\ & \quad (3.5), (3.6) \text{ for } i = 1, \dots, N. \end{aligned} \tag{3.8}$$

3.3 Approaches

We are looking for a numerical method to solve the optimization problem described by (3.8) in real time: the computation should be instantaneous compared to the timescales of the vessels actions. Currently, the closed loop control system from Figure 3.1 runs at 4Hz. The method is thus required to take far less than 0.25s, because the allocation is only part of the calculations.

Idea I: Direct nonlinear optimization

With the vast amount of tools available, solving a nonlinear optimization problem is not that difficult. Without considering the efficiency or the computation time, the problem (3.8) can be solved by the MATLAB optimization toolbox. More specifically, `fmincon` was used to gain insight into the behavior of the problem. For this specific setting, the `fmincon` routine used a Sequential Quadratic Programming (SQP) approach for the inner, and line search for the outer loop. The Hessian is updated using a quasi-Newton scheme (more details are available in the MATLAB documentation).

In order to provide a reasonable starting point, the solution of the linearized problem was considered at $t=0$. When ignoring the inequality constraints, problem (3.8) with $\nu=1$ has a quadratic Lagrange function. This leads to a much easier linear problem that can be solved directly.

For subsequent time steps, the result of the previous step were taken as initial value. This is reasonable because of the rather large timescales that are involved with the actual movement of the vessel and external influences like wind and water currents.

Alternative penalty approach for overloaded situations

As mentioned before, there may be times where the thrusters can not produce the requested forces. It is necessary to be aware of this situation and to prioritize the requirements. What is most important the drift avoidance or the energy consumption? In practice, the former is considered to be crucial.

No value can be attributed to the output of `fmincon` when the force and momentum constraints (3.2), (3.3) and (3.4) cannot be met within the thruster capacity

(i.e. (3.5)). It is thus necessary to consider this, undesirable but sometimes unavoidable, case separately. The approach used here is to loosen the constraints on the required forces if the capacity of the thrusters is insufficient. The force/momentum constraints (3.2), (3.3), (3.4) are then dropped, but they are reflected by an additional penalization term in the modified objective function. In particular, we penalize differences between required and provided forces and momentum. Together with the power consumption of the thrusters, this leads to the following modified objective function:

$$\tilde{P}_\nu = w_1 P_\nu + w_2 (\Delta_{\mathbb{F}_x}^2 + \Delta_{\mathbb{F}_y}^2) + w_3 \Delta_{\mathbb{M}_z}^2, \quad (3.9)$$

where w_1 , w_2 and w_3 are weights (to be chosen appropriately), and

$$\begin{aligned} \Delta_{\mathbb{F}_x} &= \mathbb{F}_x - \sum_{i=1}^N f_{x,i}, \\ \Delta_{\mathbb{F}_y} &= \mathbb{F}_y - \sum_{i=1}^N f_{y,i}, \\ \Delta_{\mathbb{M}_z} &= \mathbb{M}_z - \sum_{i=1}^N (x_i f_{y,i} - y_i f_{x,i}). \end{aligned} \quad (3.10)$$

The associated alternative minimization problem, *that is used only when the thrusters have insufficient capacity*, can be written as

$$\begin{aligned} &\text{minimize (3.9)} \\ &\text{subject to (3.5), (3.6) for } i=1, \dots, N. \end{aligned} \quad (3.11)$$

The weights in (3.9) need to be chosen so that the right balance is reached between the energy consumption, drift and orientation changes. Consulting the experts from MARIN led to the use of $w_1=0$: there is no intention of minimizing the power in extreme weather conditions. The other weights were chosen relative to the maximal required thrust and moment for a given time series. This somehow equally treats both position and orientation errors.

Idea II: Reduction to a 3×3 nonlinear system

We will show that, even for the more realistic case where $\nu = \frac{3}{4}$, the $3N+3$ Lagrange equations can be reduced to only 3 equations and the 3 unknown multipliers. The equations obtained from the multipliers technique can be simplified using T_i and α_i , the thrust and azimuth angle of thruster i , as main variables. The associated feasible region then reduces to the product of intervals $T_i \notin [0, \bar{T}_i]$ and $\alpha_i \in [\alpha_{F,i} - \alpha_{C,i}, \alpha_{F,i} + \alpha_{C,i}]$. Solutions will be either inside this domain, as stationary points of the Lagrange function $\Lambda(\mathbf{T}, \mathbf{A}, \mathbf{L})$ (where we collect the thrusts $\mathbf{T} = [T_1, \dots, T_N]^\top$, angles $\mathbf{A} = [\alpha_1, \dots, \alpha_N]^\top$ and Lagrange multipliers $\mathbf{L} = [\lambda_1, \lambda_2, \lambda_3]^\top$ in column vectors) or on the boundary of the domain. These cases are discussed separately.

Solutions in the inside of the feasible region

Using the notation (3.10), the Lagrange function for problem (3.8), assuming that the inequality constraints are inactive, can be written as

$$\Lambda_{\nu=\frac{3}{4}}(\mathbf{T}, \mathbf{A}, \mathbf{L}) = \sum_{i=1}^N T_i^{\frac{3}{2}} - \lambda_1 \Delta_{\mathbb{F}_x} - \lambda_2 \Delta_{\mathbb{F}_y} - \lambda_3 \Delta_{\mathbb{M}_z}. \quad (3.12)$$

For a given thruster i , collecting terms linear in $f_{x,i}$ and $f_{y,i}$ gives $u_i f_{x,i} + v_i f_{y,i}$ where $u_i = \lambda_1 - y_i \lambda_3$ and $v_i = \lambda_2 + x_i \lambda_3$. Using the relations $f_{x,i} = T_i \cos(\alpha_i)$ and $f_{y,i} = T_i \sin(\alpha_i)$, the collected terms are written as $T_i(u_i \cos(\alpha_i) + v_i \sin(\alpha_i))$ and further summarized to $T_i h_i$ using $h_i = u_i \cos(\alpha_i) + v_i \sin(\alpha_i)$. This gives

$$\Lambda_{\nu=\frac{3}{4}}(\mathbf{T}, \mathbf{A}, \mathbf{L}) = \sum_{i=1}^N \left(T_i^{\frac{3}{2}} + T_i h_i \right) - \lambda_1 \mathbb{F}_x - \lambda_2 \mathbb{F}_y - \lambda_3 \mathbb{M}_z. \quad (3.13)$$

In stationary points, the partial derivatives of the Lagrange function $\Lambda_{\nu=\frac{3}{4}}$, with respect to T_i and α_i for each thruster i , must be zero and can be solved:

$$0 = \frac{\partial \Lambda_{\nu=\frac{3}{4}}}{\partial T_i} = \frac{3}{2} \sqrt{T_i} + h_i \quad \Rightarrow \quad T_i = \frac{4}{9} h_i^2, \quad (3.14)$$

$$0 = \frac{\partial \Lambda_{\nu=\frac{3}{4}}}{\partial \alpha_i} = -T_i u_i \sin(\alpha_i) + T_i v_i \cos(\alpha_i) \xrightarrow{T_i \neq 0} \tan(\alpha_i) = \frac{v_i}{u_i}. \quad (3.15)$$

If $T_i = 0$, the thruster i is switched off and any value of α_i is a solution.

With the above, thrust T_i can be rewritten as a function of u_i and v_i :

$$h_i = \pm u_i \underbrace{\left(\frac{u_i}{\sqrt{u_i^2 + v_i^2}} \right)}_{\cos(\alpha_i)} \pm v_i \underbrace{\left(\frac{v_i}{\sqrt{u_i^2 + v_i^2}} \right)}_{\sin(\alpha_i)} = \pm \sqrt{u_i^2 + v_i^2}. \quad (3.16)$$

Both T_i and α_i depend only on the Lagrange multipliers λ_1, λ_2 and λ_3 . The stationary points are thus characterized by the multipliers, that can be found by substitution T_i and α_i into the equality constraints (3.2), (3.3) and (3.4):

$$\begin{cases} \mathbb{F}_x = \sum_{i=1}^N T_i \cos(\alpha_i) & = \frac{4}{9} \sum_{i=1}^N h_i u_i, \\ \mathbb{F}_y = \sum_{i=1}^N T_i \sin(\alpha_i) & = \frac{4}{9} \sum_{i=1}^N h_i v_i, \\ \mathbb{M}_z = \sum_{i=1}^N T_i (x_i \sin(\alpha_i) - y_i \cos(\alpha_i)) & = \frac{4}{9} \sum_{i=1}^N h_i (x_i v_i - y_i u_i). \end{cases} \quad (3.17)$$

These are thus three equations for the three unknown multipliers λ_1, λ_2 and λ_3 . When such a stationary point exists inside the domain, the optimal value of the power P is then equal to $\sum_{i=1}^N T_i^{\frac{3}{2}} = \frac{8}{27} \sum_{i=1}^N h_i^3$.

Solutions on the boundary: saturation and forbidden angles

With the Lagrange multipliers technique, it is possible to take inequalities into account, introducing a new multiplier μ_j for each inequality. Derivations lead to the following conclusion: either inequality j becomes an equality (border of the domain) or $\mu_j = 0$. Hence, inside the domain all μ_j vanish and the extended Lagrange function is equal to the previous $\Lambda = \Lambda_{\nu=\frac{3}{4}}$.

On a border, optimizing the total power can also be done by the multiplier technique using the restriction of Lagrange function Λ to this border of the domain. As the domain is expressed as boundary values for T_i and α_i , the restriction of Λ to a border amounts to fixing the value of T_i (resp. α_i) in Λ . Hence all previous derivations remain valid excepted $\frac{\partial \Lambda}{\partial T_i}$ (resp. $\frac{\partial \Lambda}{\partial \alpha_i}$) that is no longer needed to determine T_i (resp. α_i) as a function of the λ 's. Observe that when T_i is saturated, equation $\frac{\partial \Lambda}{\partial \alpha_i} = 0$ still allows to determine $\alpha_i = \arctan\left(\frac{v_i}{u_i}\right)$ and conversely, if α_i is a forbidden angle, equation $\frac{\partial \Lambda}{\partial T_i} = 0$ still allows to determine $T_i(\lambda_1, \lambda_2, \lambda_3)$. Finally, if for some i , both T_i and α_i reach boundary values, then the allocation problem is reduced to a problem with $N - 1$ thrusters and new known constraints ($\mathbb{F}_x := \mathbb{F}_x - f_{x,i}$, and similar for \mathbb{F}_y and \mathbb{M}_z) and it reduces to the same system of 3 equations for a subset of indices in the summations.

Idea III: Iteration on a linearized Lagrange problem

For this strategy, we distinguish a simplified version of the problem and the full problem. By first solving a simplified version, an initial estimate of the solution is obtained. This can be used in an iterative algorithm which adapts the simple version to obtain improved versions. A few of these defect correction type iterations yield the final solution.

The simplified problem ($\nu = 1$)

We simplify the optimization problem (3.8) by taking $\nu = 1$ and the angular dependent maximal thrust constraint (3.7) instead of constraints (3.5) and (3.6):

$$\begin{aligned} & \text{minimize (3.1) for } \nu = 1 \\ & \text{subject to (3.2), (3.3), (3.4) and} \\ & \quad (3.7) \text{ for } i = 1, \dots, N. \end{aligned} \tag{3.18}$$

Denoting \mathcal{J} as the set of indices j for which thruster j is saturated, e.g. inequality (3.7) becomes an equality, using vectors $\mathbf{F} = [f_{x,1}, f_{y,1}, \dots, f_{x,N}, f_{y,N}]^\top$, $\mathbf{M} = \{\mu_j\}_{j \in \mathcal{J}}$ and $\mathbf{L} = [\lambda_1, \lambda_2, \lambda_3]^\top$, the Lagrange function becomes

$$\begin{aligned} \Lambda_{\nu=1}(\mathbf{F}, \mathbf{L}, \mathbf{M}) = & P_{\nu=1} - \lambda_1 \Delta_{\mathbb{F}_x} - \lambda_2 \Delta_{\mathbb{F}_y} - \lambda_3 \Delta_{\mathbb{M}_z} \\ & - \sum_{j \in \mathcal{J}} \mu_j \left(\bar{T}_j(\alpha_j)^2 - f_{x,j}^2 - f_{y,j}^2 \right). \end{aligned} \tag{3.19}$$

Now we can find \mathbf{F} , \mathbf{L} , and \mathbf{M} such that $(\mathbf{F}, \mathbf{L}, \mathbf{M})$ is a stationary point for the Lagrange function (3.19), by solving the following system (for notational convenience,

where \mathbf{C} is an diagonal matrix of dimension $2N \times 2N$; the matrix \mathbf{E} is $3 \times 2N$ and the matrix \mathbf{B} is $k \times 2N$, where k is the number of indices in \mathcal{J} , that is the number of inequalities (3.7) that is reduced to equalities (i.e. the number of saturated thrusters).

In the initial step we assume none of the constraints (3.7) is active, i.e. $\mathcal{J} = \emptyset$. This implies that in the initial step the rows and columns with \mathbf{B} , \mathbf{L} and $\hat{\mathbf{T}}$ are absent from (3.21). So we solve the system (3.21) for \mathbf{F} and \mathbf{L} to find the estimate $\mathbf{F}^{[0]}$.

As soon as an estimate $\mathbf{F}^{[m]}$ is available we can compute the thrusts T_i

$$T_i = \bar{T}_i \left(\arctan \left(\frac{(f_{y,i})^{[m]}}{(f_{x,i})^{[m]}} \right) \right) \quad \text{for } i = 1, \dots, N \quad (3.22)$$

and find \mathcal{J} , the set of indices j for which the constraints (3.7) is violated. For those indices, we scale that vector so that the trust is equal to the maximum:

$$f_{x,j} := \frac{\bar{T}_j(\alpha_i)}{T_j} f_{x,j} \quad \text{and} \quad f_{y,j} := \frac{\bar{T}_j(\alpha_i)}{T_j} f_{y,j}. \quad (3.23)$$

If $\mathcal{J} \neq \emptyset$ we compute \mathbf{B} , \bar{T}_i and $\hat{\mathbf{T}}$, using $\mathbf{F}^{[m]}$, and solve the system (3.21) again. The iterative process ends when the set \mathcal{J} does not change any more¹⁰.

After the first iteration, instead of system (3.21) with the artificial $\nu = 1$, it is more realistic to solve the system that will be described in the following.

The true, non-simplified problem ($\nu = \frac{3}{4}$)

In order to remove the simplification made in Section 3.3 by setting $\nu = 1$ instead of $\nu = \frac{3}{4}$ in the expression P_ν , we have to correct for it. The function P_ν was the original object function for optimization, and the value of ν is reflected in the system (3.21) only in the \mathbf{C} . In fact \mathbf{C} is the Hessian of P , which is constructed to make the gradient of P vanish.

Namely, for $\nu = 1$ the gradient of $P_{\nu=1}$ reads

$$\nabla P_{\nu=1}(\mathbf{F}) = \frac{\partial P_{\nu=1}}{\partial \mathbf{F}} = 2(f_{x,1}, f_{y,1}, f_{x,2}, f_{y,2}, \dots, f_{x,N}, f_{y,N})^\top \quad (3.24)$$

and the equations $\mathbf{C}\mathbf{F} = 0$ make the gradient vanish.

If $\nu = \frac{3}{4}$ the gradient can be written with \div , an element-wise division

$$\nabla P_{\nu=3/4}(\mathbf{F}) = \frac{\partial P_{\nu=3/4}}{\partial \mathbf{F}} = \frac{3}{2} \mathbf{F} \div [\sqrt{T_1}, \sqrt{T_1}, \sqrt{T_2}, \sqrt{T_2}, \dots, \sqrt{T_N}, \sqrt{T_N}]^\top.$$

Applying the defect correction principle [1], we compute the true problem by replacing the system (3.21) by

$$\begin{bmatrix} \mathbf{C} & \mathbf{B}^\top & \mathbf{E}^\top \\ \mathbf{B} & \mathbf{0} & \mathbf{0} \\ \mathbf{E} & \mathbf{0} & \mathbf{0} \end{bmatrix} \begin{bmatrix} \mathbf{F} \\ \mathbf{M} \\ \mathbf{L} \end{bmatrix} = \begin{bmatrix} \nabla P_{\nu=1}(\mathbf{F}) - \nabla P_{\nu=3/4}(\mathbf{F}) \\ \hat{\mathbf{T}}^2 \\ \mathbf{R} \end{bmatrix}, \quad (3.25)$$

¹⁰Because of the weak non-linearity of the system, a nice convergence behavior of the iteration is expected.

so that the iterative improvement of the solution of the problem we are interested in, is achieved by solving for $\mathbf{F}^{[m+1]}$ from the system

$$\begin{bmatrix} \mathbf{C} & \mathbf{B}^{[m]\top} & \mathbf{E}^\top \\ \mathbf{B}^{[m]} & \mathbf{0} & \mathbf{0} \\ \mathbf{E} & \mathbf{0} & \mathbf{0} \end{bmatrix} \begin{bmatrix} \mathbf{F}^{[m+1]} \\ \mathbf{M} \\ \mathbf{L} \end{bmatrix} = \begin{bmatrix} \nabla P_{\nu=1}(\mathbf{F}^{[m]}) - \nabla P_{\nu=3/4}(\mathbf{F}^{[m]}) \\ \hat{\mathbf{T}}^{[m]^2} \\ \mathbf{R} \end{bmatrix}, \quad (3.26)$$

for $m=0,1,2,\dots$. Upon convergence, this leads to the stationary point of (3.19) with $\nu=\frac{3}{4}$, hence to the solution of the full optimization problem.

3.4 Results

The optimization using `fmincon` was used to solve the allocation problem for a sequence of \mathbb{F}_x , \mathbb{F}_y and \mathbb{M}_z , provided by MARIN. The resulting thrusts T_i and orientations α_i are plotted for the first 250 seconds in Figure 3.4-3.5, where the second figure uses the modified algorithm with the robust handling of the overloaded situation (see Section 3.3).

The baseline implementation took on average 0.15s per iteration for the given sequence. This was reduced to about 0.03s by optimizing the code and by providing some of the derivatives analytically (profiling showed that the finite difference approximations of this derivatives took most of the time).

We tried to mimic the approach that MARIN uses nowadays (with $\nu=1$). It is unclear if this is exactly identical to their program (there is no way of verifying due to confidentiality of their actual results). Our implementation, in which we use the realistic value $\nu=\frac{3}{4}$, proved to require about 2% less power on average than when considering the previously used quadratic objective function ($\nu=1$). It is clearly worth considering the realistic case with $\nu=\frac{3}{4}$: in some time steps, the excess power for $\nu=1$ reached up to 5% of our optima.

In order to facilitate the interpretation, a MATLAB visualization was written to show the thrust together with their orientation (see Figure 3.6). By joining static plots for the given sequence of required values, a movie was made. It allows for a very natural way of inspecting the results because the human eye is able to see trends, even for several thrusters simultaneously. Waves for example, can easily be spotted in this manner because all thrusters re-orient in a similar fashion. This video also shows the required and achieved forces and moments. Violations of the constraints are indicated by the use of color, as explained in Figure 3.6. For the time being, the visualization is specialized for the azimuthal thrusters, but it can be extended to other type of actuators, as can the analysis in Section 3.3.

3.5 Recommendations

If the speed and quality of the straight forward MATLAB implementation is sufficient, this optimization routine can be used in the software with minimal effort. If not, the other approaches should be investigated further.

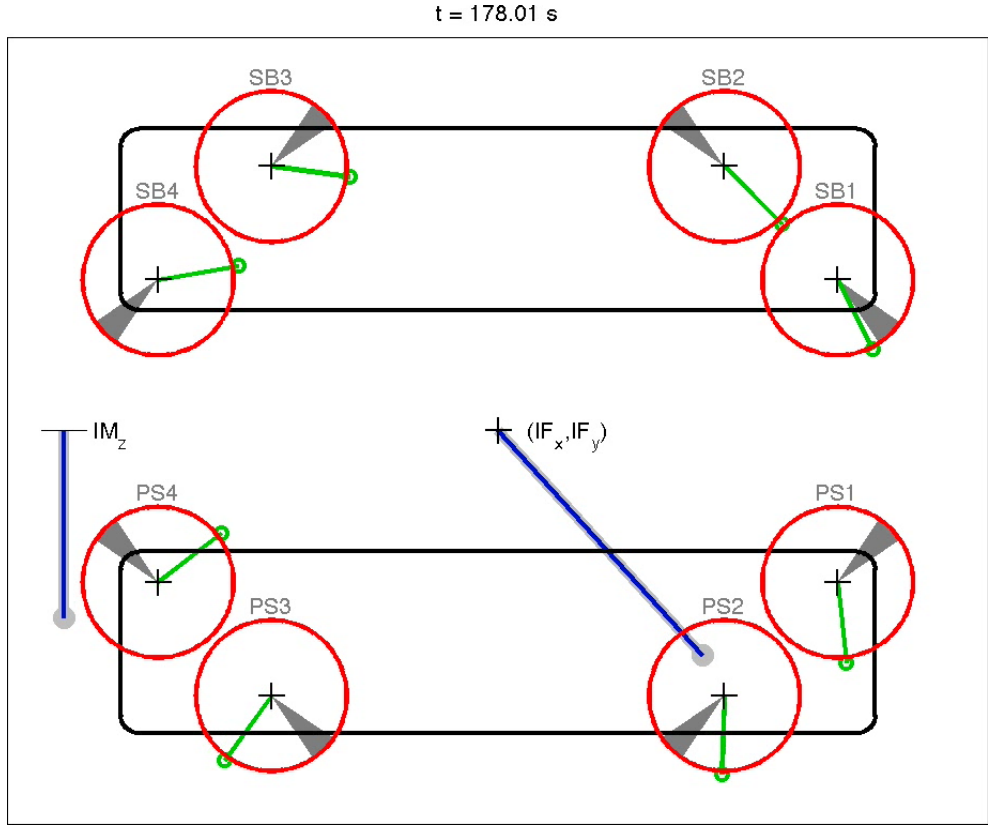


Figure 3.4: Resulting thrust and orientation for the direct nonlinear optimization (Section 3.3) for a given sequence of requested force and momentum. Each plot represents one of the eight thrusters on starboard (SB) and port side (PS). The left axis shows the thrust T_i with an indication of the maximum \bar{T}_i (at some points in time, the thrusters are indeed overloaded), the right axis shows the azimuth angle α_i and the forbidden angle range $[\alpha_{F,i} - \alpha_{C,i}, \alpha_{F,i} + \alpha_{C,i}]$ (only within visible range for thruster 'PS3').

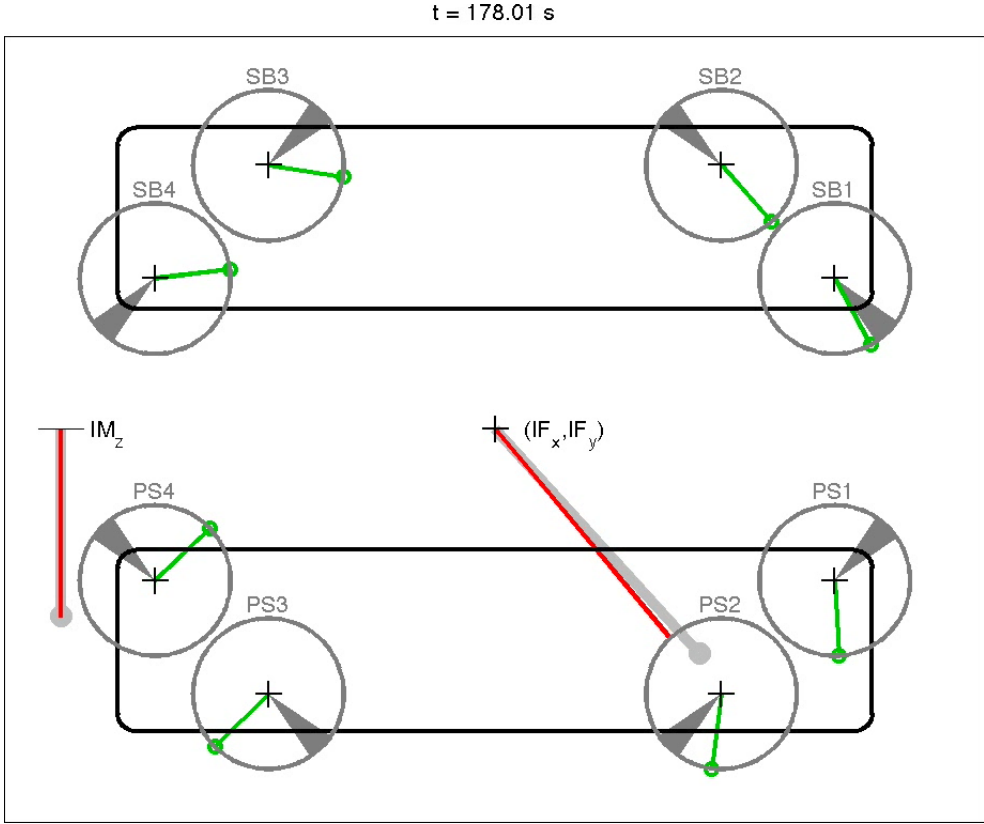
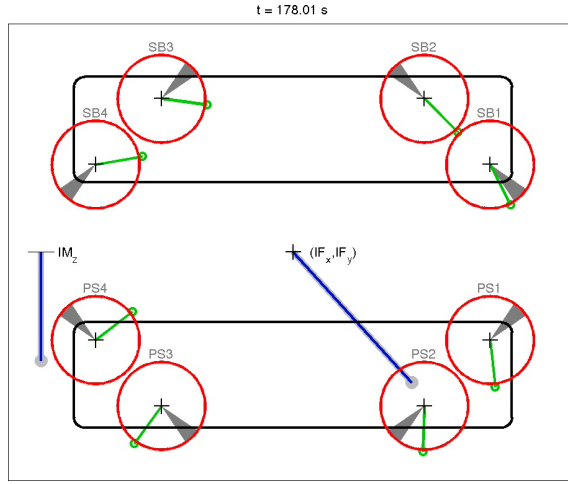


Figure 3.5: Identical setup as in Figure 3.4, but with results for the approach in which the penalty function formulation is used in case the thrusters are overloaded. This avoids overloading, as can be seen in the graphs, by loosening the constraint on the required force and momentum (see Section 3.3).

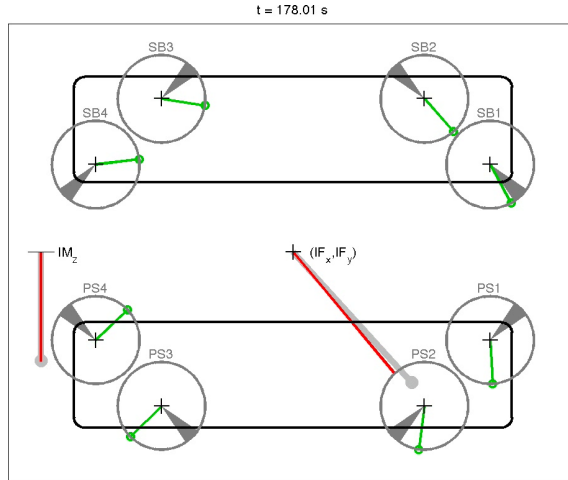
The use of the thrust/angle notation proved to reduce the complexity of the problem quite dramatically to only 3 equations with as many unknowns. Using this in the software could result in another significant speedup.

The iterative method with linearized Lagrange problem seems a promising algorithm. It should only require about 4 or 5 iterations to find a sufficiently accurate solution. However, during the workshop, we had no time to make an implementation and thus have no results at the time of writing.

It should be noted that optimizing only the allocation block in Figure 3.1 might not be ideal. A model-predictive approach, that combines the EKF, PID and allocation units might lead to even better results. Another important aspect of this approach would be the concept of time horizon: the power can be minimized over a given period, the next two hours for example. However, this would require a full model of the vessel, together with models for the wind and the waves. This is not that



(a) Still image from the visualization of the direct nonlinear optimization from Section 3.3. At this moment, the thrusters are overloaded as indicated by the red circles that show the maximal thrust and the thrust vectors that are longer than that radius.



(b) Still image from the visualization for the nonlinear optimization with special handling of the overloaded thruster situation as explained in Section 3.3. At this time, the thrusters would be overloaded, as shown in 3.6(a). So the alternative approach with penalty function is used: instead of overloading the thrusters, the required force and momentum constraint is loosened and matched as closely as possible given the available capacity.

Figure 3.6: MATLAB visualization of the resulting thrusters settings. The required (gray) and achieved (blue, red if not produced) total force (F_x, F_y) and moment M_z are shown, together with all the thruster forces of this semi-submersible. The constraints are also shown: filled sections show the forbidden angles and the circle's radius is the maximum thrust capacity. If constraints are violated, the corresponding section or circle is shown in red.

straightforward.

3.6 References

- [1] K Böhmer, P Hemker, and H J Stetter. The defect correction approach. In *Defect Correction Methods. Theory and Applications*, pages 1–32. Springer-Verlag, 1984.
- [2] Jorrit-Jan Serraris. Time domain analysis for dp simulations. *ASME Conference Proceedings*, 2009(43413):595–605, 2009.

Report 4

Modeling and Optimization of Algae Growth

Authors:¹ Anthony Thornton², Thomas Weinhart², Onno Bokhove², Bowen Zhang³, Dick M. van der Sar⁴, Kundan Kumar⁵, Maxim Pisarenco⁵, Maria Rudnaya⁵, Valeriu Savcenco⁵, Jens Rademacher⁶, Julia Zijlstra⁶, Alicja Szabelska⁷, Joanna Zyprych⁷, Martin van der Schans⁸, Vincent Timperio⁸, Frits Veerman⁸

Abstract

The wastewater from greenhouses has a high amount of mineral contamination and an environmentally-friendly method of removal is to use algae to clean this runoff water. The algae consume the minerals as part of their growth process. In addition to cleaning the water, the created algal bio-mass has a variety of applications including production of bio-diesel, animal feed, products for pharmaceutical and cosmetic purposes, or it can even be used as a source of heating or electricity.

The aim of this paper is to develop a model of algae production and use this model to investigate how best to optimize algae farms to satisfy the dual goals of maximizing growth and removing mineral contaminants.

With this aim in mind the paper is split into five main sections. In the first a review of the biological literature is undertaken with the aim of determining what factors effect the growth of algae. The second section contains a review of exciting mathematical models from the literature, and for each model a steady-state analysis is performed. Moreover, for each model the strengths and weaknesses are discussed in detail. In the third section, a new two-stage model for algae production is proposed, careful estimation of parameters is undertaken and numerical solutions are presented. In the next section, a new one-dimensional spatial-temporal model is presented, numerically solved and optimization strategies are discussed. Finally, these elements are brought together and recommendations of how to continue are drawn.

4.1 Introduction

Greenhouses produce large amounts of mineral rich runoff water that needs to be treated to avoid ground-water contamination. The contaminants are mostly fertilisers such as nitrogen and phosphorus. It is both an environmental challenge and a legal requirement to avoid such contamination. A simple and efficient treatment to lower the nutrient concentration is to grow algae in shallow outdoor racetrack ponds, which are cheap and easy to maintain. This problem was presented by Phytocare who wants to achieve the following goals: To prove that algae cultures can clean runoff water; to

¹Other participants: Amit Smotra, Katarzyna Marczyńska, Vivi Rottschäfer.

²Universiteit Twente, Enschede

³Delft University of Technology

⁴Phytocare, Berkel en Rodenrijs

⁵Technische Universiteit Eindhoven

⁶Centrum Wiskunde & Informatica, Amsterdam

⁷Poznan University of Life Sciences, Dabrowskiego, Poland

⁸Leiden University

obtain experience in growing algae cultures and develop protocols for industrial scale production; and to work toward producing an economically valuable product from the runoff water. This could be the start toward a new sustainable economic activity for greenhouse builders.

To grow algae, one requires not only nutrients but a supply of energy, which is provided by sunlight. The photosynthesis process converts photonic energy and carbon dioxide into glucose, or sugar. Thus, the pond requires an inflow of runoff water from the greenhouses as well as a pump that maintains a specified amount of carbon dioxide in the pool. The pond is continuously mixed to allow for homogeneous growth conditions and algae is continuously removed by ‘sieving’ the water, see figures 4.1 and 4.2.

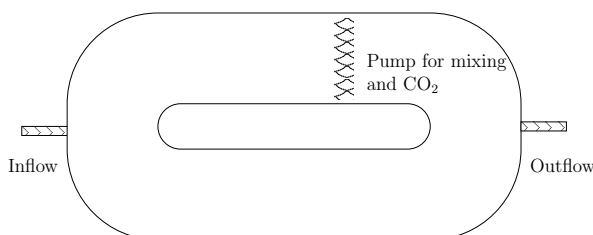


Figure 4.1: Schematic of a racetrack pond. Photos of the key parts can be seen in figure 4.2.

Algae not only remove the contaminants from water, but are an extremely important resource in many fields of industry. On the one hand, they can be employed for production of bio-diesel and bio-ethanol. On the other hand they form an important food source for shellfish or other animals. In addition, they are commercially cultivated for pharmaceutical and cosmetic purposes as well as to produce biomass, which is subsequently exploited to create heat and electricity. This wide variety of applications of algae explains the interest in controlling their growth.

The remainder of this paper is split into four sections. In the second section an hierarchy of exciting models from the literature is reviewed. For each model an equilibrium point analysis is undertaken and the limitations are discussed. In the third section a new two-stage ordinary differential equation model that considers the evolution of carbon, sugar, nutrients and algae is presented. Careful estimates for the parameters are obtained using a combination of the literature reviewed above and temporal averages of the equations. The fourth section presents an alternative partial differential equations model, which considers the depth and temporal evolution of two separate nutrients (phosphates and nitrates), carbon dioxide and algae growth. Numerical solutions are presented and a discussion of how to optimize the algae growth is undertaken. In the final section all these models and approaches are compared and contrasted, and then the factors that affect the growth of algae are discussed.



Figure 4.2: Images of an algae farm owned by Ingrepo: Top left, overview of the racetrack pond; top right, close up of the mixing device; bottom left, algae extraction apparatus; bottom right, bagged dry algae. Images reproduced with permission of Ingrepo, Borculo, The Netherlands. Website www.ingrepo.nl. Photos taken by V.R. Ambati.

Brief review of existing literature

Before discussing mathematical models, we will briefly review some of the biological literature on the growth of algae; including a study of the conditions for optimizing the growth of algae and the removal of contaminants. We explain this process in terms of environmental conditions. The most important parameters regulating algal growth are temperature, nutrient quantity and quality, intensity of light, levels of CO_2 and O_2 , pH and salinity. Knowledge about the influence and ranges of these parameters will help us to promote algae growth. The temperature of water as well as the nutrients content must be on the level that will allow the algae to grow [9]. The optimal temperature for phytoplankton cultures is generally between $20^\circ C$ and $30^\circ C$. Ranges for nutrients are presented in [12] and [6], whereas content of specific elements with focus on nitrogen and phosphorus is described in [15]. Since algae are photo-synthetic organisms, there is a need to set the cultures in areas of varying temperatures but with sufficient light to promote photosynthesis. Photosynthesis

depends also on the light intensity and frequency. The photo-synthetic rate is proportional to irradiance and the higher the irradiance, the longer the dark period that can be afforded by the system without loss of growth [20]. Optimal light intensity for algae is 2,500-5,000 lux. According to Vonshak et al. [31], growth of algae becomes saturated at a range of $150 - 200 \mu\text{mol photon } m^{-2}s^{-1}$. For a high photosynthesis rate balance between CO_2 and O_2 has to be taken into consideration [27]. In addition, Pulz in [27] described that species-specific O_2 evolution rates were recorded between 28 and 120 mg $O_2/(gDW h^{-1})$ in high-cell-density micro-algal cultures with optimum growth; whereas, Cheng et al. [6] studied the CO_2 concentration during algal growth and determined that the proper range is 0.8%-1.0%. Deviations from the optimum pH and salinity will cause productivity problems. Therefore optimum conditions should be maintained. The pH value for optimum growth of algae ranges between 7-12. Every algal species has a different optimum salinity range [4]. Paasche et al. [24] found a salinity range of 10 to 34 ppt for growth of clones of *Emiliana huxleyi*.

4.2 A hierarchy of models and some qualitative analysis

In this section we describe a hierarchy of increasingly complex, minimal models for light and nutrient limited algae growth which may serve as building blocks for more detailed models. All model ingredients were taken from the literature. The light-limitation is a crude model for the influence of photosynthesis on growth, lumped into a few parameters that would need to be gauged by measurements or extended by more detailed model components. This holds similarly for other influences, such as CO_2 , pH value, etc. In the models presented in this section, we do not specify values for such parameters but rather investigate the qualitative dynamics of the algae growth and its interpretation.

We start with the purely light limited scalar model derived by Huisman et al in [12]. Inspired by the model in [10], see also [9], we extend this model by including two nutrients and a temperature dependence, but keep a scalar model. We then move on to a model by Klausmeier ([17, 16]) for nutrient-limited growth where nutrient densities are variable, and where intra- and extracellular densities are distinguished. Lastly, we combine this with the light-limitation model by Huisman ([12]).

The Huisman model: light-limited, nutrient surplus

This model has been derived in [12] and gives the density of algae $\mathcal{A}(t) \geq 0$ through the scalar ordinary differential equation

$$\frac{d}{dt}\mathcal{A} = \mathcal{H}(\mathcal{A}) := \overbrace{\frac{\mu_{\max}}{z_{\max}} \ln \left(\frac{H_P + I_{\text{in}}}{H_P + I_{\text{out}}} \right)}^{\text{gain}} \frac{\mathcal{A}}{k\mathcal{A} + K_{\text{bg}}} - \overbrace{h_r\mathcal{A} - D_r\mathcal{A}}^{\text{loss}}. \quad (4.1)$$

The parameters of the model can be roughly grouped into external, somewhat controllable, and internal, algae dependent parameters. All of these also depend to varying degrees on CO_2 , pH value, temperature, nutrients, etc.

External parameters		Internal parameters	
incoming light:	I_{in}	maximum specific growth rate:	μ_{max}
outgoing light:	I_{out}	half saturation of photosynthesis:	H_P
background turbidity:	K_{bg}	specific light attenuation:	k
mixing depth:	z_{max}	specific maintenance (death rate):	D_r
dilution / outflow:	h_r		

One of the main aspects of the model is that, even in the presence of mixing, the light intensity decays with depth due to ‘shading’ by algae above. For the above spatial average model this means:

$$I_{\text{out}} = I_{\text{in}} \exp(-(k\mathcal{A} + K_{\text{bg}})z_{\text{max}}).$$

In [12] the form of the growth rate \mathcal{H} is compared with ecological reality. For instance the inverse proportionality with respect to z_{max} suggests that shallow tanks are better for growth, which is well known in practice. Note that here this effect is given by a quantitative scaling law, and, for instance halving z_{max} has much greater effect than doubling I_{in} . We shall investigate some other qualitative predictions of this model.

Steady state analysis. The qualitative behaviour of a scalar ordinary differential equation is essentially determined by the location and stability of steady states, where $\mathcal{H}(\mathcal{A}) = 0$: the flow is monotone on intervals between equilibria with direction compatible with the (necessarily changing) stability of these equilibria. It is convenient to rewrite (4.1) in steady-state as

$$\mu_{\text{max}} \ln \left(\frac{H_P + I_{\text{in}}}{H_P + I_{\text{out}}(\mathcal{A})} \right) = z_{\text{max}}(k\mathcal{A} + K_{\text{bg}})(h_r + D_r), \quad (4.2)$$

where we divided by \mathcal{A} , to remove the trivial steady state $\mathcal{A} = 0$. The relative value of left and right hand sides (LHS, RHS) of this equation determines growth via

$$\frac{d}{dt}\mathcal{A} > 0 \Leftrightarrow \text{LHS} > \text{RHS}. \quad (4.3)$$

We first observe that LHS saturates for growing \mathcal{A} to the asymptotic state, $\mu_{\text{max}} \ln \left(\frac{H_P + I_{\text{in}}}{H_P} \right)$, while RHS is growing linearly. This implies that for sufficiently large \mathcal{A} we always have $\frac{d}{dt}\mathcal{A} < 0$ which makes intuitive sense as we expect that very large amounts of algae cannot be maintained.

Since the model is scalar, this decay can only be stopped by a steady state, which, in absence of positive steady states means $\mathcal{A} = 0$. The left and right hand sides at the state without algae satisfy:

LHS at $\mathcal{A} = 0$:

$$\begin{aligned} \text{Value:} & \quad \mu_{\text{max}} \ln \left(\frac{H_P + I_{\text{in}}}{H_P + I_{\text{in}} \exp(-K_{\text{bg}}z_{\text{max}})} \right) \\ \text{Slope:} & \quad \mu_{\text{max}} z_{\text{max}} \frac{I_{\text{in}} \exp(-z_{\text{max}}K_{\text{bg}})}{H_P + I_{\text{in}} \exp(-z_{\text{max}}K_{\text{bg}})} \end{aligned}$$

RHS at $\mathcal{A} = 0$:

$$\begin{aligned} \text{Value:} & \quad z_{\text{max}} K_{\text{bg}} (h_r + D_r) \\ \text{Slope:} & \quad z_{\text{max}} k \mathcal{A} (h_r + D_r) \end{aligned}$$

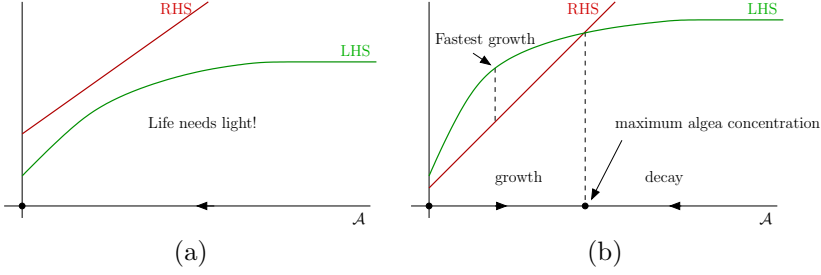


Figure 4.3: Configurations without stable steady state (a) and mono-stability (b). Arrows on the horizontal \mathcal{A} -axis indicate the direction of growth. Bullets are steady states.

We infer that $\mathcal{A}=0$ is the only steady state if the light intensity I_{in} is very small or if the depth z_{max} is very large. Again, this makes intuitive sense as ‘life need light’ to overcome depletion and natural death. The algebraic criterion for this is cumbersome and does not provide much insight. A relatively simple sufficient criterion for the existence of another steady state above $\mathcal{A}=0$ is that the value of LHS at $\mathcal{A}=0$ is bigger than that of RHS:

$$\mu_{\text{max}} \ln \left(\frac{H_P + I_{\text{in}}}{H_P + I_{\text{in}} \exp(-K_{\text{bg}} z_{\text{max}})} \right) > z_{\text{max}} K_{\text{bg}} (h_r + D_r). \quad (4.4)$$

As mentioned, this holds for large I_{in} , or for small z_{max} and K_{bg} i.e. a clean shallow tank, and can be somewhat controlled by small depletion (harvest) rate h_r .

Geometrically, steady states are intersection points of the graphs of LHS and RHS, see Figure 4.3. Since LHS is concave and RHS linear, under criterion (4.4) there is a single non-zero positive steady state. Since \mathcal{A} larger than this implies decay as noted above, this steady state is stable, that is, when perturbing the amount of biomass the growth dynamics will be driven back to this state. This configuration may be called ‘mono-stable’ as the state without algae is unstable, which is ecologically perhaps unrealistic as it implies that even the smallest initial amount of algae suffices for stable growth up to a ‘carrying capacity’. Note that the geometry implies that there is a single point of fastest growth, which means that a slowing of growth implies that the reactor is roughly halfway to its carrying capacity state.

The other possible configuration with positive carrying capacity is plotted in Figure 4.4. Here the initial amount of algae concentration has to lie above a threshold value to trigger growth until the carrying capacity state.

Huisman Model with nutrient limitation

As a first step to incorporate nutrient limitation we include a nutrient concentration dependent factor in the gain term, similar to the model in [10]. Denoting the amount of nitrogen and phosphorus as N and P , we assume for this factor the typical

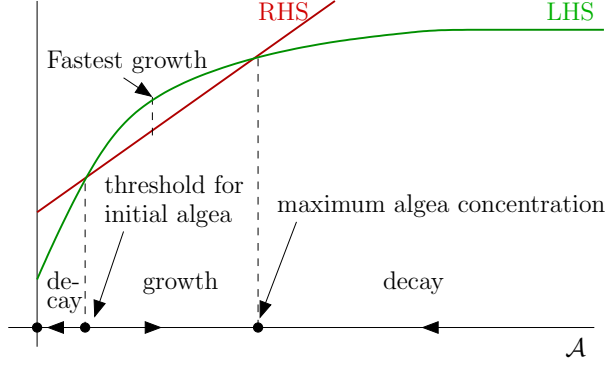


Figure 4.4: Typical dynamics of the Huisman model.

saturation form

$$\frac{P}{(H_P + \xi_P P)} \frac{N}{(H_N + N)}$$

known from generic growth models, where H_N , H_P are the half saturation parameters. To close the system, we assume instantaneous nutrient adaption

$$P = P_{\text{Tot}} - \alpha \mathcal{A}, N = N_{\text{Tot}} - \beta \mathcal{A},$$

where $P_{\text{Tot}}, N_{\text{Tot}}$ is the total influx of nutrients and α, β environmental parameters measuring the uptake into algae concentration.

It has been reported in the literature [5] that growth is more sensitive to Phosphorus, which we crudely model by taking the parameter $0 \leq \xi_P < 1$. For simplicity, we initially set $\xi_P = 0$, so that the resulting model becomes invalid for large amount of P .

In addition, and mainly for illustration, we follow [10], see also [9], to include simple forms of temperature (T) dependence with respect to a reference temperature T_{ref} and rates θ_j , $j = 1, 2$.

$$\begin{aligned} \frac{d}{dt} \mathcal{A} = & \frac{\mu_{\max}}{z_{\max}} \ln \left(\frac{H_P + I_{\text{in}}}{H_P + I_{\text{out}}} \right) \frac{\mathcal{A}}{(k\mathcal{A} + K_{\text{bg}})} \\ & \times \theta_1^{T - T_{\text{ref}}} \frac{P}{(H_P + \xi_P P)} \frac{N}{(H_N + N)} \\ & - D\mathcal{A} - D_r \theta_2^{T - T_{\text{ref}}} \mathcal{A}. \end{aligned}$$

Steady state analysis for $\xi_P = 0$. As above we pursue a steady state analysis and divide out $\mathcal{A} = 0$, which now gives

$$\frac{\mu_{\max} \theta_1^{T - T_{\text{ref}}}}{z_{\max} (D + D_r \theta_2^{T - T_{\text{ref}}})} \ln \left(\frac{H_P + I_{\text{in}}}{H_P + I_{\text{out}}} \right) = \frac{(k\mathcal{A} + K_{\text{bg}})(H_N + N_{\text{Tot}} - \beta \mathcal{A})}{(P_{\text{Tot}} - \alpha \mathcal{A})(N_{\text{Tot}} - \beta \mathcal{A})}.$$

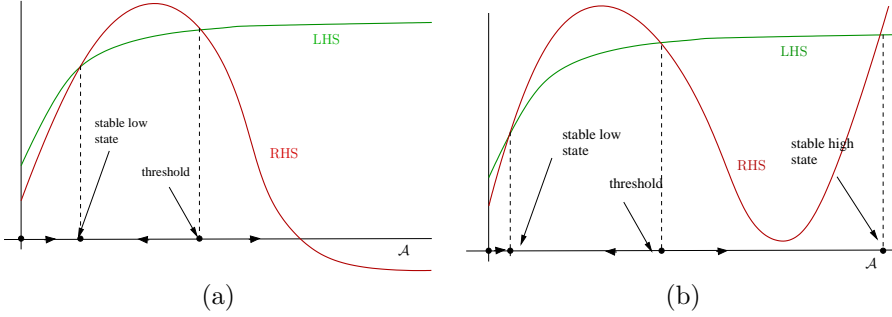


Figure 4.5: Sketches of possible configurations for the extended Huisman model with nutrient limitation. (a) $\xi_P = 0$, (b) $0 > \xi_P \leq 1$.

In essence, the left hand side is the same as in (4.2), but the right hand side is no longer affine. Instead, it has the shape sketched in Figure 4.5(a), and in particular has the negative asymptotic value $-k/\alpha$.

Therefore, large values of \mathcal{A} imply $\frac{d}{dt}\mathcal{A} > 0$, which would mean unbounded growth. This is of course unrealistic, but as mentioned, the model becomes invalid for large values of \mathcal{A} . We infer that, within the range of validity, the largest steady state is always unstable, and may be $\mathcal{A} = 0$ in which case any initial amount of algae will grow (and eventually lie outside the range of validity).

The most interesting case is when there exists a positive *stable* ‘low’ steady state, which (to be consistent) implies the presence of a larger *unstable* ‘threshold’ steady state. This would mean that starting with initial algae below this larger unstable state and above any potential low threshold states, the reactor would always converge towards the low stable state. It would thus not reach its potential, which is an algae concentration so large that it is outside the range of this model.

One way to drive the reactor beyond the high threshold value would be control of the parameters, which is, however, beyond the scope of this article.

We note that it is for instance also possible that, geometrically, RHS lies below LHS everywhere, which implies unbounded growth for any amount of initial algae.

Steady state analysis for $0 < \xi_P < 1$. In this case the steady state equation reads

$$\frac{\mu_{\max}\theta_1^{T-T_{\text{Ref}}}}{z_{\max}(D+D_r\theta_2^{T-T_{\text{Ref}}})} \ln\left(\frac{H_P+I_{\text{in}}}{H_P+I_{\text{out}}}\right) = \frac{(k\mathcal{A}+K_{\text{bg}})(H_N+N_{\text{Tot}}-\beta\mathcal{A})(H_P+P_{\text{Tot}}-\alpha\mathcal{A})}{(P_{\text{Tot}}-\alpha\mathcal{A})(N_{\text{Tot}}-\beta\mathcal{A})}.$$

The main difference compared to $\xi_P = 0$ is that now the RHS asymptotically grows linearly, so that for large values of \mathcal{A} we have the more realistic case $\frac{d}{dt}\mathcal{A} < 0$. As in the original model, this implies that the largest steady state is stable (which may be $\mathcal{A} = 0$). Qualitatively, and for small $\xi_P > 0$ also quantitatively, the discussion of $\xi_P = 0$ applies when augmented by a stable steady state larger than all others. This can be viewed as the ‘carrying capacity’ state of the reactor. In particular, the scenario of a stable low state now implies presence of a high stable state, which may be called

‘bi-stability’: coexistence of two stable states. Bi-stability is a signature of nonlinear systems and is analogous to a ball rolling in a landscape with two depressions: depending on the initial conditions, the ball can be caught in either and will remain there. In order to use the full potential of the reactor it is desirable to drive it always into the large carrying capacity state, but a discussion of this is beyond the scope of this short article. We only mention that a simple theoretical control would make the tank more shallow so that the maximum of RHS will be below the LHS curve.

We emphasize that local considerations near any fixed value of \mathcal{A} cannot determine whether there exists such a larger stable state: It is an effect of global properties of the model. One indicator of bi-stability that uses medium-range deviation from a known potentially low stable state would be that the return towards this state significantly slows down upon increasing the perturbation in \mathcal{A} . This occurs when approaching the unstable threshold steady state between the low and high states: when the red and green curves get closer, the rate of decay becomes smaller, see Figure 4.5.

The Klausmeier model: nutrient-limited, light surplus

We describe the model from [17, 16] and summarize some relevant results. The model considers the biomass growth depending on the inner nutrient resources of the cells, rather than directly on the nutrient supply in the water. It thus accounts for limited physical space within the cells, which prevents uptake of arbitrary large quantities of raw nutrients, and the time it takes the cells to convert the raw nutrients into the biomass.

The nutrients available from the environment, R_N, R_P , corresponding to N and P , respectively, are thus distinguished from nutrients taken up from the water and stored within the algae cells, i.e., ‘quota’ nutrient: Q_N, Q_P . This approach also allows us to calculate the ratios of raw nutrients left in the water to the cell quota Q_i/R_i ($i = P, N$).

Biologically meaningful initial conditions in this setting require $Q_i > Q_{\min,i}$, i.e., the cell growth starts only after a certain threshold value of stored nutrient has been surpassed. Furthermore, at the initial time $t=0$ a certain amount of the biomass and nutrients are present in the water $\mathcal{A}(0) > 0, R_i(0) > 0$.

Klausmeier et al [17, 16] derived a 5-dimensional model, which describes the dynamics of the concentrations of two co-limiting nutrients and one algae species in an ideal chemostat (the nutrient supply rate a matches the algae dilution rate h_r).

$$\begin{aligned}\frac{dR_i}{dt} &= a(R_{\text{in},i} - R_i) - \frac{v_{\max,i}R_i}{R_i + K_i}\mathcal{A}, \\ \frac{dQ_i}{dt} &= \frac{v_{\max,i}R_i}{R_i + K_i} - \mu_{\max} \min_{j=1,2} \left(1 - \frac{Q_{\min,j}}{Q_j}\right) Q_i, \\ \frac{d}{dt}\mathcal{A} &= \mu_{\max} \min_{j=1,2} \left(1 - \frac{Q_{\min,j}}{Q_j}\right) \mathcal{A} - h_r\mathcal{A}.\end{aligned}$$

The conservation law of this models concerns the total nutrients, which is given by $\sum_{j=1,2} R_j + Q_j\mathcal{A}$; note that Q_j is the nutrient concentration within a cell. Indeed,

the rate of change of nutrients is equal to the nutrients added minus the nutrients removed from this system:

$$\frac{d}{dt} \sum_{j=1,2} R_j + Q_j \mathcal{A} = \sum_{j=1,2} a(R_{\text{in},j} - R_j) - h_r Q_j \mathcal{A}.$$

This model can easily be extended to the case of multiple species (e.g. [19]), competing for the shared resources, as well as incorporating the specific maintenance rate D_r . The latter is set to zero here: $D_r = 0$; the loss of algae is only due to washout from the chemostat.

In contrast to the previous scalar model, the dynamics of higher dimensional models are, in general, no longer determined by the location and stability of steady states alone. However, in this particular case it is: There is again the trivial steady state $\mathcal{A} = 0$, but also one nontrivial steady state, and if the latter exists, it is stable and the ‘global attractor’ [18] (all solutions with positive biomass converge to it). The nonzero steady state (if it exists) is thus the steady state carrying capacity.

For low initial amounts of nutrients, biomass evolution undergoes a number of stages. The first one is characterized by an ‘exponential growth’-state, the so-called quasi-equilibrium state (where only biomass is not in equilibrium), during which the cellular quota ratio Q_N/Q_P matches the so-called *optimal* $N:P$ ratio $Q_{\text{min},N}/Q_{\text{min},P} = 27.7$, given in (mol N)/(mol P), which is also a condition for optimal growth [17, 16].

Thus, if the quota ratio Q_N/Q_P changes, it means that the exponential growth phase has been concluded and biomass has essentially reached equilibrium. If biomass production is the focus, one may increase depletion and harvest at this point. If the interest lies in water purification then the second stage is more interesting: the quota ratio Q_N/Q_P swings towards the supply ratio $R_{\text{in},N}/R_{\text{in},P}$ while the biomass is in equilibrium. This is because algae are, just as most living organisms, highly sensitive to their environment and able to adapt. Interestingly, the model also mirrors this feature and exhibits the flexibility of the cell quota being able to match the supply ratio at the optimal dilution rate of $h_r = 0.59 \text{ day}^{-1}$ [16]. These results have also independently been obtained in a series of chemostat experiments in [28, 29]. However, the harvesting of clean water should be done before the third stage starts, which is when the quota ratio falls back to the optimal ratio $Q_{\text{min},N}/Q_{\text{min},P}$ [16], and the biomass is still at equilibrium. Since the nutrient concentrations, the uptake rates and the quota are modelled separately, it is possible to determine the remaining concentrations of the nutrients in the water.

This model provides a fair description of phytoplankton/algae biomass growth and stoichiometry, which is determined not only by the nutrient supply stoichiometry in the chemostat, but also takes into account the physiological response of the algae.

Klausmeier-Huisman model: light and nutrient limited growth

The previous model is mainly focused on the chemical resources, however, we know from the discussion of the scalar models, that light, i.e. energy, may be a limiting factor for algal biomass growth, so that the next logical step is to incorporate the light dependence.

The simplest extension in view of the discussion above would be the inclusion of the growth function in \mathcal{H} , see section 4.2, in the maximum growth rate μ_{\max} , which then becomes

$$\frac{\mu_{\max}}{z_{\max}} \ln \left(\frac{H_P + I_{\text{in}}}{H_P + I_{\text{out}}} \right) / (k\mathcal{A} + K_{\text{bg}}).$$

The extended ‘Klausmeier-Huisman’ model thus reads, $i = 1, 2$,

$$\begin{aligned} \frac{dR_i}{dt} &= a(R_{\text{in},i} - R_i) - \frac{v_{\max,i} R_i}{R_i + K_i} \mathcal{A} \\ \frac{dQ_i}{dt} &= \frac{v_{\max,i} R_i}{R_i + K_i} - \frac{\mu_{\max}}{z_{\max}(k\mathcal{A} + K_{\text{bg}})} \ln \left(\frac{H_P + I_{\text{in}}}{H_P + I_{\text{out}}} \right) \min_{j=1,2} \left(1 - \frac{Q_{\min,j}}{Q_j} \right) Q_i \\ \frac{d}{dt} \mathcal{A} &= \frac{\mu_{\max}}{z_{\max}(k\mathcal{A} + K_{\text{bg}})} \ln \left(\frac{H_P + I_{\text{in}}}{H_P + I_{\text{out}}} \right) \min_{j=1,2} \left(1 - \frac{Q_{\min,j}}{Q_j} \right) \mathcal{A} - h_r \mathcal{A}. \end{aligned}$$

This still has the trivial steady state, and, depending on parameter values, possibly multiple nontrivial steady states. In that case the analysis of [18] fails. The criterion for stability of the trivial state is readily derived and reads

$$\left(1 - \frac{\bar{Q}_{\text{lim}, \min}}{\bar{Q}_{\text{lim}}} \right) \frac{\mu_{\max}}{z_m K_{\text{bg}}} \ln \left(\frac{H_P + I_{\text{in}}}{H_P + I_{\text{out}}} \right) < h_r,$$

where \bar{Q}_{lim} is the equilibrium value of the quota of the limiting nutrient (we omit the formula). For small dilution rate h_r , this is violated, which means the trivial state would be unstable, the expected situation. Note that removing the light dependent part gives the analogous criterion for the above Klausmeier model, where instability of the trivial state implies that a non-trivial equilibrium is the global attractor. It would be interesting to find a natural connection (homotopy) from this to the scalar nutrient-limited Huisman model from section 4.2, and to analyze this model in more detail.

Conclusions

We reviewed selected minimal models and model building blocks for algae growth from the literature with focus on light and nutrient limitation effects. We showed a simple geometric way to interpret and understand the dynamics of the arising scalar models, in particular their carrying capacity states and the occurrence of bi-stability. Strategies for optimization are beyond the scope of this exposition, and would require better understanding of the actual values of parameters. In a nutshell, we claim that a qualitative analysis provides: consistency check, criteria for growth, estimates of growth rates and carrying capacity, and a framework for optimization. The next step would be to find realistic parameter values and to compare the result with real data.

In the final sections we briefly discussed a more realistic five dimensional model that includes nutrients as dynamic variables and distinguishes intra- and extracellular nutrient concentrations. We proposed an extension by the light-limitation building block of the previous models. Any satisfying mathematical analysis would require much more mathematical formalism and analysis. We refer to [18, 19] for studies in that direction.

4.3 An ODE model for algae growth

Mathematical model

In the previous section a hierarchical series of one-stage models was presented and a steady-state analysis undertaken, which revealed understanding of the long-term behaviour of the pond. In this section a new two-stage model is presented and an attempt is made to obtain ‘real’ values for all the parameters that appear in the models. Due to the more complicated two-stage model a steady-state analysis is not performed, but the Huisman model (see section 2.1) can be obtained from a certain limit; therefore, the steady-state analysis could be used as test cases for the numerical solution presented at the end of this section. The derivation of this limit and numerical confirmation will not be covered in this publication.

Algae growth is a simple two-stage process, illustrated in Figure 4.6: carbon dioxide is pumped into the water and transformed into glucose by photosynthesis; then, nutrients provided by the drain water from the greenhouses and glucose combine to form new algae. Further, the algae, and the sugar stored in them, are assumed to be reduced by starving and harvesting. To keep the model simple, the nutrient composition is neglected, as well as the fact that energy can not only be stored in glucose, but also as more complex sugars and oils.

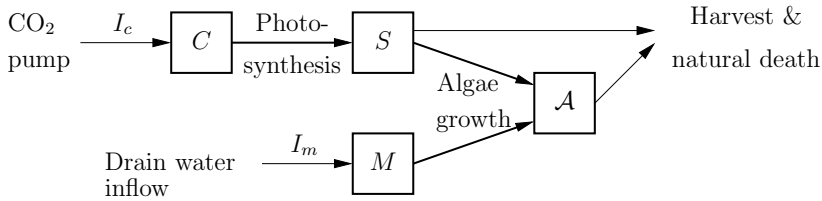
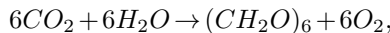


Figure 4.6: Production of algae from nutrients and carbon dioxide.

The algae production is modelled by the concentrations of dry algae \mathcal{A} , nutrients M , sugar S and carbon dioxide C in the pond. Assuming that the pond is well-mixed and algae growth is very slow, the above mentioned concentrations are independent of all spatial variables and only depend on time t ; The inflow of nutrients and carbon dioxide into the pond is denoted by I_m and I_c , respectively. The algae are starving at a ‘death rate’ D_r and harvested at a rate h_r , both of which decrease the amount of algae and the sugar stored inside the algae. Further, sugar is produced at a rate $\alpha_s C$ from carbon dioxide, where α_s is the rate constant. This decreases the amount of carbon dioxide by a rate of $-k_1 \alpha_s C$. From the oxygenic photo-synthetic process,



we know that 44 g of carbon dioxide is needed to produce 30 g of sugar, yielding the conversion rate

$$k_1 = 44/30 \text{ g}[\text{CO}_2] \text{ g}[(\text{CH}_2\text{O})_6]^{-1}.$$

New algae are produced inside the existing algae at a rate $\alpha_A N f_m(M)$ from nutrients and sugar, where α_A is the rate constant and $f_m(M)$ denotes the concen-

tration of nutrients inside the cells. This depletes nutrients and sugar by a rate of $-k_2\alpha_A N f_m(M)$ and $-k_3\alpha_A N f_m(M)$, respectively. Since mass has to be conserved, $k_2 + k_3 = 1$. Based on an estimate in [2] on the composition of algae,

$$k_2 = 0.1 \frac{g[M]}{g[A]}, \text{ and } k_3 = 0.9 \frac{g[(CH_2O)_6]}{g[A]}.$$

Units and a short description of all model parameters can be found in Table 4.1.

Combining the effects of algae growth, photosynthesis, inflow of carbon dioxide and minerals and starving and harvesting of algae, the following system of ODEs is obtained,

$$\dot{A} = \alpha_A f_m(M)S - (D_r + h_0)A, \quad (4.5a)$$

$$\dot{M} = -k_2\alpha_A f_m(M)S + I_m(t), \quad (4.5b)$$

$$\dot{S} = \alpha_s C - k_3\alpha_A f_m(M)S - (D_r + h_0)S, \quad (4.5c)$$

$$\dot{C} = -k_1\alpha_s C + I_c(t). \quad (4.5d)$$

where the rate constants $\alpha_A = \alpha_A(A)$ and $\alpha_s = \alpha_s(A, C, \lambda, \theta)$ are explained in section 4.3.

It should be noted, that in the current model we assumed the total amount of water is constant. We do not explicitly model the inflow/outflow of water or evaporation from the top of the pond. To fully treat the situation were the primary aim is to clean large volumes of run-off water an extra equation for the evolution of the total water volume is required. In the numerical examples presented below no clean water is removed from the system; therefore, this model is valid but additionally considerations are required to model the full decontamination problem.

Proper flux balance is obtained as the model obeys the following conservation law,

$$\frac{d}{dt}(A + S + M + C/k_1) = -(D_r + h_r)(A + S) + I_m + I_c/k_1. \quad (4.6)$$

One sees that the total mass involved is balanced by the nutrient and carbon dioxide input and the material lost by natural death and harvest.

Parameter values and functional dependencies

In the following section, we define the nutrient concentration inside the cell, $f_m(M)$, and the rate constants α_A and α_s . All parameters used below are summarized in Table 4.2.

We assume that the nutrient concentration inside the cell is saturated at $p_{max} = 0.4 \text{ g}[M]m^{-3}$ and that half-saturation is achieved when the outside nutrient concentration is $M_{turn} = 4 \text{ g}[M]m^{-3}$; thus,

$$f_m(M) = p_{max} \frac{M}{M + M_{turn}}. \quad (4.7)$$

The rate constants α_s , α_A depend on various physical parameters. From [2], it is known that α_A saturates with a increasing amount of algae and is half-saturated for

Par.	Unit	Description
\mathcal{A}	$g[\mathcal{A}]m^{-3}$	Concentration of dry algae
M	$g[M]m^{-3}$	Concentration of nutrients
$f_m(M)$	$g[M]m^{-3}$	Concentration of nutrients inside algae cells
S	$g[(CH_2O)_6]m^{-3}$	Concentration of glucose
C	$g[CO_2]m^{-3}$	Concentration of carbon dioxide
I_c	$g[CO_2]m^{-3}day^{-1}$	inflow of carbon dioxide
I_m	$g[M]m^{-3}day^{-1}$	inflow of nutrients
D_r	day^{-1}	(relative) algae death rate
h_0	day^{-1}	(relative) algae harvest rate
$\alpha_{\mathcal{A}}$	$g[\mathcal{A}]g[M]^{-1} \dots$ $g[(CH_2O)_6]^{-1}day^{-1}$	rate constant for biomass growth
α_s	$g[(CH_2O)_6] \dots$ $g[CO_2]^{-1}day^{-1}$	rate constant for photosynthesis
k_1	$44/30 \quad g[CO_2] \dots$ $g[(CH_2O)_6]^{-1}$	conversion rate of CO_2 into $(CH_2O)_6$
k_2	$0.1 \quad g[M] \quad g[\mathcal{A}]^{-1}$	conversion rate of nutrients into dry algae
k_3	$0.9 \quad g[(CH_2O)_6] \dots$ $g[\mathcal{A}]^{-1}$	conversion rate of $(CH_2O)_6$ into dry algae

Table 4.1: Model parameters

$\mathcal{A}_{max} = 30g[\mathcal{A}]m^{-3}$, yielding

$$\alpha_{\mathcal{A}} = \alpha_{\mathcal{A}}(\mathcal{A}) = \hat{\alpha}_{\mathcal{A}} f_{\mathcal{A}}(\mathcal{A}), \text{ where } f_{\mathcal{A}}(\mathcal{A}) = \frac{\mathcal{A}}{1 + \mathcal{A}/\mathcal{A}_{max}}. \quad (4.8)$$

Further, the growth rate of algae is assumed to be proportional to the light intensity and further depends on the temperature and pH of the mixture. Therefore, α_s is proposed to have the following dependencies,

$$\alpha_s = \alpha_s(\mathcal{A}, C, \lambda, \theta) = \hat{\alpha}_s f_{\lambda}(\lambda, \mathcal{A}) f_{\theta}(\theta) f_{pH}(C), \quad (4.9a)$$

where f_{λ} , f_{θ} and f_{pH} model the dependence of the algae growth rate on light intensity, temperature and pH, respectively.

The photo-synthetic process in the algae depends on the light intensity and is therefore depth-dependent. However, since the pool is well mixed, the percentage of light absorbed at any given depth is constant and the light intensity decreases exponentially. In [12], a depth-averaged light intensity is given by

$$f_{\lambda}(\lambda, \mathcal{A}) = \frac{a\mathcal{A}}{a\mathcal{A} + a_{bg}} \ln \left(\frac{H + \lambda}{H + \lambda e^{-(a\mathcal{A} + a_{bg})d}} \right), \quad (4.9b)$$

with λ the light intensity at the pond surface, pond depth $d = 30 \text{ cm}$, half-saturation constant H , light absorption constants of algae $a = 0.00455 \text{ m}^2 g[\mathcal{A}]^{-1}$ and background

$a_{bg} = 7.2 \text{ m}^{-1}$ given in [12].¹

From [30], the photo synthesis rate is optimal at a temperature of $\theta_{opt} = 297 \text{ K}$ and vanishes at temperatures below $\theta_{min} = 269 \text{ K}$. This is modelled by a simple quadratic dependence,

$$f_\theta(\theta) = \max \left(0, 1 - \left(\frac{\theta - \theta_{opt}}{\theta_{min} - \theta_{opt}} \right)^2 \right). \quad (4.9c)$$

We also know from the literature, see section 1.1 for a full discussion, that the photo-synthesis rate has an optimal pH level and does not grow in alkaline solutions. This optimum pH varies massively for different types of algae, here we take an optimal value of 7.4 (which is a little of the low side of the average, see section 1.1) and assume growth vanishes at pH below 6.9. As shown in [22], pH does mainly depend on the amount of potassium and carbon dioxide. A typical potassium content was given in [3] to be $8 \text{ g}[KH]m^{-3}$. Thus, by [22], the minimal and optimal pH corresponds to a carbon dioxide content of $C_{max} = 24.9 \text{ g}[CO_2]m^{-3}$ and $C_{opt} = 7 \text{ g}[CO_2]m^{-3}$, respectively. This behaviour is modelled by a quadratic dependence,

$$f_{pH}(C) = \max \left(0, 1 - \left(\frac{C - C_{opt}}{C_{max} - C_{opt}} \right)^2 \right). \quad (4.9d)$$

It remains to estimate the constants $\bar{\alpha}_s$, $\bar{\alpha}_A$. Therefore we assume that the algae, nutrient, sugar and carbon dioxide concentrations are bounded; therefore, average values \bar{A} , \bar{M} , \bar{S} , \bar{C} exist, with $\bar{\cdot} = \lim_{T \rightarrow \infty} \frac{1}{T} \int_0^T \cdot dt$.

To estimate $\hat{\alpha}_A$, we average equation (4.5b) over time $[0, T]$ and take the limit $T \rightarrow \infty$ to obtain

$$\lim_{T \rightarrow \infty} \frac{M(T) - M(0)}{T} = -k_2 \hat{\alpha}_A \overline{f_A(A) f_m(M) S} + \bar{I}_m, \quad (4.10)$$

Since the nutrient concentration is bounded,

$$\lim_{T \rightarrow \infty} \frac{M(T) - M(0)}{T} = 0;$$

therefore, we approximate $\hat{\alpha}_A$ by

$$\hat{\alpha}_A \approx \frac{\bar{I}_m}{k_2 \overline{f_M(\bar{M}) \bar{S} f_A(\bar{A})}}, \quad (4.11)$$

where we assumed $\overline{f_M(M) S f_A(A)} \approx \overline{f_M(M) \bar{S} f_A(\bar{A})} \approx f_M(\bar{M}) \bar{S} f_A(\bar{A})$, *i.e.*, the average of the total product equals the product of the average of each factor and the typical function value can be estimated by the function value at the typical parameter.

¹We note that the value given in [12] is $a = 0.7 \cdot 10^{-6} \text{ cm}^2 \text{ cell}^{-1}$. From [21], we know that the maximal algae density is $5.6 - 7.5 \cdot 10^6 \text{ cells ml}^{-1}$ and $0.1 \text{ g}[A] \text{ ml}^{-1}$, from which we deduce that algae weigh about $1.5 \cdot 10^{-8} \text{ g cell}^{-1}$.

To estimate $\hat{\alpha}_S$, we average equations (4.5a)+(4.5b)+(4.5c) over time $[0, T]$ and take the limit $T \rightarrow \infty$ to obtain

$$\lim_{T \rightarrow \infty} \frac{(\mathcal{A} + M + S)|_0^T}{T} = \hat{\alpha}_S \overline{f_\lambda(\lambda, \mathcal{A}) f_\theta(\theta) f_{pH}(C) C} + \bar{I}_m - (D_r + h_r)(\bar{\mathcal{A}} + \bar{S}). \quad (4.12)$$

Assuming that the algae, mineral and sugar concentration is bounded, the left hand side of (4.12) vanishes; combining this with the fact that $\bar{C} \approx C_{\text{opt}}$ and $\bar{\theta} \approx \theta_{\text{opt}}$, we estimate $\hat{\alpha}_S$ by

$$\hat{\alpha}_S \approx \frac{(D_r + h_r)(\bar{\mathcal{A}} + \bar{S}) - \bar{I}_m}{f_\lambda(\bar{\lambda}, \bar{\mathcal{A}}) \bar{C}}, \quad (4.13)$$

where we assumed as in (4.11) that

$$\overline{f_\lambda(\lambda, \mathcal{A}) f_\theta(\theta) f_{pH}(C) C} \approx \overline{f_\lambda(\lambda, \mathcal{A})} \overline{f_\theta(\theta)} \overline{f_{pH}(C) C} \approx f_\lambda(\bar{\lambda}, \bar{\mathcal{A}}) f_\theta(\bar{\theta}) f_{pH}(\bar{C}).$$

We estimate $\bar{\mathcal{A}}$, \bar{C} , \bar{M} , \bar{S} , \bar{I}_m , $\bar{\lambda}$, D_r and h_r by typical values from the literature:

- From [2], p. 36, a typical input rate of waste water is 7 to 20 $l\ m^{-3}\ \text{day}^{-1}$. Assuming an average input of drain water of 20 $l\ m^{-3}\ \text{day}^{-1}$, given a nitrogen concentration of 15 $\text{mmol}[N]l^{-1}$ and a molecular weight of $14\text{g}\text{mol}^{-1}$, we estimate $\bar{I}_m = 4.2\ \text{g}[M]m^{-3}\text{day}^{-1}$.
- The input rate yields further that 2% of the water in the pool is changed per day, thus an order of magnitude estimate is given by $\bar{M} = 2\% * \bar{I}_m$.
- The typical sugar content $\bar{S} = 10\ \text{g}[(CH_2O)_6]m^{-3}$ is an estimate from [3].
- Since the carbon dioxide input can be controlled, we assume $\bar{C} = C_{\text{opt}}$.
- A typical algae concentration was provided by [1] to be $\bar{\mathcal{A}} = 6\ \text{g}[\mathcal{A}]m^{-3}$.
- The typical light intensity on the surface is

$$\bar{\lambda} = \lambda_{\text{max}}/2,$$

where the maximum light intensity $\lambda_{\text{max}} = 2000\ \mu\text{mol photons } m^{-2}$ is given by [23].

- The typical harvest rate is

$$h_r = \overline{h_r \mathcal{A}} / (\bar{\mathcal{A}} + \bar{S}),$$

where a typical harvest of $\overline{h_r \mathcal{A}} = 12\text{g}[\mathcal{A}]m^{-3}\text{day}^{-1}$ was given in [2].

- Finally, we use an estimate of the death rate $D_r = 0.46\ \text{day}^{-1}$ derived from [12].

Substituting these values into (4.13) and (4.11) we obtain

$$\begin{aligned} \hat{\alpha}_A &\approx 102\ \text{g}[\mathcal{A}]g[M]^{-1}g[(CH_2O)_6]^{-1}\text{day}^{-1} \text{ and} \\ \hat{\alpha}_S &\approx 676\ \text{g}[(CH_2O)_6]g[CO_2]^{-1}\text{day}^{-1}. \end{aligned}$$

Param.	Value, Source	Description
p_{max}	$0.4 \text{ g}[M]m^{-3}$	maximal nutrient concentration inside algae
M_{turn}	$4 \text{ g}[M]m^{-3}$	half-saturation constant for nutrient
\mathcal{A}_{max}	$30 \text{ g}[\mathcal{A}]m^{-3}$, [2]	concentration inside algae maximal algae concentration before growth shuts down
H	$30 \text{ } \mu\text{mol photons } m^{-2}$, [12]	half-saturation constant
a	$0.00455 \text{ m}^2\text{g}[\mathcal{A}]^{-1}$, [12, 21]	light absorption constant
a_{bg}	7.2 m^{-1} , [12]	background light absorption constant
d	0.3 m	pond depth
C_{max}	$24.9 \text{ g}[\text{CO}_2]m^{-3}$, [22, 3]	maximal CO_2 concentration for photosynthesis
C_{opt}	$7 \text{ g}[\text{CO}_2]m^{-3}$, [22, 3]	optimal CO_2 concentration for photosynthesis
θ_{min}	269 K , [30]	minimal temperature for algae growth
θ_{opt}	297 K , [30]	optimal temperature for algae growth
D_r	0.46 day^{-1} , [12]	algae death rate
h_r	2 day^{-1} , [2]	typical harvest rate
$\bar{\lambda}$	$1000 \text{ } \mu\text{mol photons } m^{-2}$, [23]	average light intensity
\bar{I}_m	$4.2 \text{ g}[M]m^{-3}\text{day}^{-1}$, [2]	typical nutrient inflow
\bar{M}	$0.084 \text{ g}[M]m^{-3}$, \bar{I}_m	typical nutrient concentration
\bar{C}	$7 \text{ g}[\text{CO}_2]m^{-3}$, C_{opt}	typical carbon dioxide concentration
\bar{S}	$10 \text{ g}[(\text{CH}_2\text{O})_6]m^{-3}$, [3]	typical sugar concentration
$\bar{\mathcal{A}}$	$6 \text{ g}[\mathcal{A}]m^{-3}$, [1]	typical dry algae concentration

Table 4.2: Coefficients and typical values.

Limiting Behaviour and Threshold

The most well-known model for population growth is the logistic growth model. It appears naturally in models with one limiting resource. We describe in which way the system of ordinary differential equations (4.5) is related to a logistic growth model.

It is most natural to assume that the amount of minerals M is the limiting factor. We assume that the influx I_c is such that the CO_2 -concentration is optimal, i.e. $\dot{C} = 0$. Since we only want the amount of minerals M to be a limiting factor, we should make differential equations (4.5a) for \mathcal{A} and (4.5b) for M independent of S . We assume CO_2 is transformed into sugar very fast, i.e. α_s is very large. Now depending on the parameters in the model two things can happen: either α_s saturates at a large value of S , i.e. the photosynthesis will not become infinitely fast, or S itself saturates at a large value, i.e. the sugar reserve cannot become infinite. Both of these processes are not captured in the current model, since in the current model we assume S to be not too large. The second effect for example can be built in by replacing S in (4.5a), (4.5b) and the first S in (4.5c) by

$$f_S(S) := \frac{S}{1 + (1/S_{max})S}.$$

Furthermore, we assume $D_r = h_r = I_m = 0$, i.e. no natural death, harvest or inflow of minerals, and M and \mathcal{A} are not too large. For M and \mathcal{A} not too large $\alpha_{\mathcal{A}}$ behaves at leading order linear in \mathcal{A} : $\alpha_{\mathcal{A}} \sim \hat{\alpha}_{\mathcal{A}}\mathcal{A}$; similarly, f_m is at leading order given by

$$f_m \sim \frac{p_{max}}{M_{turn}} M.$$

Equations (4.5a) and (4.5b) reduce to

$$\dot{\mathcal{A}} = \hat{\alpha}_{\mathcal{A}} \frac{p_{max}}{M_{turn}} \bar{S} \mathcal{A} M, \quad (4.14a)$$

$$\dot{M} = -k_2 \hat{\alpha}_{\mathcal{A}} \frac{p_{max}}{M_{turn}} \bar{S} \mathcal{A} M, \quad (4.14b)$$

for some constant value \bar{S} . From these two equations it follows $\dot{M} = -k_2 \dot{\mathcal{A}}$, thus $M(t) = M(0) + k_2 \mathcal{A}(0) - k_2 \mathcal{A}(t)$. Upon substitution in (4.14a) we obtain the logistic equation

$$\dot{\mathcal{A}} = \hat{\alpha}_{\mathcal{A}} \frac{p_{max}}{M_{turn}} \bar{S} \mathcal{A} (M(0) + k_2 \mathcal{A}(0) - k_2 \mathcal{A}(t)).$$

For certain parameter values a threshold for the growth process can emerge. The threshold manifests itself as an equilibrium in the (\mathcal{A}, M, S, C) phase plane. Depending on the parameter values, this equilibrium can be stable. Acting as an attractor, this would limit the growth of \mathcal{A} to this equilibrium value. Taking the CO_2 -input as the relevant bifurcation parameter, application of linear stability analysis at the equilibrium yields the result that for low I_c values, the equilibrium can indeed be stable.

Numerical Results

To investigate the behaviour of equations (4.5), the model was implemented in MATLAB. We first test the numerical model for the case of nutrient limited growth, as discussed in section 4.3. Thus, death rate, harvest rate and nutrient inflow is set to zero, I_c is chosen such that $\dot{C}=0$ and temperature and CO_2 concentration is chosen to be at its optimal values θ_{opt} , C_{opt} , resp.. As initial values we choose $\mathcal{A}(0) = 3 \text{ g}[\mathcal{A}]m^{-3} \ll \mathcal{A}_{max}$, $M(0) = .4 \text{ g}[M]m^{-3} \ll M_{turn}$, and $S(0) = 10 \text{ g}[S]m^{-3}$. The results of this simulation compares favorably with the analytic solution to the logistic limit equations (4.14), cf. Figure 4.7.

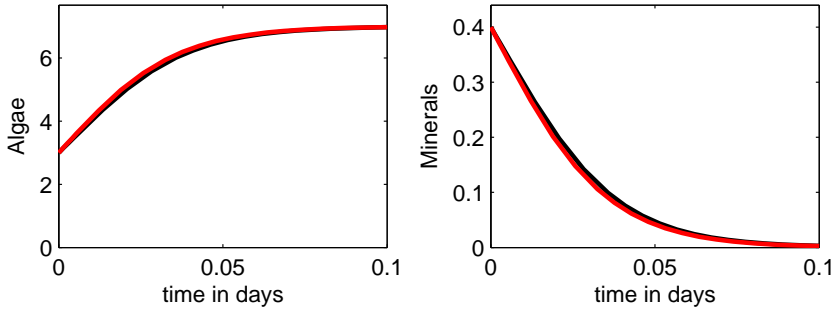


Figure 4.7: Comparison between results from the numerical model (black) and the logistic limit equations (red).

In the following we test the model for different parameter settings.

To optimize the photosynthesis process, the carbon dioxide inflow is controlled such that $C \approx C_{opt}$ by setting

$$I_c(t) = \beta \max(0, g[C]m^{-3}, C_{opt} - C), \quad \beta = 4 \text{ day}^{-1}. \quad (4.15)$$

The ambient temperature was taken to be $\theta(t) = 293K$. To show that algae-growth can be nutrient-limited, we use a low nutrient influx of $I_m(t) = 0.2 \text{ g}[M]m^{-3}\text{day}^{-1}$. The simulation is started with a low algae concentration $\mathcal{A}(0) = 3g[\mathcal{A}]m^{-3}$ and zero sugar, while we chose typical mineral and carbon dioxide concentrations $M(0) = \bar{M}$ and $C(0) = \bar{C}$. We evaluate on the time interval $0 \leq t \leq 20$. We simulate three cases for different harvest and light intensity values, producing the results shown in Figure 4.8.

The red line shows the behaviour, when no harvesting is done and light intensity is constant,

$$h_0(t) = 0 \text{ day}^{-1}, \quad \lambda(t) = \bar{\lambda}. \quad (4.16)$$

The algae grow rapidly until the nutrients are depleted. It then decreases towards a stable equilibrium, while the amount of sugar is increasing. Thus, the algae growth is nutrient-limited.

Next, a day-night cycle is modelled (blue line) by setting

$$h_0(t) = 0 \text{ day}^{-1}, \quad \lambda(t) = \bar{\lambda}(1 + \text{sign}(\sin(2\pi t))). \quad (4.17)$$

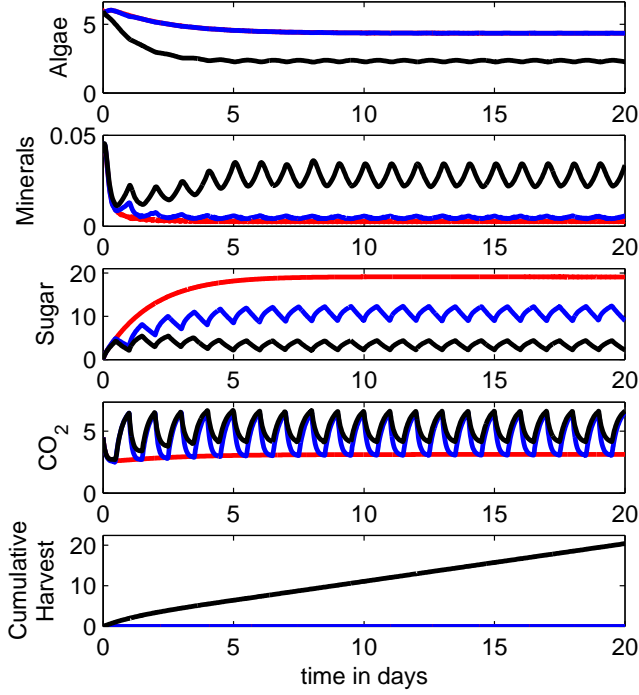


Figure 4.8: Concentrations for $t \in [0, 20]$. Red: $h_r = 0 \text{ day}^{-1}$, $\lambda(t) = \bar{\lambda}$, blue: $h_r = 0$, $\lambda(t) = \lambda_0(1 + \text{sign}(\sin(2\pi t)))$, black: $h_r = 0.4 \text{ day}^{-1}$, $\lambda(t) = \lambda_0(1 + \text{sign}(\sin(2\pi t)))$.

This decreases the amount of sugar, since the photosynthesis rate is non-linear w.r.t. the light intensity. Otherwise, this has only little effect on the algae growth, since it is nutrient- and not sugar-limited.

Finally, harvesting is turned on (black line),

$$h_0(t) = 0.4 \text{ day}^{-1}, \quad \lambda(t) = \bar{\lambda}(1 + \text{sign}(\sin(2\pi t))). \quad (4.18)$$

This significantly decreases the algae concentration. The mineral and sugar concentration now varies around a constant value with the day-night cycle. The mineral concentration initially decays in line with no harvest, but does not fall below a value of 0.2 [grams/ m^3]. This would indicate that growing algae for harvest and removing most of the minerals from the water may be difficult in the same pond; therefore, a two coupled pond configuration, with one used to grow algae and the other to remove nutrients, maybe the only way to achieve the joint goal of nutrient removed and algae cultivation.

Conclusions

In this section a new two-stage model is presented: photo-synthesis converts the CO_2 to sugars and then minerals and sugar are combined to create new algal mass. If you take the limit of a quick photo-synthesis rate and a large bath of nutrients the original Huisman model §4.2 can be obtained. Additional in §3.4 it is shown that this two stage model can additionally be reduced to the logistic equation, when the only limiting factor is the supply of a single nutrient. Separating the minerals and modeling both phosphorus and nitrogen individually results in a system similar to the model studied in §4.2. In this fashion all the extra factors added in §4.2 can be added to this model and vice-versa.

Using parameter values from the literature and temporally averaged estimates, the equations were solved numerically. The effect of harvesting was studied and preliminary study seemed to suggest that two ponds would be best way to satisfy the dual goal of nutrient removal and algae growth.

In various sensible limits, this model can be reduced to the one-stage model presented in §4.2, which can be used to verify the numerical model and give insight into its behaviour in these limiting scenarios.

4.4 An alternative PDE Model

Mathematical Model

All the models considered in the previous sections are temporal models, they investigate the time-evolution of the total mass of algae in a given pond. In this section a spatial-temporal model is presented that takes in account spatial depth variation within the ponds. Additionally, at the end of this section optimization of the model is discussed.

We study the growth of the algae (biomass) in the water body (described by the domain $\Omega \subset \mathbb{R}^3$). The biomass growth rate is related to the process of photosynthesis, the process of mixing and the death rate. The process of photosynthesis depends upon the concentration of the nutrients, the availability of CO_2 and the availability of light. The death rate includes both the harvesting rate as well as the natural death rate of the algae. Since the light intensity is uneven at different depth of the water body, it is important to stir the water to mix the algae. Advection is assumed to be absent which corresponds to the still water body. In the horizontal plane, we consider no variation and hence, the growth rate is independent of x and y coordinates. The depth in the water body is denoted by z .

The growth rate of the algae biomass is given by

$$\partial_t \mathcal{A} = g(I_{\text{in}})f_1(P)f_2(N)f_3(C)\mathcal{A} + D_M \partial_{zz} \mathcal{A} - H_a(\mathcal{A}). \quad (4.19)$$

The mixing is modeled by a diffusion term with a constant coefficient D_M . Inclusion of the mixing term helps to understand the effect of mixing on the overall production rate of the algae. The functions $g(I_{\text{in}})$, $f_1(P)$, $f_2(N)$ and $f_3(C)$ define the dependence of the biomass growth rate on the light intensity, the concentration of nutrients (phosphates and the nitrates), and the carbon dioxide. Function $H_a = (h_r + D_r)\mathcal{A}$ describes the

death rate of the algae biomass including both the harvesting term as well as the natural decay rate. A similar model was used in [13, 25]. For the light intensity, we take the Monod form of dependence [11]

$$g(I_{\text{in}}) = \frac{\mu_0 I_{\text{in}}}{H_L + I_{\text{in}}}, \quad (4.20)$$

where I_{in} is the effective light intensity received by the algae and H_L is the half saturation intensity. The Monod form ensures that the growth rate is almost linear when the light intensity is very small, and the growth rate remains bounded by μ_0 when I_{in} becomes very large. The light intensity received by the algae is not uniform throughout the water body. The light intensity is attenuated by two factors: the presence of algae and the water mass. The presence of the algae in the top layers causes reduction in the available light for the algae in the deeper layers. This describes the non-transparency of the water body due to the presence of algae. Moreover, the water layers themselves cause attenuation in the available light intensity for the deeper layers. In the light of the above discussion, the light intensity can be modeled by

$$I_{\text{in}}(z, t) = I_0(t) e^{-kz} e^{K(z)} \quad (4.21)$$

where

$$K(z) = -r_s \int_0^z \mathcal{A} dz$$

where $I_0(t)$ is the incident light intensity which changes in time (for instance during the day and night cycle). The constant k is the specific light attenuation coefficient due to the water layer and r_s is the specific light attenuation coefficient due to the presence of algae.

For the nutrients, the phosphates and the nitrates, we once again take the Monod type rates

$$f_1(P) = \frac{k_P [P - P_c]_+}{H_P + [P - P_c]_+}, \quad (4.22)$$

$$f_2(N) = \frac{k_N [N - N_c]_+}{H_N + [N - N_c]_+}. \quad (4.23)$$

Again, H_P and H_N are the half saturation concentrations of phosphorus and nitrates respectively. The $[\cdot]_+$ denotes the positive cut-off function $[x]_+ = \max(0, x)$. Parameters P_c and N_c are the critical concentration of the nitrates and phosphates, respectively, below which the growth becomes zero. To model the effect of CO_2 we note that the presence of carbon dioxide affects the pH value of the water. We assume for simplicity that pH value is solely determined by the presence of the CO_2 . The growth rate of the algae is influenced by the pH value apart from the other factors that we discussed above. The consumption of CO_2 leads to the reduction in the CO_2 concentration and hence, leads to the increase in pH value. It is known that there is a certain range of pH value where the algae growth is optimal. Hence, if the source of CO_2 provides more than required, the pH value of the water body will decrease. This decrease can lead to the enhancement of the death rate of the algae. The growth

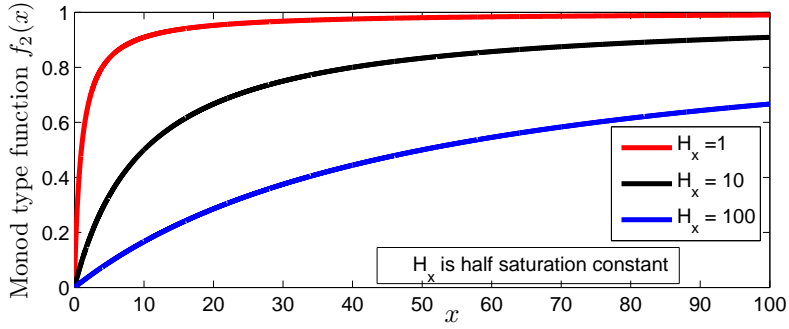


Figure 4.9: Monod type function for different half-saturation constants.

rate dependence is modeled by the functional form that monotonically decreases with pH (and hence monotonically increasing with the concentration of CO_2) however, at higher concentrations of CO_2 the growth rate becomes constant and bounded. We consider the following functional form

$$f_3(C) = \frac{1}{1 + e^{\lambda(pH(C) - pH_{opt})}}, \quad (4.24)$$

where λ is a parameter that describes the sharpness of the profile and pH_{opt} describes the ‘switching’ value of pH at which the growth increases if all other factors are kept unchanged. The relation between the pH and CO_2 is given as

$$pH(C) = (6.35 - \log_{10} C)/2.$$

This relation is obtained using the chemical equilibrium constant of the hydrolysis of the carboxylic acid. The modeling of the harvesting term includes the specific death rate having pH dependence so that at small pH the death rate enhances. We propose the following functional dependence for this term similar to the $f_3(pH)$

$$H_a(w) = D_r f_4(C) \mathcal{A}, \quad (4.25)$$

with

$$f_4(C) = \frac{1}{1 + e^{\lambda(pH(C) - pH_{dopt})}}, \quad (4.26)$$

where pH_{dopt} is again the ‘switching’ value of the pH at which the death rate increases.

In Figure 4.9 and Figure 4.10 we illustrate the nature of Monod- and f_3 functions.

We complete the system with the following ordinary differential equations describ-

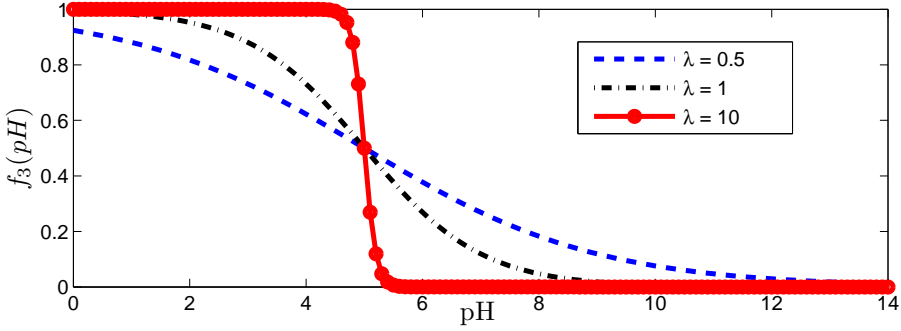


Figure 4.10: $f_3(pH)$ function for different values of parameter λ .

ing the evolution of the nutrients and the CO_2

$$\begin{aligned}
 \frac{dN}{dt} &= -\frac{1}{z_{\max}} \left(\int_0^{z_{\max}} g(I_{\text{in}}) f_1(P) f_2(N) f_3(C) A dz \right) N + S_N, \\
 \frac{dP}{dt} &= -\frac{1}{z_{\max}} \left(\int_0^{z_{\max}} g(I_{\text{in}}) f_1(P) f_2(N) f_3(C) A dz \right) P + S_P, \\
 \frac{dC}{dt} &= -\frac{1}{z_{\max}} \left(\int_0^{z_{\max}} g(I_{\text{in}}) f_1(P) f_2(N) f_3(C) A dz \right) C + S_C,
 \end{aligned} \tag{4.27}$$

where z_{\max} is the maximum depth of the water body.²

We use homogeneous Neumann boundary conditions for (4.19) and we require the following initial conditions

$$N(0) = N_0, \quad P(0) = P_0, \quad C(0) = C_0, \quad w(z, 0) = w_0(z). \tag{4.28}$$

Equations (4.19), (4.27) together with initial conditions (4.28) constitute the system of equations under study. We use the following values of the parameters for the numerical computations taken from [8, 11, 10].

$\mu_0 k_p k_N [1/s]$	$H_L [W/(m^2 \cdot day)]$	$H_N [g/l]$	$H_P [g/l]$
0.0886	70	$14.5 \cdot 10^{-6}$	$10.4 \cdot 10^{-6}$

$r_s [l \cdot m/g]$	$k [1/m]$	$D_M [m^2/s]$	$D_r [g/(l \cdot day)]$
10	0.2	$5 \cdot 10^{-4}$	0

The values of the parameters chosen are realistic, however, not all the parameters are exactly known and approximate values are taken for those parameters. The model is generic and for a given type of algae these parameters need to be determined experimentally. Here, we need the parameters to see whether the obtained results are realistic.

²It should be noted that it is unclear if nutrient and algae mass are conserved in this model.

Numerical experiment

In this section we test our model for the set of parameters presented in the previous section. We solve the system (4.19),(4.27)-(4.28) using the method of lines (MOL) approach which consists of two stages. The first stage is the spatial discretization in which the spatial derivatives of the PDE are discretized, for example with finite differences, finite volumes or finite element schemes. By discretizing the spatial operators, the PDE with its boundary conditions is converted into a system of ODEs in \mathbb{R}^m

$$\mathbf{W}'(t) = \mathbf{F}(t, \mathbf{W}(t)), \quad \mathbf{W}(0) = \mathbf{W}_0, \quad (4.29)$$

called the semi-discrete system. This ODE system is still continuous in time and needs to be integrated. So, the second stage in the numerical solution is the numerical time integration of system (4.29).

We discretize the diffusion operator in (4.19) by standard second-order central differences on a fixed uniform grid $0 = z_1 < z_2 < \dots < z_m = z_{max}$. The integral term within the light function (4.21) is approximated by

$$\int_0^{z_k} \mathcal{A} dz_k \approx \frac{z_k}{k} \sum_{i=1}^k z_i.$$

The other integral term used in (4.27) is approximated by

$$\int_0^{z_{max}} g(I_{in}) f_1(P) f_2(N) f_3(C) \mathcal{A} dz \approx \frac{z_{max}}{m} f_1(P) f_2(N) f_3(C) \sum_{i=1}^m g(I_{in}(z_i, t)) z_i.$$

The obtained system (4.29) is stiff due to the diffusion term, therefore, an implicit numerical integration method must be used. We use the two-stage second-order Rosenbrock ROS2 method [14]. The method is linearly implicit: to compute the internal stages a system of linear algebraic equations is to be solved.

An illustration of the algae concentration in time is given in Figure 4.11. The behaviour in time of P , N , C and pH is presented in Figure 4.12 and Figure 4.13.

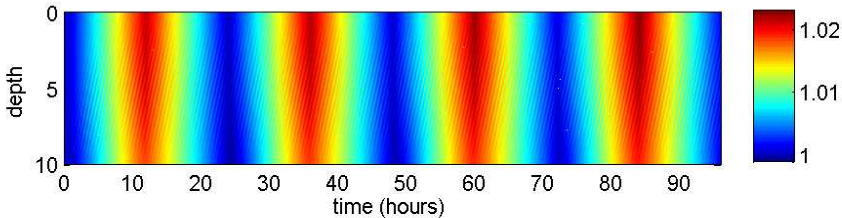


Figure 4.11: Concentration of algae.

The model equations (4.19),(4.27)-(4.28) are discretized and solved in the domain $z \in [0, z_{max}]$ on the interval $t \in [0, T]$, where $T = 96$ [hours], which corresponds to 4

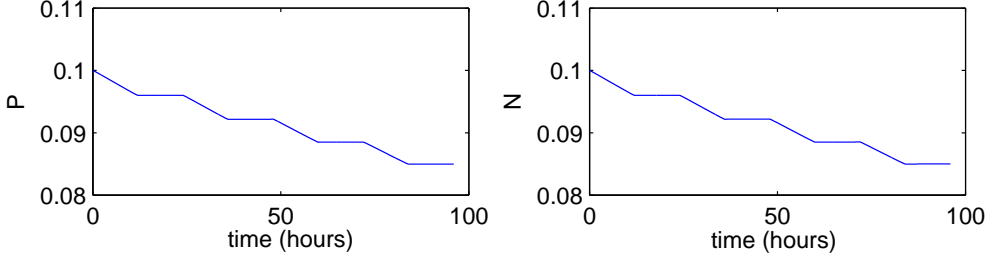


Figure 4.12: Concentration of P and N.

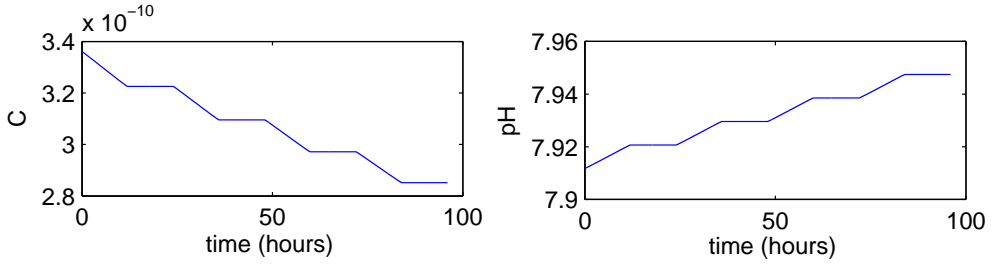


Figure 4.13: Concentration of C and pH.

days. Minerals are being added with a constant rate of $3.64 \cdot 10^{-10} [\text{mol}/(\text{l} \cdot \text{s})]$ and $2.78 \cdot 10^{-10} [\text{mol}/(\text{l} \cdot \text{s})]$ for N and P respectively. No carbon dioxide is added. In Figure 4.11 we notice the periodic nature of the algae concentration. This is due to the day-night cycle of the external illumination modeled by $I_0(t)$. The decay of light intensity with depth makes the solution z -dependent. As expected, the algae concentration is lower at the bottom. However, the mixing included in the model diminishes this difference. Due to a large initial concentration of algae, the rate of consumption of minerals is larger than their inflow rate. There is no inflow of carbon dioxide. Thus, the concentration of minerals and of carbon dioxide in the water decreases monotonically as seen from Figure 4.12 and Figure 4.13. During one day, the maximum algae concentration is attained in the noon when the light intensity on the surface is the largest. In this particular simulation the value of the maximal concentration increases from day to day at a rate which is comparable with literature data.

Optimization

We define the average concentration of algae

$$V = \frac{1}{z_{max}T} \int_0^{z_{max}} \int_0^T \mathcal{A}(z,t) dt dz,$$

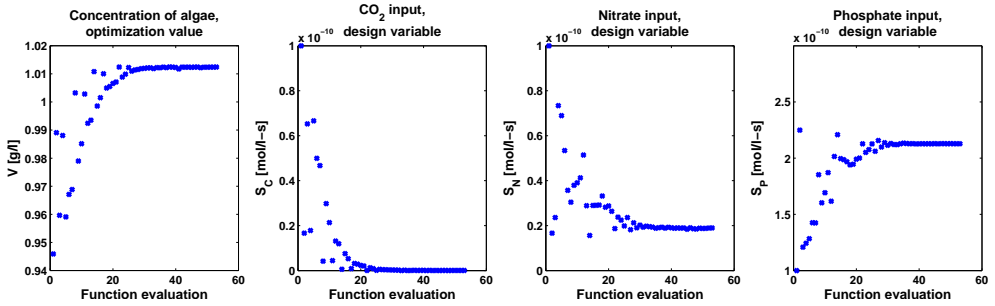


Figure 4.14: Nelder-Mead simplex optimization.

Table 4.3: Optimization parameters.

	S_C [mol/(l-s)]	S_N [mol/(l-s)]	S_P [mol/(l-s)]	V [g/l]
Initial	10^{-10}	10^{-10}	10^{-10}	0.946
Optimized	5.309×10^{-14}	1.886×10^{-11}	2.129×10^{-10}	1.0125

or in discrete form

$$V \approx \frac{1}{nm} \sum_{j=1}^n \sum_{i=1}^m \mathcal{A}(z_i, t_j),$$

where t_i are the time points in which the numerical solution is computed. The average concentration computed by means of the model described above can be optimized as a function of three design variables: carbon dioxide, nitrate and phosphate inflow rates, i.e.

$$\begin{aligned} &\text{maximize } V(S_C, S_N, S_P), \\ &\text{subject to } S_C \geq 0, S_N \geq 0, S_P \geq 0. \end{aligned}$$

For this purpose we apply the Nelder-Mead simplex method [7, 26]. The Nelder-Mead simplex method is designed to find a local optimum of a function. It makes no assumptions about the shape of the function and does not use derivative information. At each iteration the Nelder-Mead simplex method evaluates the function in a finite number of points. In our case one function evaluation corresponds to computing the average concentration of algae.

Figure 4.14 shows an example of the Nelder-Mead optimization. In this case the optimization required 55 function evaluations. The values of the design variables and correspondingly obtained concentration are plotted for each function evaluation. Table 4.3 shows the values of the initial guess and the values after optimization. For the optimized values of the design variables the average algae concentration has increased by 7.03%.

Further, the result of the optimization could be improved by assuming S_C, S_N, S_P to be functions of time. Thus, we assume that $\mathbf{s}_C = \{S_{C,i}\}_{i=1}^L$, where $S_{C,i}$ is the carbon dioxide inflow rate at time t_i . For fixed S_N and S_P we obtain an optimization

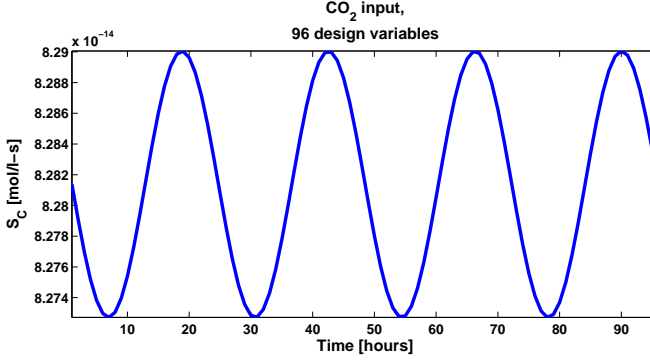


Figure 4.15: Input of CO_2 as a function of time.

problem of L design variables

$$\text{maximize } V(\mathbf{s}_C),$$

$$\text{subject to } S_{C,i} \geq 0.$$

This could result in further improvement of the average algae concentration. As an initial guess for optimization, instead of applying constant carbon dioxide inflow rate, we could use a periodic function with the same period as of the incident light function, with different amplitude and vertical and horizontal shift (see Figure 4.15).

It is important to note that the average algae concentration function may have multiple maxima. However, the Nelder-Mead simplex method is designed to find a local optimum of a function. It means that initial parameter guess should be close enough to the desirable optimum. For a global optimum other optimization methods (for example, simulated annealing optimization [26]) could be used.

Conclusions

We proposed a model for the growth of algae in a mineral solution. The model consists of a partial differential equation for the algae concentration coupled to three ordinary differential equations for the phosphate, the nitrate and the carbon dioxide concentrations. The minerals and the carbon dioxide are assumed to have a constant concentration throughout the volume, while the algae concentration is modeled as a z -dependent quantity. This choice is explained by the strong dependence of light intensity on depth. Moreover, the z -dependency allows us to study the effect of mixing on the algae population. Numerical simulations were performed with the model. To this end, the continuous equations are discretized in space by a finite difference scheme, and the resulting system of ordinary differential equations is integrated in time by a two-stage second-order Rosenbrock method. The simulations have shown a good qualitative prediction for the concentration of algae, minerals and carbon dioxide. In order to achieve also a good quantitative prediction, the parameters of

the model have to be adjusted to the experiment. Based on the proposed model, the average concentration of the algae can be optimized by means of derivative-free optimization.

4.5 Recommendations

In summary, this paper contains the following eight main themes:

1. A review of biological literature, to determine the key factors that effect the growth rate of algae (§4.1).
2. A hierarchical review of existing mathematical models in the literature (§2).
3. Steady-state analysis of one-stage models (§4.2).
4. A new two-stage model (§4.3).
5. Parameter estimation (§4.3).
6. A new spatial-temporal model of algae growth (§4.4).
7. Numerical solutions of the new models (§4.3 and §4.4).
8. A discussion of how to optimize (§4.4).

Each of these themes represents a step forward in understanding the factors that effect algae growth. All the model extensions proposed (theme 2,3 and 6) can be reduced back to the original model of Huisman *et al* [12] in the correct limit. For example the additional spatial terms introduced in theme 6 can be neglected if the re-mixing rate is small. There will be situations where each, or maybe even all, of these additional effects are important and studying these effects both in isolation and combination will be very enlightening. For the simple models (or the limits of the more complicated models) the steady-state analysis (theme 3) is very powerful and highlights when these limits are not valid and additional factors need to be included. Estimating the parameters from either the literature (theme 1,5) or by temporal averaging the equations (theme 5) is a challenge that does need more attention; hopefully, new experimental work specifically aimed at determining the control parameters will take place in the next few years. The numerical investigation (theme 7) of the new models is very limited and there is much more scope for numerical studies that allow the simulation of a full algae pond (or maybe even a coupled series of ponds) in the future. Finally, there is room for more work on optimization of the model (theme 8), but early results and a derivative-free method for optimization have been presented.

We have the following recommendations: Construction of a master model including all the effects discussed in §4.2, §4.3 and §4.4; a detailed analysis on the mathematical limits of this model using the steady-state analysis presented in (§4.2); further controlled experiment to determine the key parameters; an more detailed investigation of optimisation. The steady-state analysis is useful for two reasons: firstly, it reveals the effect individual factors have on the model; secondly, it gives a very useful test case for any numerical solution of the full system. One of the major problems is a

lack of numbers for key parameters in the model §4.1 and §4.3. Therefore a new series of experiments designed to better determine these unknowns would be highly beneficial. Finally, once a good set of parameters is determined, optimization of the model can be undertaken (§4.4) and a detailed investigation (hopefully in collaboration with the industry) of the optimal pond(s) design can be performed.

4.6 References

- [1] *Private communication with D van der Saar, representative of Phytocare.*
- [2] Stichting H2Organic en imares. algencultuur op drainwater uit de bouw. September 2009. *Stichting Innovatie Glastuinbouw Nederland.*
- [3] Andersen R. A., editor. *Algal Culturing Techniques.* 2005.
- [4] E.L. Brand. The salinity tolerance of forty-six marine phytoplankton isolates. *Estuarine Coastal and Shelf Science*, 18:543–556, 1984.
- [5] S. Chen, X. Chen, Y. Peng, and K. Peng. A mathematical model of the effect of nitrogen and phosphorus on the growth of blue-green algae population. *Applied Mathematical Modelling*, 33:1097–1106, 2009.
- [6] L.H. Cheng, L. Zhang, and C. J. Chen, H. L.and Gao. Carbon dioxide removal from air by microalgae cultured in a membrane-photobioreactor. *Sep Purif Technol*, 50:324–329, 2006.
- [7] A.R. Conn, K. Scheinberg, and L.N. Vicente. Introduction to derivative-free optimization. *MPS-SIAM series on optimization*, 2009.
- [8] J. Ramus C.S. Duke, W. Litaker. Effect of temperature on nitrogen-limited growth rate and chemical composition of *Ulva curvata*. *Marine Biology*, 100:143–150, 1989.
- [9] R.J. Geider, H. L. MacIntyre, and T. M. Kana. Dynamic model of phytoplankton growth and acclimation: responses of the balanced growth rate and the chlorophyll a:carbon ratio to light, nutrient-limitation and temperature. *Marine Ecology Progress Series*, 148:187–200, 1997.
- [10] H. Haario, L. Kalachev, and Laine M. Reduced models of algae growth. *Bulletin of Mathematical Biology*, 71:1626–1648, 2009.
- [11] J. Huisman, R.R. Jonker, C. Zonneveld, and F.J. Weissing. Competition for light between phytoplankton species, experimental tests of mechanistic theory. *Ecology*, 80:211–222, 1999.
- [12] J. Huisman, H.C.P. Matthijs, P.M. Visser, H. Balke, C.A.M. Signon, J. Passarge, and L.R. Mur. Principles of the light-limited chemostat: theory and ecological applications. *Antonie van Leeuwenhoek*, 81(1-4):117–133, 2002.

- [13] J. Huisman, N.N. Pham Thi, D.M. Karl, and B. Sommeijer. Reduced mixing generates oscillations and chaos in the oceanic deep chlorophyll maximum. *Nature*, 439:322–325, 2006.
- [14] W. Hundsdorfer and J.G. Verwer. Numerical solution of time-dependent advection-diffusion-reaction equations. *Springer Series in Comp. Math.*, 33, 2003.
- [15] E. Kebede-Westhead, C. Pizarro, and W. W. Mulbry. Treatment of swine manure effluent using freshwater algae: Production, nutrient recovery, and elemental composition of algal biomass at four effluent loading rates. *Journal of Applied Phycology*, 18:41–46, 2006.
- [16] C.A. Klausmeier, E. Litchman, T. Daufresne, and S.A. Levin. Phytoplankton stoichiometry. *Ecol. Res.*, 23:479–485, 2008.
- [17] C.A. Klausmeier, E. Litchman, and S.A. Levin. Phytoplankton growth and stoichiometry under multiple nutrient limitation. *Limnol Oceanogr.*, (4):1463–1470, 2004.
- [18] de Leenheer, P., S.A. Levin, E.D. Sontag, and C.A. Klausmeier. Global stability in a chemostat with multiple nutrients. *J. Math. Biol.*, 52:419–438, 2006.
- [19] B. Li and H.L. Smith. Global dynamics of microbial competition for two resources with internal storage. *J. Math. Biol.*, 55:481–515, 2007.
- [20] J.C. Merchuk. Photobioreactor design and fluid dynamics. *Chem. Biochem. Eng. Q.*, 21(4):345–355, 2007.
- [21] Víctor J. Nuñez, Domenico Voltolina, Mario Nieves, Pablo Piña, Alejandra Medina, and Martín Guerrero. Nitrogen budget in *scenedesmus obliquus* cultures with artificial wastewater. *Bioresource Technology*, 78(2):161 – 164, 2001.
- [22] Erik Olson. The krib: Aquaria and tropical fish. <http://www.thekrib.com/Plants/C02/kh-ph-co2-chart.html>.
- [23] Erik Olson. The krib: Aquaria and tropical fish. <http://www.thekrib.com/Plants/Tech/intensorama.html>.
- [24] E. Paasche. Biology and physiology of coccolithophorids. *Annual Review of Microbiology*, 22:71–86, 1968.
- [25] N.N. Pham Thi. Numerical analysis of phytoplankton dynamics. PhD thesis, University of Amsterdam, 2006.
- [26] H. Press, W. S.A. Teukolsky, and W.T. Vetterling. Numerical recipes: the art of scientific computing. 2007.
- [27] O. Pulz. Photobioreactors: production systems for phototrophic microorganisms. *Appl Microbiol Biotechnol*, 57:287–293, 2001.

- [28] G.Y. Rhee. Effects of $n:p$ atomic ratios and nitrate limitation on algal growth, cell composition, and nitrate uptake. *Limnol. Oceanogr.*, 23:10–25, 1978.
- [29] G.Y. Rhee. Continuous culture in phytoplankton ecology. *Adv. in Aquatic Microbiology*, pages 151–203, 1980.
- [30] Denis van Rensburg. The chemistry in shadehouses. http://www.ont.co.za/new_page_1.htm.
- [31] A. Vonshak. *Spirulina platensis* (arthrospira): Physiology, cell biology and biotechnology. *Journal of Applied Phycology*, 9(3), 1997.

Report 5

Modeling Compressible Non-Newtonian Chicken Flow

Oleg Matveichuk¹, Patricio Rosen Esquivel¹, Hanif Heidari^{2,3}, Adrian Muntean¹

Abstract

This paper addresses a few modeling issues relevant for the basic theoretical understanding of the meat flow behavior in simple geometries. We model the meat mixture as a non-Newtonian compressible fluid. Focusing on conceptually easy-to-follow cases like flow in thin molds, or steady incompressible or compressible flow in straight pipes we derive explicit expressions for the velocity and pressure profiles. For the thin mold case, we formulate a one-dimensional free-boundary problem able to capture the *a priori unknown* position of the moving meat-air interface. Special attention is paid on the derivation of the free boundary conditions.

5.1 Introduction

Understanding how meat flows is one of the fundamental aspects when designing a stable shape and content quality for food products, such as nuggets, croquettes, or meatballs. The overall process has a twofold complexity:

- (1) Meat is a compressible non-Newtonian fluid with variable viscous properties and micro-structure (e.g. fiber orientation) strongly dependent on temperature variations. Such a flow behavior typically causes complex (meat) deformations especially in non-continuous flows, where the values of meat parameters and even the equipment itself never stabilizes. This is a highly complex scenario and complexity hampers the accurate prediction of both flow and final product quality (and, consequently, also the optimization of the processing equipment).
- (2) The geometry (patterned manifolds, irregular molds) is often complex and is continuously changing from a product to another.

The problem posed by Marel to the *72 European Study Group Mathematics with Industry* was the following: Predict in a better way how meat properties affect flow in forming (molding) machines, where the meat mass is pressed in molds during mold opening and flow is a start-stop phenomena. More precisely, develop a mathematical model that predicts non-continuous flow of viscoelastic, compressible meat mass in simple geometries, where the pressure fluctuation, deformation rates, mold filling rates, and final product weight are key parameters.

¹Technical University of Eindhoven

²University of Twente, Enschede

³Tarbias Modares University, Tehran, Iran

We have chosen to discuss the case of a simple geometry⁴ – cylindrical pipes – and we have focused on developing a complete mathematical model for isothermal viscous compressible flow of meat (e.g. chicken). We included the micro-structural meat properties in a nonlinear power-law relationship connecting the shear rate to the shear stress. Besides the law governing the conservation of meat mass, we derived, by means of *first principles* arguments, a constitutive law for the meat density as a function of internal pressure.

In the steady case and also when neglecting the nonlinear inertia terms, we succeeded to find an approximate solution for the velocity profile for meat flow in cylindrical pipes and meat flow between two plates.

Furthermore, we can give theoretical estimates of the time to fill a mold in two conceptually-distinct ways:

- (a) As mentioned in Remark 5.3.1, we know how to formulate a time-optimal-control problem for the meat density, the time to fill a mold, and a corrector factor (using an approximate velocity profile). Interestingly, the resulting problem resembles the porous media equation.
- (b) We can suggest a calculation strategy, which gives exact results in one-space dimension, for the time to fill a mold, namely a free-boundary problem having as unknowns the velocity profile and the position of the interface between meat and air.

In our opinion, both working strategies deserve further attention from a combined modeling, analysis, and simulation perspective. Here we focus only on strategy (b).

The paper is organized as follows: In section 5.2, we develop a general model involving partial differential equations (PDEs) to describe the meat (chicken) flow. This is the core of our paper. The aim of section 5.3 is mainly to derive an easy-to-handle approximate solution for velocity profiles, for getting some insight about the characteristics of the problem, while in section 5.3 we propose a free-boundary problem to better understand meat flow behavior in linear molds.

5.2 Modeling chicken flow

In the current section we describe a complete set of equations which are able to capture the macroscopic behavior of chicken flow in a given geometry, say $\Omega \subset \mathbb{R}^3$. Note that the meat is a mixture of material fractions with different properties, such as a fibers, animals fats, bubbles of air trapped during the process of homogenization of the mixture, and so on. The presence of all these components, some of which having complex rheological properties, define the overall flow properties of the material. Assuming that the material is homogenized to an extent such that inhomogeneities of the meat are not noticeable at the macro-scale, allows us to make use exclusively of "effective" or averaged variables, coefficients and model equations. Let's denote by

⁴Note that the structure of the balance equations does not depend on the precise choice of the geometry.

T the final time of the process. Then $t \in (0, T)$ is the time variable, while $x \in \Omega$ is the spatial variable.

The conservation of mass is stated by continuity equation

$$\frac{\partial \rho}{\partial t} + (\nabla \cdot \rho \mathbf{v}) = 0 \text{ in } \Omega \times (0, T). \quad (5.1)$$

Here ρ is the density of the meat-mixture, while \mathbf{v} represents the meat flow velocity.

The balance of the (linear-) momentum density is described by a Navier-Stokes-like equation. The major difference here compared to the Navier-Stokes equations for usual Newtonian liquid lies in the very special expression of the stress tensor. This balance of linear momentum reads:

$$\frac{\partial}{\partial t}(\rho \mathbf{v}) + (\mathbf{v} \cdot \nabla)(\rho \mathbf{v}) = -\nabla p + \nabla \cdot \boldsymbol{\sigma} \text{ in } \Omega \times (0, T). \quad (5.2)$$

Here $\boldsymbol{\sigma}$ is the stress tensor and p is the static pressure in the material.

Due to the specifics of our problem, all investigations reported in this note are focused on shear flows. Therefore it is enough to determine averaged shear properties of the meat-mass to account for the contributions to the stress tensor. Previous works (cf. e.g. [6, 8, 3, 4], or [7] (chapter 5)) indicate that the flow properties of the meat-masses can be taken in the form:

$$\eta_{shear} = k |\dot{\gamma}|^{n-1} \text{ in } \Omega \times (0, T), \quad (5.3)$$

where $k > 0$ and $n \in [0.2, 0.4]$ are empirical⁵ coefficients.

To complete our model we still need an equation of state. To be more precise, we have to specify the compressibility properties of the material as a function of its actual density and temperature. The change of temperature has a twofold effect - it changes coefficients k , n and directly affects the flow compressibility. It is worth noting that the empirical equation (5.3) defining the shear viscosity of the meat flow is approximate, and moreover, this approximation strongly depends on temperature variations. This means that we expect that small changes in temperature are able to produce rather large deviations from the real shear viscosity. The parameters k and n play the role of correctors compensating some of the errors induced by the variations in temperature. In what we are concerned, we consider only an isothermal situation, hence, k and n are fixed for when fixing the temperature level. What about the influence of the temperature changes on the compressibility? The main part of the compressibility of the meat-mass is due to the most *compressible* material fraction, i.e. due to air bubbles. The effect is rather obvious: The bigger the bubble fraction is, the bigger the compressibility. Roughly speaking, in order to notice the compressibility of the air the changes of temperature should be in the range of $300K$. However, this temperature range is not the one encountered when filling molds with flow meat. This fact suggests that as equation of state we may consider a *density-pressure relationship*.

The fact that the our material system consists of both compressible and incompressible parts (air-filled parts *versus* liquid and solid parts of meat) leads us to the

⁵In most of the cases, n and k are fitting parameters. We expect them to incorporate important micro-structure information like the local orientation of the meat fibers.

following *first principles* approach:

$$pV = \tilde{b}_1 p + \tilde{b}_2 \text{ in } \Omega \times (0, T), \quad (5.4)$$

or equivalently,

$$\rho = \frac{p}{b_1 p + b_2} \text{ in } \Omega \times (0, T). \quad (5.5)$$

Here b_1, b_2 , or equivalently, \tilde{b}_1, \tilde{b}_2 are material coefficients depending on the concentration of air.

The equation of state (5.4) together with boundary conditions (describing the experimental setup – the concrete food-processing machine) and initial condition (the precise type of meat) complete the set of our model equations. It is worth noting that, trusting arguments like those employed, for instance, in [1] (chapter 3) and [2] (chapter 3), we expect that our model is *thermodynamically consistent* in the sense that it fulfills the Clausius-Duhem inequality.

In the remainder of the paper, we study various flow behaviors corresponding to specific (simple) geometries when boundary conditions delimitate different experimental situations. Our focus will then be oriented towards the motion of the *a priori unknown* free interface separating meat and bulk air.

5.3 Construction of approximate velocity profiles

In this section we derive an approximate velocity profiles for the chicken flow in cylindrical pipes. We start by considering the case of steady incompressible meat flow. Under these assumptions, the term $\frac{\partial}{\partial t}(\rho \mathbf{v})$ drops out, and hence (5.2) takes the form

$$\rho(\mathbf{v} \cdot \nabla \mathbf{v}) = -\nabla p + \nabla \cdot \boldsymbol{\sigma} \text{ in } \Omega. \quad (5.6)$$

Due to the prominent viscous properties of the meat mixture and due to the particular scale of speed used in the processing machines, inertial effects become less important than viscous effects. Therefore, neglecting the inertia term in (5.2) yields

$$-\nabla p + \nabla \cdot \boldsymbol{\sigma} = 0 \text{ in } \Omega. \quad (5.7)$$

Note that (5.7) is some sort of Stokes-like approximation, in which the stress tensor $\boldsymbol{\sigma}$ appears in general form.

In what follows we consider particular geometries mimicking standard ones used in food processing technologies in order to derive closed-form expressions for meat velocity and density profiles.

Steady flow in straight pipe

Let us consider firstly a straight cylindrical pipe. In this particular case, by neglecting the effects of gravity, we can assume axial symmetry of the flow with respect to the center line of the pipe. Consequently (5.7) can be rewritten in cylindrical coordinates as follows

$$-\frac{\partial p}{\partial z} + \frac{\partial}{\partial r} \left(k |\dot{\gamma}(r)|^{n-1} \dot{\gamma}(r) \right) + \frac{1}{r} k |\dot{\gamma}|^{n-1} \dot{\gamma}(r) = 0, \text{ in } \Omega, \quad (5.8)$$

where z is the coordinate in the axial direction, and r is the coordinate in the radial direction. Applying the chain rule of differentiation and multiplying the result by r gives

$$-r \frac{\partial p}{\partial z} + \frac{\partial}{\partial r} \left(rk |\dot{\gamma}(r)|^{n-1} \dot{\gamma}(r) \right) = 0 \text{ in } \Omega. \quad (5.9)$$

After integrating with respect to r and substituting $\dot{\gamma}(r) = -\partial v / \partial r$, where v denotes the axial velocity component, the latter equation takes the form

$$-\frac{r}{2k} \frac{\partial p}{\partial z} + \left| \frac{\partial v}{\partial r} \right|^{n-1} \frac{\partial v}{\partial r} = 0 \text{ in } \Omega. \quad (5.10)$$

Solving for $\partial v / \partial r$, integrating with respect to r , and finally, using the no-slip condition at the wall of the pipe, we obtain

$$v(r) = \frac{n}{n+1} \left(-\frac{1}{2k} \frac{\partial p}{\partial z} \right)^{1/n} \left(R^{\frac{n+1}{n}} - r^{\frac{n+1}{n}} \right) \text{ for all } r \in \Omega, \quad (5.11)$$

where the new constant R stands for the radius of the pipe. Fig. 5.3 shows a comparison between the well known parabolic Poiseuille profile for Newtonian fluids and a typical profile for steady non-Newtonian flow (5.11). Depending on the particular value of the parameter n , the profile becomes flatter or steeper. For the case of chicken flow with $n \in [0.2, 0.4]$ the viscosity decreases when the shear rate increases. Consequently, the profile becomes flatter.

Compressible steady flow in a pipe

The velocity profile (5.11) was obtained by neglecting the effects of compressibility. However, when speaking about meat flow, one actually wants to keep some compressibility effects in the game. In this section, we look at a steady flow of the meat-mixture and including the compressibility accordingly to the equation of state (5.4).

In order to simplify matter, we consider our equation already averaged over the cross section of the pipe. Let $\hat{\Omega} := (0, L)$ be the new domain, where L is the length of the pipe. For notational convenience, we use in the derivations below v for denoting the average velocity over the pipe cross section. Note that the velocity v can be decomposed as

$$v(z) = v_0 + u(z), \quad (5.12)$$

where v_0 is the average of the velocity profile (5.11) derived in the previous subsection. Furthermore, by neglecting inertia effects and linearizing our equations, we obtain the following system of equations posed in $\hat{\Omega}$:

$$\frac{\partial p}{\partial z} + \frac{\partial p}{\partial \rho} \frac{\partial \rho}{\partial z} = 0, \quad (5.13a)$$

$$\rho \frac{\partial u}{\partial z} + v_0 \frac{\partial \rho}{\partial z} = 0. \quad (5.13b)$$

Dividing (5.13b) by ρ and integrating with respect to z we obtain

$$u(z) = -v_0 \ln \left(\frac{\rho}{\rho_0} \right). \quad (5.14)$$

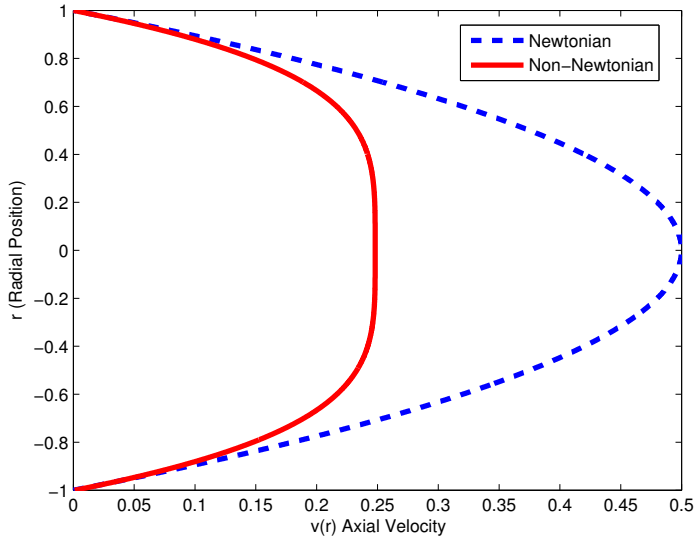


Figure 5.1: Velocity profiles in a straight pipe, for Newtonian and non-Newtonian fluid.

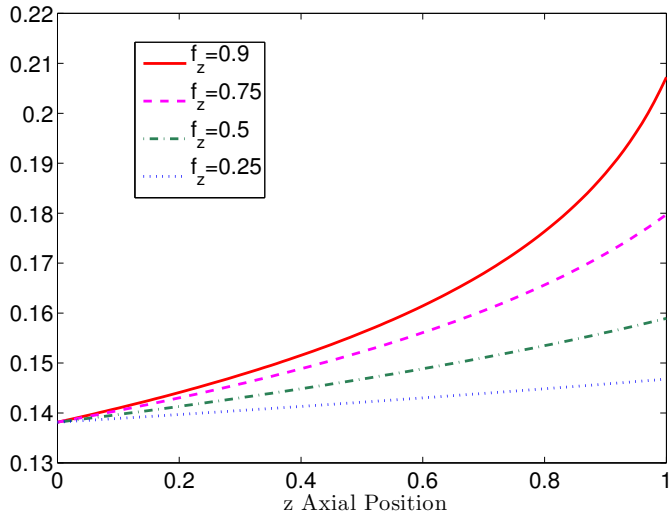


Figure 5.2: Velocity deviation u as function of the axial position.

From (5.13a) we obtain then the density $\rho(z)$. Indeed, substituting (5.4) in (5.13a) yields

$$\frac{\partial}{\partial \rho} [(b_1 p + b_2) \rho] = \frac{\partial p}{\partial s}, \quad (5.15)$$

from which we finally obtain

$$\rho(z) = \frac{1 - \frac{\partial p}{\partial z} z}{b_1 \left(1 - \frac{\partial p}{\partial z}\right) z + b_2} \text{ for all } z \in \hat{\Omega}. \quad (5.16)$$

One important conclusion can be observed from this derivation. That is, that even in the case of steady flow, the average velocity along the pipe is not uniform. In fact, due to compressibility, the velocity of the flow increases with the axial direction. This can be clearly observed in Fig. 5.2 for different values of the pressure gradient, the density is plotted in Fig. 5.3. The decompression taking place in the axial direction, introduces an extra velocity component to the flow, making the velocity distribution non-uniform.

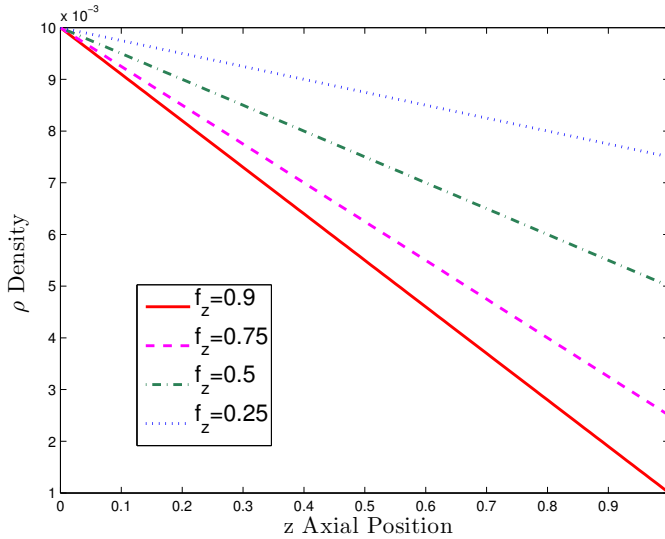


Figure 5.3: Density ρ as function of the axial position $z \in \hat{\Omega} := (0, L)$ with $L = 1$.

Remark 5.3.1. Interestingly, the pipe chicken flow situations described is remotely resembling the porous media equation. One can see this easily when inserting the explicit expressions of $v = v(\rho, \rho_0, v_0)$ into meat mass balance. This similarity can potentially be used (see e.g. [5]) to formulate a time optimal control problem for chicken flow.

On moving free chicken-air interfaces in linear molds

The aim of this part is to describe the filling of the mold by meat masses. We assume that the mold has the form of the parallelepiped with a much less height compared to its width and thickness. We choose the Cartesian coordinate system so that Oz is directed vertically, Ox is directed from left to the right and Oy forms the right triple with the other two axes.

Near the walls the speed of the meat is minimal and somewhere inside gains its maximum. The small height of the mold means that the vertical velocity gradients are much bigger than the horizontal ones. Consequently the main input in the friction term seems to be caused by vertical velocity gradients. If the boundary data prescribed at the left and right sides do not vary much along the sides then it also makes sense to formulate the filling-mold-problem as a one-dimensional event. Let's denote by $s(t)$ the free boundary (meat front) separating the meat bulk $(0, s(t))$ from the air part $(s(t), L)$. The front of the meat starts to propagate from left side to the right. We are now interested in the time-behavior of the front of the meat. The equations in this case can be derived from equation (5.2) by integrating along the Oy and Oz directions. Locally, due to the high viscosity of the meat mixture, the velocity profile along Oz direction can be taken as in-between two parallel plates. But, of course, the average velocity given by this profile can be different for different points x .

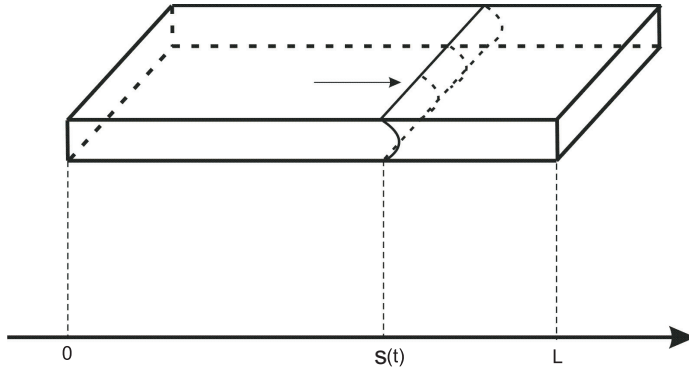


Figure 5.4: The velocity profile for the steady flow between two plates.

The velocity profile between two parallel plates is then

$$v(x) = \frac{n}{n+1} \left| \frac{\nabla p}{k} \right|^{\frac{1}{n}} \left(\left(\frac{d}{2} \right)^{\frac{n+1}{n}} - x^{\frac{n+1}{n}} \right) \text{ for } x \in \left(-\frac{d}{2}, \frac{d}{2} \right). \quad (5.17)$$

Here d is the distance between the plates, ∇p is the pressure gradient, while k and n enter the expression for the viscosity (5.3). From this profile we get a relation between the average velocity and the pressure drop due to viscosity

$$\nabla p_{drop} = \xi |v|^{n-1} v, \quad (5.18)$$

where ξ is a constant coefficient which relates to the coefficient k .

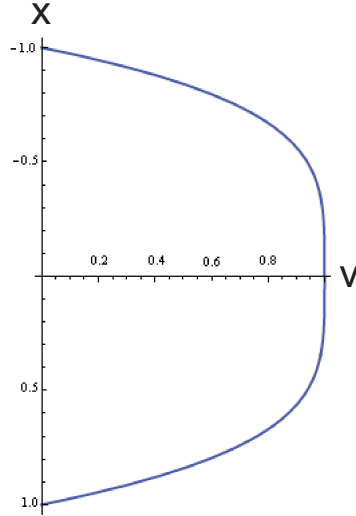


Figure 5.5: The velocity profile for steady meat flow between two plates.

Summarizing, we get the equations for the averaged velocity $v(x)$ and density $\rho(x)$ in the mold. The balance of momentum is

$$\frac{d(\rho v)}{dt} = -\frac{\partial p}{\partial x} - \xi |v|^{n-1} v \text{ in } [0, L] \times (0, T), \quad (5.19)$$

and the conservation of meat mass reads

$$\frac{d\rho}{dt} + \rho(\nabla \cdot v) = Q(x, t) \text{ in } [0, L] \times (0, T). \quad (5.20)$$

Here the total differentials are the Lagrange derivatives, i.e. this is the derivative in accompanying system of reference for a local portion of the fluid. The function $Q(x, t)$ - accounts for a possible sources of meat inside the mold. The additional sources of the meat are the possible inlets for the meat at the sides of the mold.

The boundary conditions are:

$$p(0, t) = p_{in}(t) \quad \text{and} \quad p(s(t), t) = p_b.$$

Here $v_{in}(t)$ is the velocity at the left side of the mold, $p_{in}(t)$ is the pressure on the left side, and $p(s(t), t) = p_b$ - the pressure at the meat front. p_b is the atmospheric pressure. In practice there are many small outlets for the air to go out in the mold. The inertia of the air is negligible compared to the inertia of the meat. That is why we can neglect the changes of the pressure near the right boundary due to the flow of air. $s(t)$ is the function of the coordinate of the meat-air boundary on time and is an unknown of our model. To determine $s(t)$ we have to introduce an additional

interface condition. This condition naturally arises when imposing the momentum balance at that boundary. But, as it was said above, we neglect the inertia of the air. Consequently, the momentum transfer by air is also negligible. So the condition on the free boundary should be "no momentum transfer to the air", i.e.

$$\rho \frac{d^2 s}{dt^2} = -\frac{\partial p}{\partial x} - \xi \left| \frac{ds}{dt} \right|^{n-1} \frac{ds}{dt} \text{ in } [0, L] \times (0, T). \quad (5.21)$$

This equation defines the motion of the free boundary. It is a kind of Rankine-Hugoniot conditions. But to make use of it we need to know the pressure gradient near the boundary. To find it we have to find the function $p(x, t)$. Therefore this equation has to be solved together with (5.19) and (5.20). If we assume for a moment, that the pressure gradient is constant in time, then we can immediately find the meat-boundary motion. The pressure on the moving boundary is constant, and therefore the density near the boundary is also constant. This leads to the following equation for the boundary

$$\rho \frac{dv}{dt} = \xi |u|^{n-1} u - \xi |v|^{n-1} v \text{ in } [0, L] \times (0, T). \quad (5.22)$$

Here u is a constant that can be related to the strength of the flow. The bigger the pressure applied on the left edge, the bigger u is. The plot $v(t) = s'(t)$ is shown in Fig. 5.6.

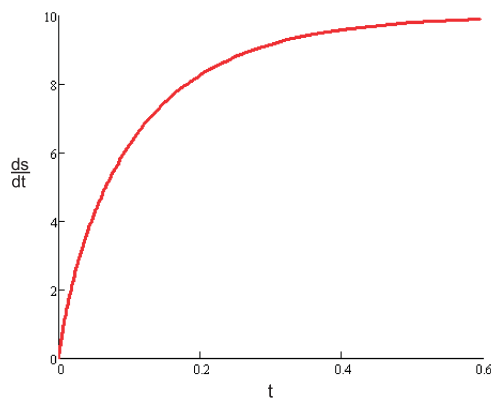


Figure 5.6: The velocity $s'(t)$ of the meat front in the mold as a function of time.

It seems that for short time the velocity of the meat front follows the asymptotic relation $s'(t) = \mathcal{O}\left(t^{\frac{1}{2}}\right)$ for $t > 0$. On the other hand, we expect that the large time behavior of $s'(t)$ will essentially depend on the exponent n . We will focus elsewhere on capturing the precise short- and large-time asymptotics of the meat front.

Acknowledgments

Fruitful discussions with Han Slot (TU Eindhoven) are kindly acknowledged. We also thank Bertus Dunnewind (STORK) for introducing us to this subject.

5.4 References

- [1] L. C. Evans. *Entropy and Partial Differential Equations*. unpublished book, Berkeley University, USA, 2010.
- [2] M. Fabrizio and A. Morro. *Mathematical Problems in Linear Viscoelasticity*. SIAM, Philadelphia, USA, 1992.
- [3] M. Houska, J. Sestak, J. Jeschke, M. Adam, and J. Pridal. Rheology of minced meat transportation in pipes. *Progress and Rends in Rheology*, II:460–463, 1988.
- [4] J. C. M. Jacobs, J. H. Houben, T. van Vliet, P. S. van Roon, and B. Krol. Characterization of the flow behavior of sausage emulsions with a simple tube viscometer. *International Journal of Food Science and Technology*, 29:321–329, 1994.
- [5] Xu Liu. Null controllability of a class of Newtonian filtration equations. *J. Math. Anal. Appl.*, 342:1096–1106, 2008.
- [6] M. A. Rao and R. C. Anantheswareen. Rheology of fluids in food processing. *Food Technology*, 1(1):116–126, 1982.
- [7] J. F. Steffe. *Rheological Methods in Food Processing*. Freeman Press, East Lansing, USA, 2nd edition, 1996.
- [8] R. I. Tanner. *Engineering Rheology*, volume 14 of *Oxford Engineering Science Series*. Clarendon Press, Oxford, 1985.